Generation, Characterization, and Migration Behavior of Vesicle Suspensions

By

Kari Storslett

A dissertation submitted in partial satisfaction of the

requirements for the degree of

Doctor of Philosophy

in

Chemical Engineering

in the

Graduate Division

of the

University of California, Berkeley

Committee in charge:

Professor Susan J. Muller, Chair
Professor Dorian Liepmann
Professor David B. Graves

Summer 2017

Generation, Characterization, and Migration Behavior of Vesicle Suspensions

Abstract

Generation, Characterization, and Migration Behavior of Vesicle Suspensions

by

Kari Storslett

Doctor of Philosophy in Chemical Engineering

University of California, Berkeley

Professor Susan J. Muller, Chair

This dissertation is an attempt to address open questions in the area of suspension migration behaviors that have been observed. Different flow regimes and their corresponding migration behaviors are introduced, and the lack of experiments investigating the collective migration behavior of deformable particle or vesicle suspensions is discussed. One of the reasons for this gap in the literature is the absence of readily available, well-controlled vesicle suspensions (or another model deformable particle suspension). Vesicles are attractive to study because their dynamic behavior in flow is similar to that observed for cells of interest (e.g. red blood cells), but most vesicle generation methods produce very polydisperse vesicle suspensions – or suspensions with a broad distribution of vesicle diameters. The development of a protocol for reduced-polydispersity vesicle suspensions involves a parametric study of electroformation as a vesicle generation method, as well as the application of microfluidic separation technologies, originally developed for suspensions of particles and cells. Because the resulting vesicle suspensions still exhibit some polydispersity, migration experiments are performed with a bidisperse suspension of rigid spherical particles to gain insight into the effect of polydispersity on migration behavior. Initial results indicate that even in dilute conditions, particles in mixed suspensions exert some influence over each other. Differences are observed when comparing migration lengths of particles in bidisperse suspensions to migration lengths of particles in monodisperse suspensions. Potential next steps and challenges to conducting migration experiments with vesicle suspensions are discussed.

Table of Contents

Chapter 1. Suspensions in flow

1.1 Introduction

1.1.1 *Motivation for suspension flow studies*

A suspension is a heterogeneous mixture composed of dispersed particles in a continuous medium. When this mixture is subjected to flow, the dispersed particles can exhibit interesting behavior depending on the suspension parameters (e.g. particle composition, concentration of particles, flow characteristics of the solution, etc.). This behavior usually manifests as particle movement lateral to the flow direction, and there has historically been wide interest in understanding what controls this observed phenomenon. Understanding suspension behavior in flow is important for many different fields: from environmental studies that investigate river delta systems to the food, pharmaceutical, or coatings industries; other possible applications of suspensions involve improving filtration schemes and optimizing cell-sorting mechanisms for better diagnostic abilities[1]. The study of suspensions is especially important for understanding blood flow and the development of lab-on-a-chip analysis tools.

In particular, the study of the flow behavior of blood, or similar deformable particle suspensions, has important implications for the development of better drug delivery vehicles, improving the wound healing response, and for the development of separation devices that target cells of interest (i.e. leukocytes or cancer cells). Two primary migration phenomena have been observed in blood flow. The Fåhræus-Lindqvist effect is significant when blood is flowing through blood vessels with small diameters (<300 µm). The red blood cells (RBCs) migrate towards the center of the vessel, leaving a cell-free space near the vessel walls. This serves to reduce the viscosity of the suspension and encourage flow. The second phenomenon is known as margination. This behavior is classified as the outward migration towards the channel walls of the larger leukocytes (white blood cells) and the smaller and more rigid platelets, while RBCs aggregate towards the center of the flow channel. This behavior can be manipulated for improving the applications listed above, but the physics that controls the motion of these cells is still not yet fully understood. For example, the thickness of the cell-free layer controls how long it takes platelets to migrate to the vessel walls when they are needed to stop bleeding. If platelet transport was controlled solely by diffusion, this process would be excessively slow. Understanding platelet migration is just one important application of studying migration behavior in suspensions[2]. Targeted drug delivery particles are another useful application of studying migration behavior. These particles are more effective if they exhibit margination and remain near the vessel walls; determining what controls or enhances margination allows for better medicines to be designed[3].

In an attempt to elucidate the driving forces of particle migration, several sets of experiments and simulations have been performed. The following sections discuss the different migration regimes that have been observed; this migration space can be differentiated by particle deformability, particle concentration, and flow regime (characterized by Reynolds number, Re). In the limit of investigating the collective flow behavior of suspensions of deformable particles, very few experiments have been done that do not solely use suspensions of blood; in general, the collective behavior of deformable particle suspensions is still an open question[4,5]. There have been a few attempts to investigate this area with simulations; however, there is a need for a model suspension that can access a wider parameter space (in terms of size, deformability, shape, etc.) than that which the typical RBC offers.

Vesicles can serve as a first order approximation for cells in flow; in particular, they are a good model for RBCs because they display similar dynamic behaviors: vesicles display tumbling (end over end flipping in the flow direction) and tank treading (the vesicle maintains a constant orientation and shape with regards to the flow, with a membrane that is rotating around the inner fluid) that have also been observed in RBCs[5]. Vesicles are comprised of a lipid membrane that encloses, and is surrounded by, an aqueous solution. The membrane is composed primarily of phospholipids; these phospholipids typically have two fatty acid groups that are strongly hydrophobic attached to a polar head group that may or may not be charged. The amphiphilic quality of these lipids causes them to form certain structures in the presence of aqueous solutions. This process is entropy driven. Sizes, shapes, and lamellarity of vesicles depends on the lipid composition of the membrane and how they are generated. Giant unilamellar vesicles (GUVs) have diameters of 1-300 μm[6]. These traits give vesicles the potential to access a much wider size and deformability range than what is attainable with RBC investigations, making them useful to study as a model deformable particle suspension. Microfluidic devices are a useful tool for these experiments as they offer an accessible and low-cost way to directly observe suspension flows in channels at relevant physiological length scales. The main challenge with using vesicles or other deformable particles is that these suspensions are not yet commercially available and must be manufactured in-house. Depending on the generation protocol, it can also be challenging to obtain monodisperse suspensions (suspensions composed of particles that are all the same size). Still, there is value in studying suspensions that are not perfectly monodisperse; the possible effects that particles of different sizes have on each other in both dilute and concentrated flows is another open question that has important implications for understanding blood flow and designing better medications.
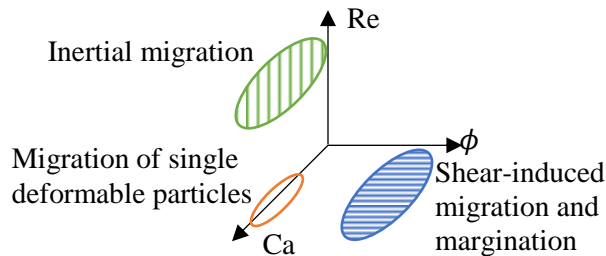
Figure 1.1 Migration of suspensions can be illustrated in terms of three key parameters.

1.1.2 *Migration parameters*

While migration of particles can depend on a host of different parameters, this space can be roughly differentiated by a few key variables, namely: Reynolds number, suspension volume fraction, and component deformability (see Figure 1.1). Reynolds number (Re) is defined as

$$Re = \frac{\rho_f \langle v \rangle D_h}{\mu_f}$$

where ρ_f is the density of the aqueous medium, $\langle v \rangle$ is the average velocity in the channel, D_h is the hydraulic diameter of the flow channel, and μ_f is the viscosity of the suspending fluid. Re provides information about the flow in the channel. Migration studies generally take place in either low Re conditions (Re $\ll$ 1, known as Stokes flow) or at finite Re (Re $\sim \mathcal{O}[10\text{-}100]$)

where fluid inertia becomes significant. Suspension volume fraction (ϕ) is classified as the ratio of the volume of solute particles to the volume of the suspension:

$$\phi = \frac{\text{volume particles}}{\text{volume suspension}}$$

It provides insight into the concentration of the suspension and the likelihood of particle-particle interactions. Deformability is generally quantified by Capillary number (Ca), but can be left as a qualitative descriptor here, since the definition of Ca depends on the deformable particle in question. Ca describes how the particle is affected by the flow; it is the ratio of viscous forces to a surface related restoring force (related to either surface tension for drops, bending modulus for vesicles, or shear modulus for elastic capsules). For vesicles, the Ca compares the external flow timescale with the membrane deformation relaxation time to quantify the relative strength of the hydrodynamic relative to the bending forces[5]. In the case of vesicle suspensions, Ca is defined as

$$Ca = \frac{\mu_f \dot{\gamma} a^3}{\kappa}$$

where a is the effective vesicle radius, κ is the bending modulus, and $\dot{\gamma}$ is the characteristic shear rate in the channel, defined as $\langle v \rangle / D_h$ [7]. In Figure 1.1, rigid spherical particles lie in the plane where deformability is zero; in works that investigate the migration behavior of deformable particles, Ca can range from 10^{-3} to 10^5. This range is fairly large due to the diverse array of particles (drops, capsules, vesicles, etc.) that have been used in migration studies; vesicles in particular are able to access a wide range of Ca because their ability to deform is dependent both on the membrane bending modulus and whether or not their membranes have excess surface area. A vesicle has excess surface area if it is not perfectly spherical (the configuration with the least surface area for a given volume). Unlike drops and elastic capsules, the surface area of a vesicle is constant – a bilayer membrane cannot deform through stretching, only bending. Without excess surface area, the only shape a vesicle can maintain is a sphere[5], giving them the ability to seem much more rigid than the bending modulus alone might imply.

1.2   Migration regimes
1.2.1   Migration in low Re and low ϕ conditions

In studies that focus on low Re flows (primarily in the Stokes regime, Re $\ll$ 1) where inertia does not contribute to any migration behavior, deformable and rigid particles exhibit different behaviors. Here, low ϕ indicates either single particle studies or dilute suspensions such that the particles are not interacting. Experiments investigating hydrodynamic interactions showed that vesicles are able to influence surrounding vesicle shapes and orientations even at volume fractions as low as 8-13%[5]. In the limit of dilute ϕ, rigid particles do not migrate due to the reversibility of the flow. Deformable particles, however, are able to migrate in this regime if there is a confining wall present[8,9] or if there is a gradient in the shear rate, as in Poiseuille flow[8].

This problem has been studied extensively both experimentally[10] and computationally[11,12] with good agreement between the predicted behavior and the experimental observations for both vesicles and RBCs[5]. Coupier et al. observed the migration of single vesicles in Poiseuille flow at low Re. The migration of these deformable vesicles to the channel centerline was credited to the combined effects of the wall proximity and the shear gradient of the velocity profile[10]. Farutin

and Misbah[11] predicted that the migration direction of a vesicle or red blood cell (RBC) in Poiseuille flow may not always be towards the channel center. Highly deformable vesicles (high Ca) that did not have a viscosity contrast between the inner and outer fluids tended to migrate inwards, but if there was a viscosity contrast, migration is predicted to move away from the axis. For vesicles with a moderate Ca, the migration and final equilibrium position varied; the vesicle is able to settle at either the channel center or a position slightly off of the axis. Vesicles with low Ca (more rigid vesicles) exhibit final positions away from the center of the flow. As Ca decreased, the final position moved further off of the center[11]. Abkarian and Viallat studied the problem of vesicles in wall-bound shear flows. They posited that the deformability of the vesicles allows them to undergo asymmetric shape changes and a tilted orientation in shear flows. This shape change induces a fore-aft asymmetric pressure field around the vesicle, and a viscous lift force then works to push the vesicle away from the wall. This observation was applied to blood flow, and it was theorized that the shape of RBCs allows for the maintenance of a cell-free layer near the vessel walls, in contrast with the more spherical white blood cells (WBCs) that tend to remain in the depletion layer[12]. Abreu et al.[5] put forth a comprehensive review of vesicles in different flow conditions, concluding that the behavior of a single vesicle in flow is determined by a combination of the membrane parameters and hydrodynamic forces. In addition to the findings discussed above, it was noted that vesicles tend to migrate to regions with minimal shear in Poiseuille flow. Vesicles with small excess area (quasi-spherical) were predicted to have a stable equilibrium position at the channel center and exhibit bullet- or parachute-like shapes. Vesicles with larger excess area are not predicted to favor these axisymmetric shapes; instead, asymmetric slipper shapes (also observed for RBCs) that sit off-center are the stable configuration[5].

To summarize, at low Re and low ϕ, deformable particles migrate, while rigid particles do not. The migration of deformable particles is driven by shear gradients in flow and by the presence of confining walls, but the final equilibrium position and particle orientation depend on the ability of the individual particle to respond to the flow (quantified by viscosity contrast, excess area, and Ca).

1.2.2 Migration in low Re and finite ϕ conditions

At low Re and finite ϕ, migration in both rigid and deformable particle suspensions has been observed. With suspensions of rigid spheres, this migration in Stokes flow is classified as shear-induced migration; it is characterized by the development of a particle depletion layer near the channel walls as the particles migrate towards regions of low shear in the channel[13]. This system has been studied experimentally[14–16] and with simulations[17]. Lyon and Leal also investigated bidisperse suspensions of rigid spheres and noted that at lower concentrations (while maintaining high enough ϕ to still observe particle interactions), the particles segregated by size in the channel, with the large particles dominating the channel center – a region of low shear – over the small particles. Smaller particles went to the low shear region when they were present at higher concentrations. The tendency of the large spheres to migrate towards regions of low shear is attributed to the gradients in collision frequency throughout the channel as well as the entry length difference between a small particle and a large particle: larger particles reached the channel axis first, thus excluding smaller spheres from that volume. Still, even in this idealized system, what drives the particle segregation by size is not completely clear[18]. A comprehensive review of migration in confined flows of multicomponent suspensions by Kumar and Graham[3] covers the different approaches that have been taken to model rigid sphere suspension behavior.

4

A diffusive flux model has been developed to capture the experimentally observed increase in particle concentration in regions of low shear. This model utilizes gradients in collision frequencies due to gradients in the shear rate that come with Poiseuille flow. Another modelling approach is the suspension balance model. This method uses the stresses associated with the different suspension phases (fluid vs particulate phases). It also produces an increase in volume fraction towards the center of the channel in compensation for the decreasing shear rate. Both the diffusive flux and suspension balance model experience problems describing the suspension behavior in regions of zero shear (namely, the channel center). The last model for monodisperse rigid particles described by Kumar and Graham is a Fokker-Planck model based on stochastic movements of particles; this method yields expressions similar to that of the diffusive flux model. For polydisperse suspensions of rigid spheres, Kumar and Graham note that a phenomenological model has been developed that is similar to the diffusive flux model. The migration behavior is controlled by non-uniform particle concentration and shear rate. This model predicts that larger particles are expected to have a larger flux towards regions of low collision frequency and shear rate (the channel axis) at the expense of smaller particles[3].

Concentrated suspensions of monodisperse deformable particles also develop a cell-free layer near the channel walls. The thickness of this depletion layer is determined by the wall-induced migration and diffusion throughout the channel due to particle interactions[3]. Clausen et al. has found through simulations of a suspension of monodisperse deformable capsules that these systems exhibit shear thinning – possibly due to the development of a cell-free layer near the walls and higher packing of deformable particles towards the center of the channel[19]. Migration in polydisperse suspensions of deformable particles (e.g. blood) has been observed and is termed margination. Studies of rigid sphere suspensions cannot explain this phenomenon, and this behavior has yet to be fully explained by simulations and available experimental data. A full understanding of the margination phenomenon is prohibited by the lack of well-controlled investigations that have the ability to change only one suspension property at a time[3]; vesicle suspension experiments could prove valuable in this area of study.

Margination is a migration behavior occurring in this regime (low Re, finite ϕ) that is classified by aggregation of red blood cells along the channel axis and the occupation of the cell-free layer by white blood cells (WBC) and platelets, both types of cells are more rigid and differently sized than red blood cells. WBC margination is a part of the body's immune response. Experiments have shown that this is influenced more by changes in the shear rate, rather than the hematocrit (ϕ in blood suspensions) in the channel; higher shear rates prevented RBC aggregation to the channel center, which in turn decreased the WBC margination. Simulations found that if the WBC was made to be more deformable, margination behavior was also decreased[3]. Platelet margination is important for hemostasis. In contrast to WBC margination, platelets were found to increasingly marginate with higher shear rates. The driving factor for margination of platelets is attributed to the size difference and pair collisions between RBCs and platelets, rather than the deformability difference[3].

Several simulations investigating margination by studying suspension behavior in bulk shear flows, as well as confined channel flows, were able to show that margination is due to a combination of wall- or shear-induced diffusive forces (driving particles to the channel center) and hydrodynamic particle-particle collisions (driving particles to the depletion layer)[2,20,21]. The velocity towards the wall depends on the size and shape of the particles, as well as the particle-particle interactions. When investigating the effect of membrane deformability, Kumar et al. found that floppier particles preferred moving towards the channel center, while stiffer particles

preferred migrating towards the channel walls; this resulted primarily from the difference in particle responses to heterogeneous collisions: stiff particles were displaced further (laterally) from their original path than the more flexible particles when they encountered each other. It is interesting to note, however, that at higher volume fractions (ϕ), the cell-free layer thickness was reduced and the segregation of particles by rigidity was driven both by the differing responses to pair collisions and the wall-induced migration velocities of the individual components. When investigating the effect of size on migration behavior, large particles were found to migrate towards the channel axis and smaller particles tended to move towards the channel walls. The margination of the smaller particles was found to be driven by the differences in wall-induced migration velocity between differently sized particles instead of the influence of heterogeneous pair collisions. However, if large particles were made to be sufficiently rigid, they were found to marginate towards the channel walls, and if small particles were made to be sufficiently deformable, they were observed to migrate towards the channel center; in these margination cases, it was determined that particle-particle collisions were the significant factor[21]. The deformability, rather than the size of the particle, was a more significant predictor of migration behavior in this study, and the driver for migration in a suspension with particles of different deformability is the particle response to heterogeneous collisions between rigid and deformable particles. A large body of simulation and modeling work has been collected thus far to study how regions of low shear become enriched with particles in this migration space; there have also been considerable experimental investigations with rigid sphere suspensions, however, well-controlled experimental studies of these phenomena with model deformable particle suspensions have yet to be performed in this migration regime.

1.2.3   Migration in finite Re and low ϕ conditions

At finite Re and low ϕ, inertial effects become noticeable and migration with both rigid and deformable particles can be observed. Initial experimental evidence of inertial migration was collected and reported by Segré and Silberberg in 1962 [22]. They observed rigid spherical particles migrating to equilibrium positions between the channel center and channel walls in Poiseuille flow at moderate Re. In this migration regime, Re usually ranges from 10-500, and ϕ is dilute enough for particles to not interact with each other, i.e. $\phi < 1\%$ [23]. In certain channel geometries as Re increases, it is possible to observe more equilibrium positions that were previously unstable. After a certain point, inertial focusing degrades with higher Re[24]. The proximity of the channel walls can enhance inertial migration; particle Reynolds number (Re_p) can quantify the extent to which wall-induced lift affects the particles in flow.

$$Re_p = Re\left(\frac{a^2}{D_h^2}\right)$$

Here, a is the particle diameter. Generally[3], inertial migration is observed when $Re_p \rightarrow 1$. The discovery of inertial migration set off a number of experimental[23] and theoretical[25,26] investigations in an attempt to explain the mechanism of this migration behavior. Zhang et al. summarizes the forces that contribute to the inertial migration phenomenon: a Magnus force from slip-rotation, a Saffman force from slip-shear – the difference in velocity between the particle experiencing wall drag and the fluid flow[27], a wall lift force due to flow around the particles being disturbed by the presence of a wall, and a shear-gradient lift force[28]. The balance of these forces determines the final equilibrium position of the particles in the channel, and

several relationships have been derived to predict the entry length over which the particle focusing occurs[28–31].

With deformable particle suspensions, there is some evidence that inertial migration may enhance focusing towards the center, instead of focusing towards an equilibrium position that is between the channel axis and the walls[32,33]. Kilimnik et al. used 3D simulations to investigate inertial migration of deformable capsules and found that deformability increased the wall-induced lift force that directs particles towards the channel center. They also provided evidence that larger and more deformable particles migrated to equilibrium positions closer to the midplane of the channel relative to smaller or stiffer particles[33,34]. Interestingly, Kilimnik et al. showed that the equilibrium positions of the deformable particles were not affected by Re in the range of 10-100, but a study by Shin and Sung showed that with increasing Re, elastic capsules first migrated to equilibrium positions that were closer to the channel walls, before eventually migrating to positions closer to the channel center.

Inertial migration has been employed in several lab-on-a-chip applications, such as removing circulating tumor cells, white blood cells, bacteria, or plasma from blood suspensions[35–38] because of its ability to focus different suspension components to different positions in the microfluidic channel. Channel geometry, Re, and particle deformability, size, and shape are all properties that play a role in determining the focusing position[39,40]. Other device properties can potentially affect the focusing behavior as well: by introducing curves or spirals in the design, another force (Dean drag) is introduced and contributes to the inertial lift. Dean flow can work to reduce the number of equilibrium positions in the channel[41], offering another degree of control over where the particles migrate. Gossett et al.[41] also provided evidence that introducing curved geometries increased the Re range where optimal focusing occurs, widening the useable design space for these devices.

Much of the inertial migration studies involving deformable capsules or vesicles are currently computational; there is a need for experiments with model suspensions in this space. While there have been several experimental and theoretical investigations into inertial migration of monodisperse rigid sphere suspensions, to our knowledge, a study of how polydispersity affects either the focusing positions or the entry length of rigid or deformable particles has yet to be published. Vesicles can offer interesting dynamic behavior in moderate Re flow, especially in the transition between the tumbling and tank treading phases[42]; as vesicles have the potential to access a wide range of the relevant parameter space – deformability can be controlled by selecting different lipids to compose the membrane, some generation protocols offer control over vesicle size, etc. – they offer a way to systematically study and answer some of the open questions as to what controls migration in these flow conditions.

1.2.4 *Migration in finite Re and finite ϕ conditions*

Studying the migration of individual particles provides insight into the driving forces that control how these particles move laterally to the flow; however, the behavior of an individual particle does not always directly translate to the collective behavior of these particles when they are concentrated enough to interact with each other. The suspension ϕ and resulting rheology can affect migration behavior; thus, it is useful to also observe and develop models for more concentrated suspensions[43]. An experimental study by Han et al.[44] expanded on the pioneering work by Segré and Silberberg and observed inertial migration of rigid sphere suspensions in a tube geometry over a wider range of Re_p and ϕ. They observed inertial focusing behavior of particles to an annulus between the axis and the walls similar to that displayed by dilute

suspensions up to $\phi \sim 10\%$. Towards the upper range of concentration, at $\phi = 40\%$, particles moved to the center of the tube in a similar fashion to the earlier discussed shear-induced migration of concentrated sphere suspensions. At the intermediate concentrations, however, these behaviors appeared to be superimposed, with spheres concentrating both at the center and to an annulus in between the channel axis and the walls. Their results indicated that inertial lift becomes significant as Re_p becomes larger than 1 [44]. Kazerooni et al. conducted a study of inertial migration of rigid particle suspensions over a range of ϕ (up to 20%) in square channels. A depletion in the channel core was observed at Re = 550 and $\phi = 20\%$, as similar forces act to move the particles to specific equilibrium positions in between the channel axis and the channel wall; however, due to the higher concentrations, the particles were not able to focus to the few equilibrium positions in the channel that were observed for the dilute suspensions[45]. Instead, they spread over a wider band in the channel, whose width increased with the suspension concentration; particle interactions were predicted to disperse particles throughout the focused band into a continuous annulus, even in square channels[44,45].

When deformability is introduced, simulations by Krüger et al. showed that the migration behavior of non-dilute suspensions ($\phi = 10\%$) at moderate Re can be divided into three categories. At lower Re (Re $\sim$ 6), deformable particles were expected to migrate towards the channel center more than rigid particles, but in both cases this migration resembled the shear-induced migration behavior that was discussed in the previous sections. A moderate Re (Re $\sim$ 50) study confirmed the expected migration behavior for rigid spheres (focusing to positions in between the channel center and the walls) and predicted that deformable particles migrate instead to the channel center – as they did in the low Re case. With higher Re (Re $\sim$ 417), Krüger et al. saw a suppression of the Segré-Silberberg effect for the rigid spheres: particles were now distributed throughout the channel. For the deformable particles, however, focusing to the channel center was noticeably enhanced. These focusing behaviors still depended on wall-induced and shear-induced lift forces (characteristic of inertial focusing), however, the effects of the deformation of the particles in the presence of Poiseuille flow and the particle-particle interactions must be considered as well. The inertial effects generally sent the particles towards the positions in between the channel center and the walls, in favor of developing a particle-depletion area at the channel axis. As the deformability of the particles increased, it became the more significant source of lift. The effect of deformability was to drive the particles towards the channel center. Particle-particle interactions generally lead to dispersion of particles throughout the channel, but Krüger et al. showed that at large enough Re and Ca, particle interactions became cooperative, and particle focusing to the center was predicted to increase[46]. With increasing suspension concentrations, the focusing behavior is expected to degrade[47,48].

The parameters important for quantifying focusing in this regime include Ca, Re, ϕ, and confinement – generally determined by Re_p to compare particle diameter to channel size. The inertial effects discussed in the previous section continue to influence the observed migration behavior; however, in this regime where ϕ is finite, particle interactions must also be considered. Polydispersity can complicate the migration of suspensions as it introduces an additional parameter to control[47]; the effect it has is still relatively unclear, though it is initially expected to increase the migration entry length[48]. As with several of the migration regimes presented above, there is a distinct lack of experimental investigation into this area, particularly with deformable particle suspensions. Again, vesicle suspensions could be used as a model suspension to gain insight into the physics of suspension migration. Additionally, it would be interesting to investigate the effects of polydispersity on the collective suspension flow behavior. An ideal

system, namely that of a rigid sphere suspension that is composed of spheres of two or more distinct sizes, would be a good starting point for this study before moving to deformable particle suspensions or even mixed particle suspensions composed of particles of varying deformability and size.

1.3   Structure of dissertation

The objective of this project is to conduct an experimental investigation to determine the driving forces behind the collective migration behavior of deformable and polydisperse particle suspensions, in an attempt to better understand blood flow and improve lab-on-a-chip diagnostic devices. Chapter 1 introduces the problem and relevant migration scenarios that have been studied before. Chapter 2 dives into the vesicle generation process, and the challenges associated with making deformable particle suspensions. Chapter 3 discusses efforts to reduce the polydispersity of the vesicle suspensions using microfluidic separation devices. At this point, the separated vesicle suspensions are still somewhat polydisperse; to obtain a better idea of how polydispersity affects suspension behavior in flow, inertial flow experiments are first conducted with rigid sphere suspensions, a system with flow behavior that has adequate documentation for the monodisperse case; these are discussed in Chapter 4. Chapter 5 reviews the main conclusions and outlines future experimental directions that have the potential to offer more insight into what factors are important in suspension migration.

Chapter 2. Vesicle generation

2.1   Introduction

2.1.1   Applications and desired traits for vesicles

Vesicles are defined as bilayer membranes that both enclose an aqueous solution and are surrounded by an aqueous solution. Vesicles in the size range of 1-300 μm are termed "giant." Due to their size, giant unilamellar (single lipid bilayer) vesicles (GUVs) are useful for studying and modeling the properties of cells and cell membranes (e.g. membrane dynamics, membrane fission or fusion, shape changes, etc.). GUVs are also extremely important for artificial cell studies and the development of biosensors or microreactors. These applications generally require unilamellar vesicles with particular sizes or shapes; however, controlling the size and polydispersity (or broadness in the distribution of vesicle diameters) of vesicle suspensions can be extremely difficult. A method that consistently and reproducibly generates monodisperse, unilamellar vesicles of different sizes is desired, but a reliable protocol has yet to be developed.

2.1.2   Challenges of vesicle generation

Giant vesicles are difficult to prepare because their sizes and properties depend heavily on experimental conditions. Giant vesicles are not the most favorable thermodynamic state for these lipid membranes; while they can be trapped in this state, they only remain as giant vesicles for a limited amount of time before the suspension becomes unstable. The properties of the membrane (i.e. bending rigidity) can change over time, so there is a relatively short window of time (on the order of days or a couple weeks) to work with the vesicles before they degrade and become unusable – instead of vesicles, the suspension becomes sparsely populated with lipid aggregates. Because of the thermodynamics, obtaining giant vesicles in the first place can be a challenge; it is much easier to obtain vesicles with diameters that are less than 1 μm through sonication or extrusion methods. With the methods that produce GUVs, often there is no way to control the size or broadness of the size distribution. Some methods utilizing microfluidics offer ways to control the size, however with these methods, one of the challenges lies in obtaining a single lipid bilayer – often oil remains in the bilayer which can affect the membrane properties and the subsequent vesicle behavior in channel flows.

2.1.3   Methods overview

Several methods used to generate giant unilamellar vesicles (GUVs) are covered in a thorough review by Walde et al.[49] and are summarized here. The gentle hydration method, initially proposed by Reeves and Dowben in 1969, simply involves evaporating a lipid/solvent mixture onto a flat surface and exposing that surface to an aqueous medium[50]. The quality of vesicles produced via this method depends strongly on experimental conditions, and it can generate mostly multilamellar vesicles if the apparatus is agitated even slightly during vesicle formation. This method is inconsistent in its ability to produce giant vesicles with the desired unilamellar membrane. Electroformation offers a reproducible way to produce unilamellar, spherical vesicles. This method is adapted from the gentle hydration method by applying an electric field and will be covered in more detail in the following sections.

Another method for vesicle generation involves using water-oil emulsions. Lipid-stabilized or surfactant-stabilized water droplets are sent through an oil-water interface. Usually lipids are mixed into the oil layer, and if the interface is not disturbed, as the droplets pass through to the aqueous layer (due to density differences between oil and water), the droplet picks

up another lipid layer, thus completing the bilayer membrane. It is still possible to have multilamellar vesicles with this method, and oil is likely to remain in the bilayer. Due to the way the vesicle is formed, it is also possible to have an uneven distribution of lipids around the membrane.

Continuing in this theme, water-oil-water double emulsions have also been used as a vesicle generation method[51–53]. Generally, these double emulsions are formed using microfluidic devices; the excess oil is later extracted, leaving behind the lipids to form a bilayer membrane. While this method is able to produce high yields of monodisperse vesicles, it is very sensitive to experimental start-up conditions. Additionally, the device must be prepared so that some channel sections are hydrophobic, while other parts of the channel favor hydrophilic wetting of the walls. This selective channel preparation is very difficult to achieve. If it is not done properly, the emulsions are unable to form, as the oil layer prefers to wet the generally hydrophobic channel walls. Also, this double emulsion method tends to leave oil behind in the bilayer and the presence of too many lipids in the oil layer can cause lipid aggregates to form in the membrane after the oil extraction step.

Another method includes fusion of smaller vesicles into larger vesicles. This method is not thermodynamically favorable as the bilayer membranes must be opened. This method offers no control over size or lamellarity and is not commonly used[49,54]. A newer protocol is analogous to an inkjet printer. A planar lipid bilayer is set up and an aqueous solution is jetted or blown through the bilayer[55]. This method can be very particular to how the microfluidics are set up, and the bilayer may contain excess oil. Other methods that are not mentioned here are generally less common and often lack control over vesicle size and suspension polydispersity. When generating vesicles, often only specific lipid combinations are successful with certain methods, so optimization of the chosen technique is usually required.

2.1.4 *Electroformation overview*

The electroformation technique offers a relatively consistent way to produce large unilamellar vesicles that are comparatively uniform in size (when considering the other ways of producing vesicles). Angelova and Dimitrov pioneered the electroformation technique in 1986 by applying an electric field during the gentle hydration process[56,57]. They postulated that the type, composition, and amount of lipids used, along with the applied electric field parameters and hydration medium, could control the production of the electroformed vesicles.

The mechanism of electroformation is posited as follows[56,58]. Lipids are first dissolved in a solvent and then deposited onto an electrode. The solvent is evaporated off, and the lipids organize into stacked bilayer sheets. An aqueous solution is introduced and penetrates the defects in the bilayer sheets. The water first hydrates the polar headgroups of the lipids, driven by hydration forces (the reduction in free energy from water molecules arranging themselves around charges) and undulation forces (entropy driven – more space between bilayers allows for more bending modes). This causes the lipid layers to swell. As the spacing between the bilayers is increased, electrostatic interactions can become important if using charged lipids (lipid bilayers with like charges facing each other have a repulsive effect); however, if using a system with zwitterionic lipids, such as 1,2-dioleoyl-*sn*-glycero-3-phosphocholine (DOPC), this repulsive force is likely negligible. The presence of non-electrolytic compounds such as monosaccharides (e.g. glucose) or disaccharides (e.g. sucrose) can induce separation of lipid bilayers composed of zwitterionic amphiphiles by utilizing osmotic forces. The concentration gradient between molecules in the bulk solution and their concentration in the inter-bilayer space can drive more

water in between the bilayers (to reduce the osmotic pressure difference), leading to separation and maintenance of the unilamellar membrane.

The application of an electric field is thought to enable lipid swelling and separation (leading to more unilamellar vesicles) in a few ways. If the lipids are charged, electrostatic repulsion between the similarly charged electrode and the charges on the lipid bilayer can lead to bilayer separation[59]. In an AC field, it is postulated that the switching field polarity induces mechanical stress and agitation of the lipid bilayers; this enables vesicles to form and grow. Once they grow large enough to encounter neighboring vesicles, they are able to fuse together into larger vesicles. Many vesicles remain tethered to the electrode throughout this process; attempts to detach the vesicles can involve changing the applied field parameters (decreasing the frequency) or by mechanically agitating the electroformation cell[60]. It is also thought that the electric field plays a role in decreasing the membrane surface tensions. This destabilizes the membrane and enhances bending of the membrane (important for the closing of the vesicles).

Previous electroformation studies indicate that changing the electroformation parameters (i.e. type of lipid, suspending medium, how the lipids are applied to the electrode, type and parameters of the electric field, and time of exposure) can affect the size, polydispersity, and yield of vesicles[56–58,60–62]. Besides those listed previously, there are many other adjustable steps to the electroformation protocol that may influence the process (e.g. composition and total concentration of lipid mixture, solvents the lipids are dissolved in, the spacing between the electrodes, whether or not ramping or detachment protocols are used for the applied field, etc.). Work done by Estes and Mayer[62] showed that spincoating the lipid mixture onto the ITO slide may lead to higher incidences of large vesicles compared to using a syringe to deposit and spread droplets of the lipid mixture on the slide (though the polydispersity of the suspension may not be affected). They mentioned that optimization of this method with different lipid mixtures involves choosing an optimal lipid concentration and solvent mixture to allow for proper wetting of the electrode. They offered a general recommendation for the spincoating method.

Politano and coworkers[60] postulated that vesicles produced via electroformation can be controlled by changing the applied electric field. At E = 0.212 V/mm, they observed that vesicle diameter decreased as the frequency of the applied field increased. The polydispersity of these vesicle suspensions also decreased with the increase in frequency. However, for electric fields above 0.212 V/mm, there was no discernible size dependence on the field frequency. Optimal ranges for field frequency and strength were seen by Politano; a suggested reason for this behavior was that the applied field affects how the vesicles and bilayers are agitated, which may enable separation and further vesicle formation. The AC electroosmotic flow amplitude increases with the applied field strength; at low strength and high frequencies, the flow amplitude is diminished and the vesicles were not observed to swell. On the other hand, if the electric field is too strong, the lipids can become detached from the electrode almost immediately. These electroosmotic effects have an optimal working range depending on the aqueous medium that the electroformation is taking place in. This means that if you are at an adequate field strength, but over the recommended frequency range, or are at a good frequency, but at too low field strengths, there will not be enough oscillation of the solution (and thus, not enough agitation of the hydrated bilayers) for the bilayers to separate far enough away from the surface to form vesicles. Politano et al. also noted that the lipid charge can also affect the response of the bilayer membrane to the applied electric field. It was suggested that more hydrophilic lipids were more easily hydrated, making separation and GUV formation more probable[60].

12

In comparison to other vesicle generation methods, electroformation is a reliable technique. It requires a function generator, but no other specialized equipment. However, there are a few caveats: if too many lipid layers are initially deposited onto the ITO slide, multilamellar vesicles can still form. If too few lipid layers are deposited onto the electrode, it is theorized[60] that the electric field may not be strong enough to overcome van der Waals attractions and separate the bilayers. The hydration conditions, amount and uniformity of the deposited bilayers, and the applied field can all affect the formation of GUVs. Optimizing this technique for different lipid combinations is still required, and even then, vesicle suspensions are generally polydisperse. The rest of this chapter describes a parametric study that was conducted to optimize the electroformation protocol for fluorescent vesicles to be later used in studies of suspension flow behavior.

2.2 Materials and methods

2.2.1 Electroformation protocol

Vesicles were prepared with several different electroformation protocols, adapted from earlier work by Jakob Spjut[63]. For each electroformation experiment, the lipids used were DOPC (Avanti Lipids) and 1-oleoyl-2-{6-[(7-nitro-2-1,3-benzoxadiazol-4-yl)amino]hexanoyl}-*sn*-glycero-3-phosphocholine (NBD-PC, Avanti Lipids). The total lipid concentration (in mg ml^{-1}) was one of the parameters that was varied; however, the ratio of DOPC to NBD-PC in the lipid mixture was kept constant, with each experiment utilizing a mixture composed of 99% DOPC and 1% NBD-PC. The lipids were dissolved in a 5%v/v acetonitrile (Fisher Chemical), 95%v/v chloroform (Fisher Chemical) solvent mixture. This lipid mixture was deposited onto indium tin oxide (ITO) coated glass slides (Delta Technologies, Limited) with varying deposition methods. The residual solvents in the lipid mixture were evaporated under vacuum for 30 minutes.

Two strips of copper tape were placed on either side of a 1.6mm thick rubber gasket that had a small gap along one edge. The electroformation cell was assembled by sandwiching the rubber gasket between two lipid-coated ITO slides; the cell was held together with small binder clips. A 0.2-0.4 μm filtered 100 mM sucrose solution was injected into the electroformation cell through the small gap in the rubber gasket; this gap was then sealed with a bit of polymer clay (Sculpey). The copper tape strips should be in contact with the ITO electrodes to connect the cell to the function generator (Agilent 33220A). The applied electric field parameters were also varied and are described in more detail in the following section.

Following the application of the electric field, vesicles were carefully removed from the electroformation cell with an 18G syringe needle. The quality of the vesicles in these suspensions degrades over time, and it is recommended to use them for further experiments and analysis within a week or two. The electroformation protocol described in Appendix A is the method that was used for all later vesicle experiments.

2.2.2 Size analysis

The procedure used to measure the size distributions of the electroformed vesicle suspensions can be found in Appendix B. The diameters of vesicles from a sample volume of each suspension were measured. The mean diameter and standard deviation from the distribution of measured sizes were used to quantify and compare the sizes and polydispersity of the vesicles from different experiments. The polydispersity index (PDI) is an additional parameter that was used to quantify the broadness of the vesicle size distribution and is defined as:

$$PDI = 1 + \left(\frac{\sigma}{\mu}\right)^2$$

where σ is the standard deviation of the distribution of vesicle diameters and μ is the mean vesicle size. A PDI = 1 indicates the suspension is perfectly monodisperse.

2.3   Results and Discussion

Based on the hypothesis that careful control of the electroformation process may be a way to control the produced vesicle size or resulting suspension polydispersity, several experiments were performed. The effect of total lipid concentration, applied field time, deposition method, applied field parameters, and the inclusion of ramp or detachment protocols for the applied field were investigated. Figure 2.1 illustrates the dependence of average vesicle size on total lipid concentration (the combined 99% DOPC and 1% NBD-PC) and applied field time. This figure reports the average vesicle size for lipid concentrations of 1, 2, or 3.75 mg/ml for two different applied field times: 1.5 hours (protocol 1) and 2 hours (protocol 2) – see Table 2.1 for protocol details and Table 2.2 for diameter values. The error bars represent the standard deviation of the measured sizes from a sample of each produced suspension. The variation in size and suspension polydispersity indicates that total lipid concentration is not an effective way to control these traits, at least over this range of concentrations. Figure 2.1 hints that electroformation time may not offer an adequate solution to these issues as well.

Protocol	Applied field time	Deposition method	Applied field
1	1.5 hours	175 μl spincoated 600 rpm 4 min	Sine wave $V_{pp} = 3.39$ V $\lambda = 100$ Hz
2	2 hours		

Table 2.1 Key to electroformation protocols for Figure 2.1.
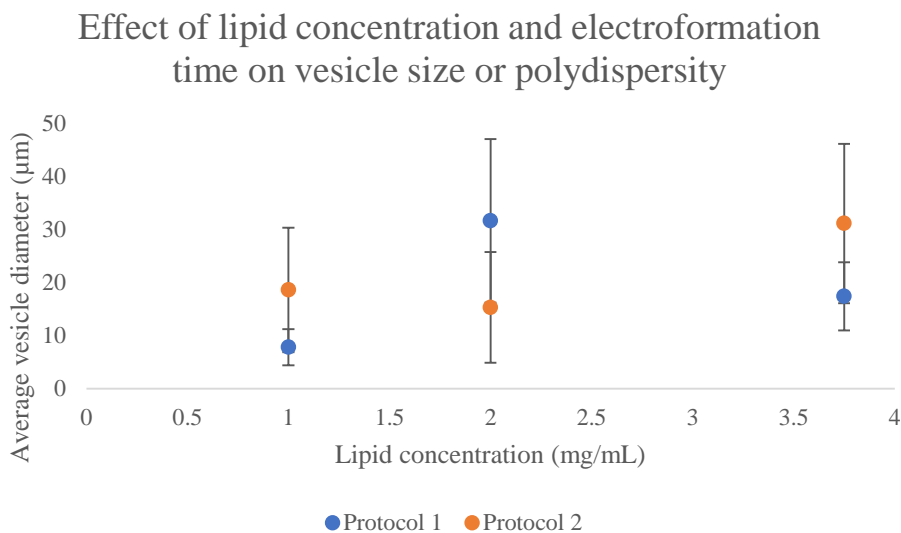
Figure 2.1 Effect of lipid concentration and applied electric field time on average vesicle diameter and suspension standard deviation.

Protocol	Total lipid concentration ($mg\ ml^{-1}$)	Mean vesicle diameter (μm)	Standard deviation (μm)	PDI
	1	7.8	3.4	1.19
1	2	31.6	15.4	1.24
	3.75	17.4	6.4	1.13
	1	18.6	11.7	1.4
2	2	15.3	10.4	1.47
	3.75	31.1	15	1.23

Table 2.2 Values for electroformation results in Figure 2.1.

The results of a more in-depth investigation into the possible effect of applied field time can be seen in Figure 2.2. Here, the time the electric field was applied was varied from 0.5 to 2 hours (see Table 2.3 for Protocol 3 electroformation parameters). The large variation both in mean vesicle diameter and suspension polydispersity (listed in Table 2.4) confirm that the time of the applied field after half an hour does not enable control over vesicle size or polydispersity – as the results from Figure 2.1 suggested.

Protocol	Total lipid concentration	Deposition method	Applied field
3	3.75 mg ml^{-1}	175 µl spincoated 600 rpm 4 min	Sine wave $V_{pp} = 3.39$ V $\lambda = 100$ Hz

Table 2.3 Protocol for Figure 2.2.

Effect of electroformation time on vesicle size
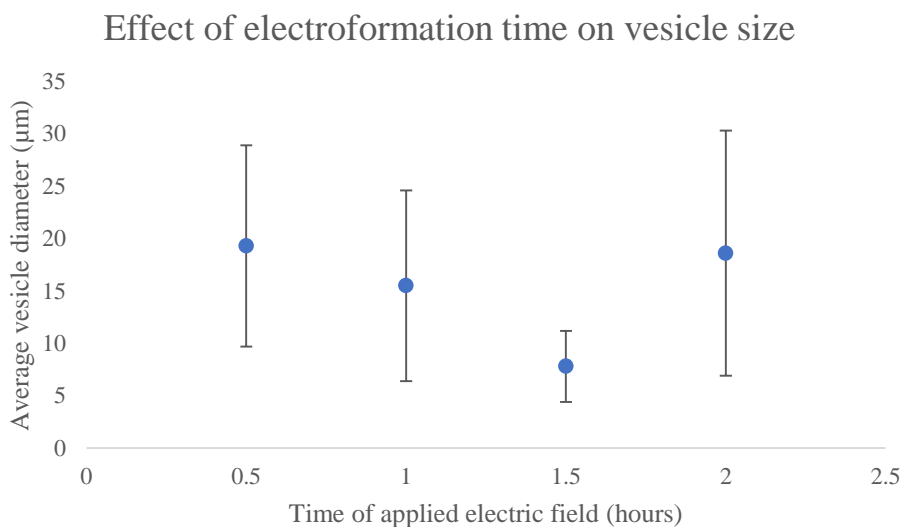
Figure 2.2 How the time of the applied field affects the resulting size and polydispersity of produced vesicle suspensions.

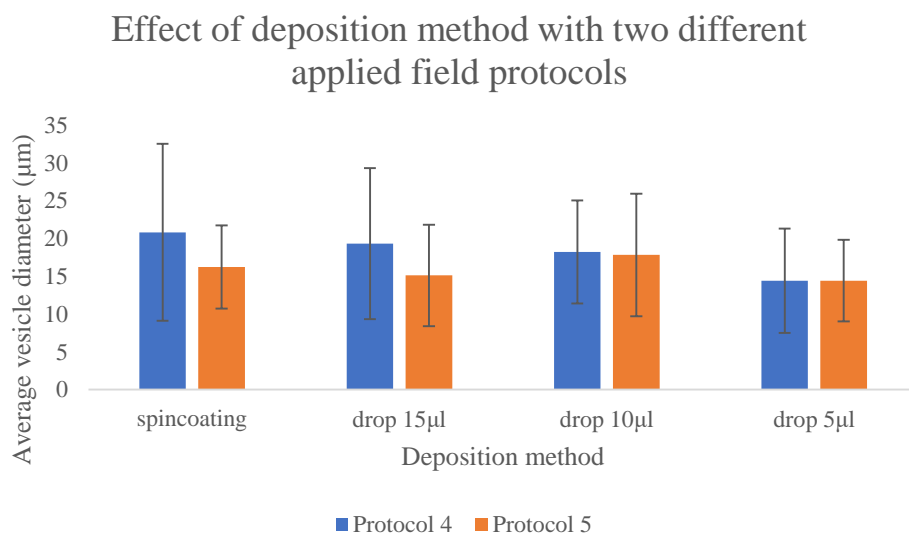| Protocol	Time of applied field (hours)	Mean vesicle diameter (μm)	Standard deviation (μm)	PDI
	0.5	19.3	9.6	1.25
3	1	15.5	9.1	1.34
	1.5	7.8	3.4	1.19
	2	18.6	11.7	1.40

Table 2.4 Data for electroformation results in Figure 2.2.

The next set of experiments involved studying the effect of how the lipids were deposited onto the ITO slide. Figure 2.3 shows the observed vesicle size and suspension standard deviation for four different deposition methods: spincoating and droplets of differing volumes. Two separate applied fields were used (see Table 2.5), one that utilized a ramping and detachment protocol (a ramping protocol involves gradually bringing the applied field up to its maximum value, the detachment protocol lowers the frequency at the end of the electroformation sequence) and one that just applied the maximum field value for 1.5 hours. As Figure 2.3 and Table 2.6 show, we were unable to observe a noticeable difference in the resulting suspensions after changing these electroformation parameters; they also provide evidence that the deposition method is not a good way to control resulting suspension size or polydispersity.

Protocol	Total lipid concentration	Ramp Sine wave; 0.5 hours	Applied field Sine wave	Applied field time	Detachment Square wave; 0.5 hours
4	2 mg ml^{-1}	V_{pp} = 0.05 V to 1.41 V λ = 10 Hz	V_{pp} = 1.41 V λ = 10 Hz	2 hours	V_{pp} = 2.12 V λ = 4.5 Hz
5	2 mg ml^{-1}	N/A	V_{pp} = 3.39 V λ = 100 Hz	1.5 hours	N/A

Table 2.5 Protocols for Figure 2.3.

Effect of deposition method with two different applied field protocols

■ Protocol 4   ■ Protocol 5

Figure 2.3 How deposition method, deposition volume, and applied field may control vesicle suspension properties.

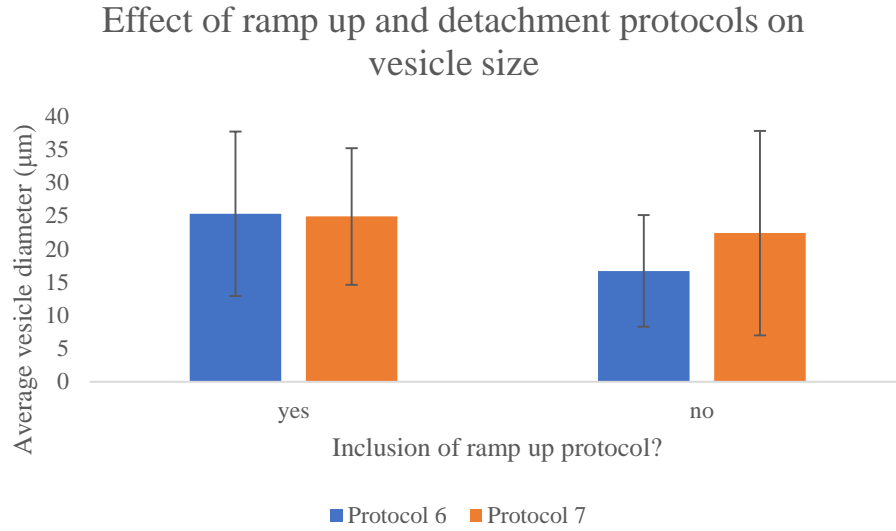| Protocol	Deposition method	Mean vesicle diameter (μm)	Standard deviation (μm)	PDI
4	Spincoat 175 μl	20.8	11.7	1.32
	Droplet 15 μl	19.3	10.0	1.27
	Droplet 10 μl	18.2	6.8	1.14
	Droplet 5 μl	14.4	6.8	1.23
5	Spincoat 175 μl	16.2	5.5	1.11
	Droplet 15 μl	15.1	6.7	1.20
	Droplet 10 μl	17.8	8.1	1.21
	Droplet 5 μl	14.4	5.4	1.14

Table 2.6 Data for electroformation results in Figure 2.3.

One of the last parameters investigated by this study involved the applied electric field (see Table 2.7). These experiments were an attempt to answer the question of whether or not to include a ramp up to the maximum field strength or a detachment protocol that would decrease the field frequency. Figure 2.4 and Table 2.8 contains the results from these experiments. From this data, it appears that the inclusion of either protocol has little effect on either the average vesicle size or broadness of the size distribution.

To confirm that electroformation produces vesicle suspensions that, while unilamellar, exhibit varying and fairly uncontrollable average size and suspension polydispersity, the day-to-day variation was investigated with three different protocols (Table 2.9). The results of this study can be found in Figure 2.5 and Table 2.10. Figure 2.5 illustrates the variation in average size and polydispersity of the resulting suspensions when using the same protocol over different days. The variation in mean vesicle diameter and suspension standard deviation observed over different days with the same electroformation protocol is on the order of the earlier variation that was observed when we were changing specific parameters of the electroformation process.

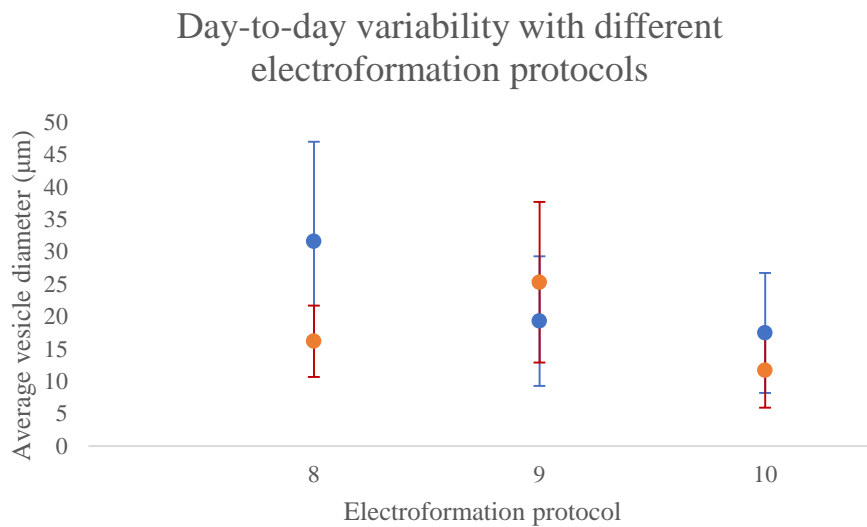| Protocol	Ramp	Applied field	Detachment	Total lipid concentration	Deposition method
6	Sine wave V_{pp} = 0.05 V to 1.41 V λ = 10 Hz 0.5 hours	Sine wave V_{pp} = 1.41 V λ = 10 Hz 2 hours	Square wave V_{pp} = 2.12 V λ = 4.5 Hz 0.5 hours	2 mg ml^{-1}	15 μl droplet
7	Sine wave V_{pp} = 0.05 V to 1.41 V λ = 10 Hz 0.5 hours	Sine wave V_{pp} = 1.41 V λ = 10 Hz 2 hours	N/A	2 mg ml^{-1}	15 μl droplet

Table 2.7 Protocols for Figure 2.4.

Figure 2.4 Average vesicle size and suspension standard deviation from electroformations conducted with and without ramping and detachment protocols.

Protocol	Ramp?	Mean vesicle diameter (μm)	Standard deviation (μm)	PDI
6	Yes	25.3	12.4	1.24
	No	16.7	8.4	1.26
7	Yes	24.9	10.3	1.17
	No	22.4	15.4	1.47

Table 2.8 Values for electroformation results in Figure 2.4.

Figure 2.5 Average vesicle size and suspension standard deviation for three different electroformation protocols performed on different days.

Protocol	Total lipid concentration	Deposition method	Ramp	Applied field	Detachment
8	2 mg ml^{-1}	Spincoat 175 µl	N/A	Sine wave V_{pp} = 3.39 V λ = 100 Hz 1.5 hours	N/A
9	2 mg ml^{-1}	Droplet 15 µl	Sine wave V_{pp} = 0.05 V to 1.41 V λ = 10 Hz 0.5 hours	Sine wave V_{pp} = 1.41 V λ = 10 Hz 2 hours	Square wave V_{pp} = 2.12 V λ = 4.5 Hz 0.5 hours
10	2 mg ml^{-1}	Droplet 10 µl	N/A	Sine wave V_{pp} = 3.39 V λ = 100 Hz 1.5 hours	N/A

Table 2.9 Protocols for Figure 2.5.

Protocol	Day	Mean vesicle diameter (µm)	Standard deviation (µm)	PDI
8	1	31.6	15.4	1.24
	2	16.2	5.5	1.11
9	1	19.3	10.0	1.27
	2	25.3	12.4	1.24
10	1	17.5	9.3	1.28
	2	11.7	5.7	1.24

Table 2.10 Data for electroformation results in Figure 2.5.

2.4   Conclusions

The electroformation process is still useful despite the inability to precisely control the vesicles' sizes. It produces consistently unilamellar vesicles which can be very difficult to obtain using other methods. It is shown here that controlling the resulting suspension through changing the total lipid concentration, how the lipids are applied to the electrode, or by adjusting the applied electric field parameters is unlikely. Monodisperse vesicles, with an ability to control the size, are desired for other studies that involve vesicle applications. While electroformation may not be the best method to obtain a monodisperse suspension, it offers a starting point to obtain GUVs that may be sorted by size for later use, as discussed in Chapter 3. A more in-depth description of the final electroformation protocol used for later vesicle experiments can be found in Appendix A.

# Chapter 3. Using microfluidics to separate vesicles by size

3.1   Introduction

Many diagnostic applications depend on the ability to separate suspensions of cells into components of interest. Microfluidic devices provide ways to conduct these separations without requiring the extra step of cell labeling, which could change the cell's properties. Microfluidics also offers a low cost approach by requiring minimal sample amounts and easily accessible equipment[65–67]. Most separation devices are tested on rigid spherical particles or with suspensions of red blood cells (RBCs); however, devices showing good separation results with rigid particles do not necessarily yield the same performance when using a suspension of deformable particles[68,69]. Testing separation devices with suspensions of vesicles allows for the effect of deformability to be included, while also providing the ability to investigate a broader range of particle sizes than those that are available from testing a suspension of cells.

Besides the advantages of using vesicles to test the separation devices, vesicle suspensions have intrinsic value for study after the separation process. Vesicles serve as a simple model for cells as they exhibit behavior similar to RBCs in channel flow conditions[4,70], and they have potential as drug delivery vehicles[71]. The thin lipid membrane of vesicles is characterized by a resistance to bending, but, unlike the membrane of RBCs, is fluid and offers negligible resistance to shear. Experiments have been conducted on single vesicles in simple Poiseuille flow in an attempt to understand the physics behind vesicle migration lateral to the flow direction[10]; extensive computational investigations into what controls the flow behavior of vesicle suspensions have also been conducted[12,72–79]. Theory and computational studies have so far only considered either monodisperse or bidisperse suspensions, leading to a need for vesicle suspensions with reduced polydispersity – such as those that have undergone size separation – if experiments to study the collective migration behavior of vesicle suspensions are to be performed and compared to theory and simulation.

Experimental studies of suspension flow behavior of vesicles require, ideally, the ability to generate suspensions of monodisperse, deformable particles; however, generation of monodisperse giant unilamellar vesicles can be very difficult. Microfluidic methods[80] that have been tried include utilizing water-oil-water emulsions[51,81], but this process is very sensitive to initial startup conditions and tailoring the hydrophobicity/hydrophilicity of channel walls and has not yet been optimized for consistent generation of vesicles. Electroformation[82] is a technique that produces many unilamellar (rather than multilamellar) vesicles, but the suspension produced is usually very polydisperse with a wide range of vesicle sizes (Figure 3.1). Other methods[49,83] that generate vesicles include gentle hydration, extrusion, and sonication, but these methods produce predominantly multilamellar vesicles or vesicles that are less than 1 micron in diameter, much smaller than the size range of interest, around 10-20 microns, which is of the same order as cells.
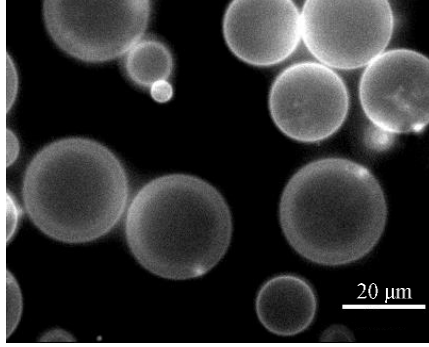
Figure 3.1 Polydisperse vesicles produced via electroformation

An alternative to microfluidic generation of monodisperse vesicles is to make polydisperse suspensions followed by size-based separation to produce suspensions with limited polydispersity. Label-free separation methods are attractive due to their ability to preserve the original vesicle (or cell) properties. These include filtration via obstacles (by weirs, pillars, cross-flows, or membranes), hydrodynamic filtration and pinched flow fractionation, deterministic lateral displacement, and inertial focusing, among others[67]. Here, we consider two separation schemes from this group: a cross-flow filter (that utilizes a size exclusion mechanism) and an inertial focusing separator. The filter was chosen because this design has shown promising results for use with vesicles[84]; however, the extent to which this device reduced the suspension polydispersity was unclear. The inertial device[68] was chosen because of positive results on suspensions of rigid spheres and its potential for adjusting the focusing size cutoff through changing only the device depth. The chosen designs have the potential to be implemented in a cascade for improved separation, and both device footprints are small, lending themselves to parallelization for higher throughput. These two separation schemes are easy to implement, as they do not require extra equipment to generate external fields (e.g. magnetic, acoustic, optical, etc.), which other label-free methods might employ. An additional advantage is the potential for extended runtime and continuous separation.

Below, we discuss the two separation mechanisms in detail and describe the different microfluidic devices that were used in this investigation. Metrics to evaluate the separation ability are also defined. Devices were fabricated and tested with a suspension of rigid spheres as well as polydisperse suspensions of vesicles produced via electroformation. A discussion of the efficacy of the two approaches follows.

3.1.1 Separation metrics

A variety of measures are reported in the literature to evaluate separation devices. The metrics used depend heavily on the suspension that is being separated as well as the target component. Gossett et al. summarized the metrics for separation devices that sorted cells as follows: throughput, recovery, separation resolution, enrichment, and purity or efficiency[67]. Definitions of these metrics can vary between different groups of researchers, but the most commonly reported values are some form of throughput, enrichment, separation efficiency, and purity. Throughput (T) can be reported in terms of volumetric flow rate, often multiplied by a volume fraction or cell density to include the effects of dilution.

$$T = \frac{volume}{time} \; [=] \frac{\mu L}{min}$$

21

For the following separation metrics, it should be noted that recovered suspensions (after separation) from a fraction of the device outlets are recombined before analysis; this is done to maximize the recovery volume as well as evaluate the device's ability to separate the initial suspension into two groups: a large vesicle suspension and a small vesicle suspension. These recombined suspension outlet streams are denoted with the subscript *chosen fraction*; they may consist either of the fraction that contains more of the large vesicles or the fraction that contains more of the smaller vesicles.

Enrichment (E) entails dividing the ratio of the target particle count (N_{target}) to contaminant particle count ($N_{contaminant}$) in a specific fraction of outlets by the ratio of the target count to contaminant count at the inlet:

$$E = \frac{\left[N_{target} : N_{contaminant}\right]_{chosen\ fraction}}{\left[N_{target} : N_{contaminant}\right]_{inlet}}$$

Separation efficiency (SE) can be defined as the number of target particles in a separated fraction divided by the total number of target particles recovered:

$$SE = \frac{\left[N_{target}\right]_{chosen\ fraction}}{\left[N_{target}\right]_{all\ fractions}}$$

Here, purity (P) is defined as the number of target particles in a chosen fraction divided by the total number of particles (both target and contaminants) recovered from that fraction.

$$P = \frac{\left[N_{target}\right]_{chosen\ fraction}}{\left[N_{target} + N_{contaminant}\right]_{chosen\ fraction}}$$

These separation metrics, in one form or another, have typically been used by groups that tested their devices on suspensions with clearly differentiated components (e.g., suspensions of rigid spherical particles of well-separated sizes[85–87], suspensions of blood containing platelets, RBCs, and white blood cells[88–91], bacteria[37], tumor cells[92,93], etc.)[69,94].

Many suspensions, however, are composed of particles that are not as easily segregated into categories but are instead characterized by a continuous distribution of sizes. These suspensions include emulsion droplets, vesicles, and some cell populations with a highly polydisperse distribution of sizes for a single component. Because these suspensions consist of one component, the target population is identified using a size cutoff[68,84,95], where the target population is either above or below this cutoff and the contaminant population consists of the remaining sizes. The size cutoff value depends on the end application for the suspension of interest and can be attained by adjusting different design or runtime parameters of the separation device. Establishing a size cutoff allows for the previously defined separation metrics to be calculated for vesicle suspensions and provides a way to compare the separation of vesicles to the separation of rigid spheres or cell suspensions.

The polydispersity index (PDI) is commonly used in describing the breadth of the molecular weight distribution in polymers for which the synthesis creates a broad, smooth distribution of molecular weights. The size (i.e., diameter) histograms produced through vesicle analysis provide analogous data which can also be characterized by a mean vesicle diameter μ and a PDI[96,97]. The PDI is simply related to the mean and standard deviation σ of the distribution by:

$$PDI = 1 + \left(\frac{\sigma}{\mu}\right)^2$$

Note that $PDI = 1$ corresponds to a monodisperse population, where all particles are of identical size; larger values of the PDI correspond to broader distributions. The mean and PDI are related to the first and second moments of the distribution, and provide meaningful separation metrics as long as the distributions remain close to normal distributions. However, for highly asymmetric or skewed distributions (such as the bidisperse suspensions of spheres considered below) these metrics are less useful. For our vesicle suspensions, the means and PDIs for the different devices averaged over several experiments are reported in Appendix C. In addition to this information, the difference between the mean diameter μ_L of vesicles in the collected suspension fraction that contains more particles that are larger than the cutoff size (this separated suspension fraction is denoted as S_L) and the mean diameter μ_S of particles in the collected suspension fraction that contains predominantly particles below the cutoff size (known as S_S) is reported as $\Delta\mu = \mu_L - \mu_S$. The difference in polydispersity index (ΔPDI) between the PDI of the initial suspension (S_I) and the PDI of the large particle fraction S_L is also reported.

3.2 Materials and methods

3.2.1 Separation mechanisms and device design

Two separation mechanisms are investigated: filtration via a size exclusion mechanism and inertial focusing. The size exclusion filter was adapted from Woo et al.[84] (Figure 3.2); it utilizes 19 filter channels that are 10 μm wide to remove vesicles below this size from the rest of the suspension. A pinching flow, introduced at the start of the filter section, along with wide outlet channels downstream of the filter (200 μm or larger), facilitate flow of the suspension through the filter channels. The volumetric flow rate of the pinching flow was kept at one third that of the suspension volumetric flow rate; the total flow rate through the device was 667 μL/hr, chosen after consideration of the work done by Woo et al.[84]. The smaller filter channels offer more resistance to or exclude the larger vesicles, while allowing the smaller vesicles to flow through. Outlets placed downstream of the filter section collect a suspension of mostly small vesicles, while outlets along the main channel collect fluid that bypasses the filter and collect mostly large vesicles. The height of the device was either 30 μm or 60 μm for the vesicle experiments and was 50 μm for the sphere experiments to mitigate clogging of the filter channels. 30 μm was chosen as a minimum height since the vesicle size of interest was around 10-20 μm. A bifurcation is introduced in the main channel after the filter section to skim off the excess sucrose introduced by the pinching flow. Three different bifurcation designs were used. These are illustrated schematically in Figure 3.3. One has the large vesicles pulled off the main channel first (Figure 3.3a), another has the skimmed sucrose pulled off of the main channel first (Figure 3.3b), and the third design has the bifurcation as a Y-shape, where the vesicles and excess sucrose diverge from the main channel at the same location (Figure 3.3c).
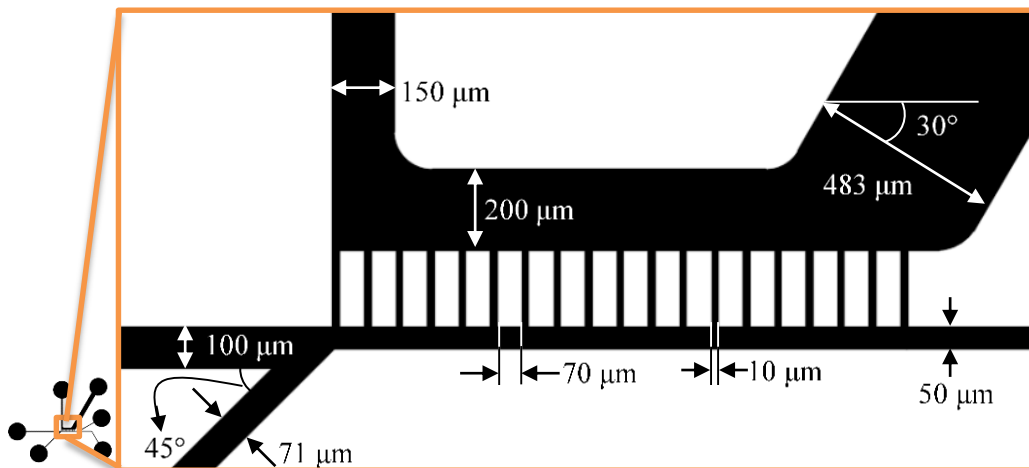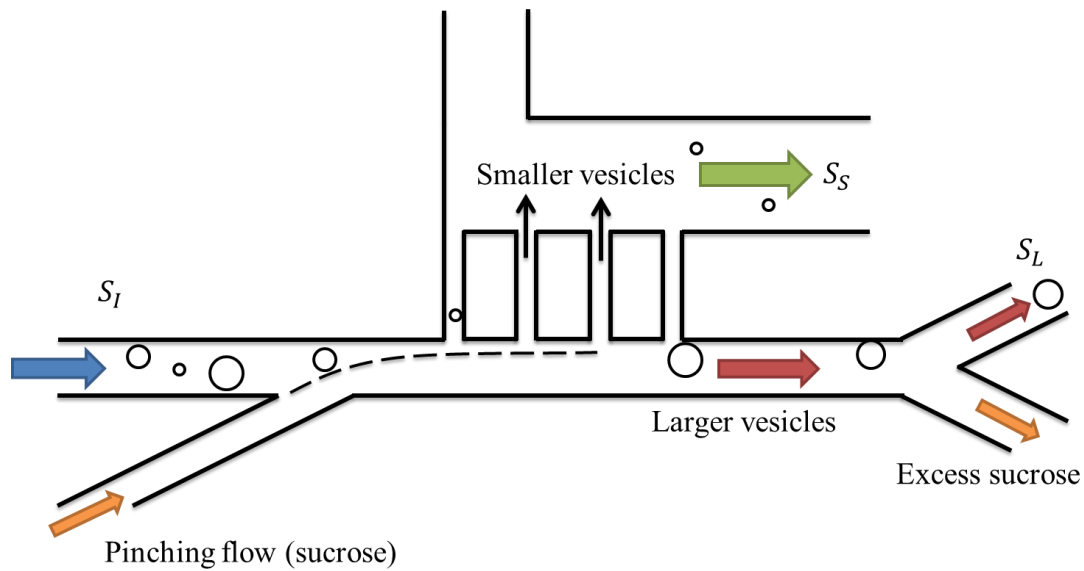
Figure 3.2 Schematic of filter design. (top) size exclusion mechanism. (bottom) design parameters.
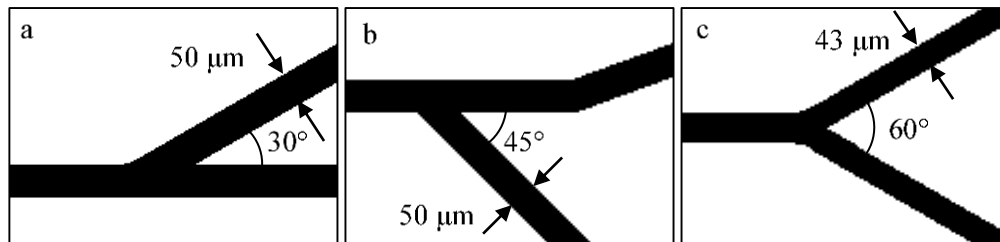
Figure 3.3 (a) Filter1 bifurcation design. (b) Filter2 bifurcation. (c) Filter3 bifurcation.

The inertial separator is based on a design proposed and discussed by Di Carlo et al.[68] (Figure 3.4). The inertial separator is run at higher flow rates so that fluid inertia affects the particle behavior. The inertial flow regime falls in a Reynolds (Re) number range of 10-500. Re is defined here as

$$Re = \frac{\rho_f \langle v \rangle D_h}{\mu_f}$$

where ρ_f is the fluid density, μ_f is the fluid viscosity, D_h is the hydraulic diameter of the channel, and $\langle v \rangle$ is the average flow velocity in the channel. Inertial lift forces and Dean drag forces introduced by the curving channels compete; both of these hydrodynamic forces depend on particle size. If the particle diameter is above a certain size cutoff, the inertial lift forces dominate and the particles will focus to a narrow band of streamlines by the end of the channel. If the particles are small, Dean flow dominates and induces mixing in the channel as the direction of the drag changes with the curvature of the serpentine walls; thus, smaller particles remain unfocused by the end of the channel. The larger particles will leave via one or two of the multiple outlets and can be collected and used for other studies.

Deformability of vesicles introduces a lift force[98] in addition to the inertial lift and Dean drag that rigid particles experience in these channels. In general, the lift force due to deformability directs the particle towards the channel center[8], though an investigation by Hur et al.[39] reported observations of deformable droplets migrating to equilibrium positions that were closer than expected to the channel wall when the ratio of internal to external viscosity fell below a threshold value. While deformability may affect the final equilibrium positions of migrating particles, inertial focusing and Dean drag mixing are still observed in this system and others[68,99,100]. Thus, the focusing and separation behavior of vesicles in this device is expected to be similar to that of rigid spheres.

The device height for the inertial separator was modified to work with different suspensions of interest. Changing the height of the device allowed for different size cutoffs during the separation; a device height of 145 µm was chosen for the following vesicle and sphere experiments based on particle cutoff size calculations proposed by Di Carlo et al.[68]. The empirical relation for hydraulic diameter (D_h) and cut-off diameter (a_c) is described by Di Carlo as:

$$D_{h2} = D_{h1} \left(\frac{a_{c2}}{a_{c1}} \right)^{\frac{3}{4}}$$

where a_{c1} and D_{h1} are the cutoff diameter and the hydraulic diameter, respectively, found in the results of Di Carlo's work (at Re = 115, a_{c1} = 4 µm and D_{h1} = 90 µm), and D_{h2} and a_{c2} are the hydraulic diameter and particle cutoff size for a new device and can be used to predict the proper device dimensions for a desired cutoff diameter. Due to interest in obtaining two suspensions of large unilamellar vesicles with average diameters of either 10 µm (as a model for red blood cell suspensions) or 20 µm (as a rough approximation for leukocytes or other cells), a cutoff size between 10 and 20 µm is desired. These devices were prepared with the dry film photoresist protocol (described below) that utilizes photoresist film of predefined thickness. A channel height of 145 µm is accessible, and an inertial separation device with these dimensions has an expected size cutoff of 13 µm, which falls between 10 and 20 µm as desired.
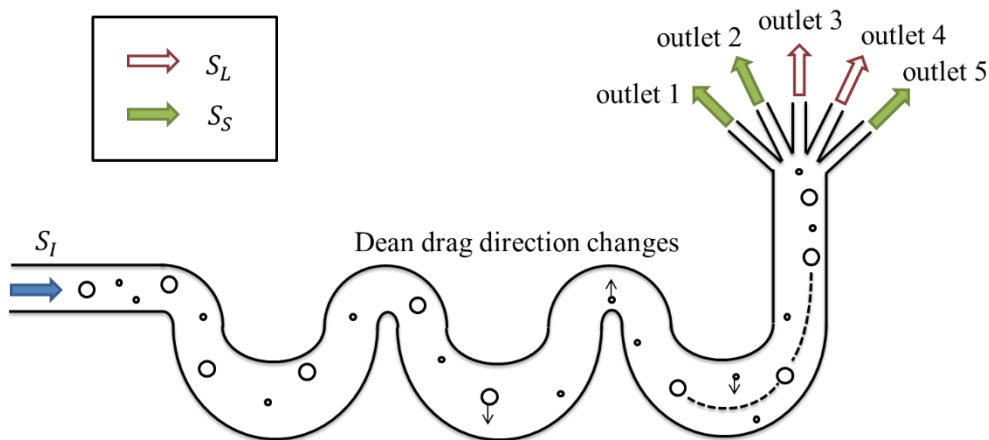
Figure 3.4 Schematic of inertial separator design.

3.2.2 Microfabrication

Microfluidic devices were fabricated using standard soft lithography techniques. Designs were drawn using AutoCAD (Autodesk), and masks were printed on mylar by Fine Line Imaging (Colorado Springs, CO). Device masters were fabricated with either SU-8 2050 photoresist from MicroChem on silicon wafers (see Appendix D for a detailed protocol) or by using a dry film photoresist (Riston GoldMaster GM130 photoresist, DuPont) that was laminated in multiple layers onto stainless steel wafers (see Appendix E for protocol details). Following exposure, this dry film photoresist can be developed away with a 1% K_2CO_3 solution, a much quicker and more benign process relative to the SU-8 development. Development of the unexposed dry film photoresist must be performed meticulously, as high aspect ratio (AR) channels (channel height/channel width > 1) are prone to overdevelopment and subsequent delamination from the substrate. For the inertial device, development of channels resulting in an AR of about 4 was obtained. Additional details of the dry film photoresist process can be found in Khalkhal et al.[101].

The Sylgard® 184 Silicon Elastomer Kit (Dow Corning) was used to make polydimethylsiloxane (PDMS) devices from the fabricated masters. The elastomer base was thoroughly mixed with the elastomer curing agent in a 10:1 ratio. This mixture was left to degas under vacuum for 30 minutes to an hour at room temperature. The degassed PDMS was poured over the master mold and degassed for another 30 minutes to an hour under vacuum. After all air bubbles are removed, the PDMS is cured at 60°C for 4 hours. Inlet holes and outlet holes in the PDMS devices were punched with a 16G blunt tip needle (McMaster-Carr). PDMS devices were bonded to glass coverslips (Fisherbrand, cover glass #1) using a handheld laboratory corona treater (BD-20AC, Electro-Technic Products). See Appendix F for a more detailed protocol description. Syringes were threaded using a 23G needle (BRICO Products) and were connected to the devices with Tygon® tubing (ID 0.020" Saint-Gobain PPL Corp.).

3.2.3 Materials

Suspensions of rigid spheres consisted of 0.025% v/v total sphere concentration of fluorescent polystyrene spheres. 0.02% v/v were 15 μm in diameter (FluoSpheres® yellow-green, ex/em 505/515 nm, Life Technologies) and 0.005% v/v were 2 μm in diameter (Fluoro-Max™ green, Thermo Scientific). To prevent particle aggregation, suspensions also contained 1% v/v Tween-20 (Sigma-Aldrich). To ensure spheres were neutrally buoyant, the suspension was 7% NaCl by mass.

26

Vesicles were prepared via electroformation[82] from 2 mg mL^{-1} total lipid mixtures that are 20% (0.4 mg mL^{-1}) 1-oleoyl-2-{6-[(7-nitro-2-1,3-benzoxadiazol-4-yl)amino]hexanoyl}-sn-glycero-3-phosphocholine (NBD PC, ex/em 460/534 nm, Avanti Lipids) and 80% (1.6 mg mL^{-1}) 1,2-dioleoyl-sn-glycero-3-phosphocholine (DOPC, Avanti Lipids). Lipids were dissolved in a 95% chloroform, 5% acetonitrile solvent. 15 μL was deposited and spread onto indium tin oxide (ITO) coated glass slides (Delta Technologies, Limited) with a Hamilton gas-tight syringe. The solvents were then evaporated under vacuum for 30 minutes. A 1.6 mm rubber gasket trimmed to fit the ITO slide (leaving a small gap along one edge) was placed between two lipid-coated ITO slides. Copper tape is used to connect the ITO electrodes to a function generator (Agilent 33220A). This electroformation cell was held together using small binder clips; a small gap is left through which 100mM aqueous sucrose can be deposited. The gap was closed with a bit of polymer clay (Sculpey). The electroformation protocol utilized a 10 Hz sine wave that was linearly ramped from 0.05 V to 1.41 V over 30 minutes; a 10 Hz, 1.41 V sine wave was then applied for the next two hours. Finally, a square wave with 2.12 V amplitude and 4.5 Hz frequency was applied for 30 minutes[63]. Vesicles are sensitive to high shear and must be handled gently with 18G syringe needles and wide pipette tips.

Vesicle volume fractions in the starting suspensions were determined using phase contrast microscopy at the CNR Biological Imaging Facility at UC Berkeley (see Appendix G). Images of vesicles in a hemocytometer counting chamber (Bright-Line Phase, Hausser Scientific Co.) were taken using a Zeiss AxioImager M1 microscope with a 20x phase objective and a Qimaging Micropublisher camera. This apparatus included a Sutter Instruments Lambda LS Light Source.

Vesicle deformability is characterized by a capillary number (Ca). Capillary number is defined[102] as:

$$Ca = \frac{\mu_f \dot{\gamma} a^3}{\kappa}$$

where μ_f is the fluid viscosity, a is the vesicle radius, κ is the bending modulus, and $\dot{\gamma}$ is the characteristic shear rate in a rectangular channel, defined as $\langle v \rangle / D_h$. Dahl et al. measured the bending modulus for this system and found $\kappa = 6.2 \times 10^{-20} J$ [7]. The capillary numbers experienced by the vesicles in the separation devices range from 10^2 to 10^5. These large capillary numbers are due to the high flow rates, and consequently high shear rates in the microchannels. Extensional flows of vesicles at capillary numbers of order 10^2 to 10^3 were explored in Dahl et al.[7]; under these conditions the vesicles did not rupture as long as the initial vesicle shape was close to spherical. In the present work, our flows are shear dominated. We estimate the capillary numbers in the shear flow experiments on vesicles of Coupier et al.[10], where no vesicle rupture was reported, as being of order 10^3. However, we anticipate some vesicle loss through breakage at the highest flow rates and Ca in the present experiments.

3.2.4 *Separation experiments*

Separation experiments with both vesicles and spheres were conducted using fluorescence microscopy. A Leica DMIRE2 inverted microscope was used with an external light source (Leica EL6000). A dual-band excitation/emission filter (Chroma 51004v2, 460-500/510-560 nm) was appropriate for our system. Objectives used include 10x (Olympus), 20x (Leica), and water-immersion 63x (Leica). Images and videos were taken by a monochromatic

Photometrics Cascade 512b CCD camera. Analysis was performed with ImageJ (NIH) and Matlab (Mathworks).

To prepare separation devices for experiments, 50% isopropyl alcohol (IPA) solutions, filtered using 0.2-0.4 μm filters, were injected to facilitate the removal of air bubbles from the device. For the sphere experiments, sphere solutions were introduced at this point and kept running until the IPA solution was flushed from the system before recording data. For experiments with vesicles, filtered de-ionized water was flowed through to remove the IPA solution. Next, a solution of filtered 2 mg mL^{-1} Bovine Serum Albumin (Thermo Scientific Pierce) was injected and left to sit in the device for at least five minutes. Filtered 100 mM sucrose was then flowed through the device to wash away the BSA solution. Finally, the vesicle suspension was introduced. Flow in all experiments was controlled with a syringe pump (Harvard Apparatus PHD 2000). See Appendix H for additional details on device preparation.

3.3   Results
3.3.1   *Device notation*

Several devices were used to test the separation mechanisms and strategies for vesicles. The individual designs are outlined in Table 3.1. Devices are named according to the separation mechanism (Filter or Inertial) and the device height in microns (e.g., H30 denotes a device that is 30 microns deep). For the filter devices, three exit configurations were tested, these are indicated by a number (e.g., Filter1) and the corresponding exit configuration is shown schematically in Figure 3.3 and in column 4 of Table 3.1. The different exit bifurcations were tested in filter devices that were 30 μm in height. 60 μm high filter devices were tested later to examine the design's ability to handle increased throughput. For the inertial separation device, only one height of 145 μm was tested; this height was studied based on considerations of the optimal hydraulic diameter needed to effect separation of vesicles that were 15 microns or larger.

3.3.2   *Consistency of initial vesicle suspensions*

Many electroformation cycles were performed to generate enough vesicles for all of the experiments. The mean vesicle diameter of the starting suspension was 17.6 ± 2.1 μm. The mean of the initial suspension's polydispersity index (PDI) was 1.29 ± 0.05. Measurements of the volume fraction of vesicle suspensions can be difficult to obtain. Standard quantification techniques (e.g., flow cytometry) use flow rates and focusing solutions that can lead to vesicle breakup; in addition, a lack of reference solutions for vesicles (used for instrument calibration) contributes to this difficulty in interpreting data for vesicles from cytometry and other methods. Therefore, volume fraction measurements were attempted with a hemocytometer. As a first validation of this technique, a suspension of 10 and 20 μm diameter rigid spheres was analyzed. The measured volume fractions ranged from 0.035% v/v to 0.048% v/v when the expected volume fraction was 0.025% v/v. For vesicles, a much broader variation was observed in the volume fraction measurements of three suspensions from 15% v/v to 47% v/v. A significant fraction of this variation can be attributed to concentration gradients that develop due to sample evaporation. Very small volumes (10 μL) are used in the hemocytometer, and the settling time required for the vesicles to sink to the plane with the counting grid is of the same order as the time for the effects of evaporation to become noticeable. We acknowledge this as a limitation of this quantification method, but note that efforts to better quantify the volume fraction for vesicles are beyond the scope of the current study.

Name	Separation mechanism	Device height (μm)	Bifurcation design
Filter1 H30	Size exclusion	30	
Filter2 H30	Size exclusion	30	
Filter3 H30	Size exclusion	30	
Filter1 H50	Size exclusion	50	
Filter1 H60	Size exclusion	60	
Inertial H145	Inertial focusing	145	Not applicable

Table 3.1 Device notation

3.3.3 Separation metrics

As noted above, sphere experiments used a bidisperse suspension of 2 and 15 μm diameter particles. To calculate the enrichment, separation efficiency, and purity for the experiments using this suspension, the target particles were the 15 μm spheres, and the contaminant particles were the 2 μm spheres. Vesicle experiments utilize a size cutoff to differentiate between target and contaminant particles. A size cutoff of 14 μm was established in order to compare the separation abilities of the filter and the inertial devices. This particular value is the average of the means of S_L and S_S for the two different devices. Note that S_L is the collected suspension fraction that contains most of the large vesicles and S_S is the collected suspension fraction that contains primarily small vesicles. Determining the distribution of vesicle diameters in S_L and S_S for all separation devices allows for comparison of separation ability and quality. Because applications for both S_L and S_S exist, the enrichment, separation efficiency, and purity are calculated for each separated vesicle suspension obtained from all separation devices. Metrics calculated for S_L are denoted by the subscript L; with these calculations, the target particles are vesicles with diameters above the size cutoff. Metrics for S_S use the subscript S, and target particles consist of vesicles with diameters below the size cutoff.

For the filter separation devices, S_L is the suspension collected from the outlet that bypasses the filter. S_S is the suspension collected downstream of the filter section containing mostly small vesicles. The filter schematic (Figure 3.2) illustrates which outlets correspond to each fraction. For the inertial separation device, the suspensions collected from outlets 3 and 4 were combined and used as S_L, while the suspensions collected from outlets 1, 2, and 5 were combined to form S_S (see Figure 3.4). Two outlets in the inertial device were used for S_L as the band of streamlines the rigid particles and vesicles focused to spanned more than one outlet channel.

In terms of the vesicle size cut off, the separation metric equations are listed below:

$$E_L = \frac{[N_{\geq 14} : N_{<14}]_{S_L}}{[N_{\geq 14} : N_{<14}]_{S_I}} \qquad SE_L = \frac{[N_{\geq 14}]_{S_L}}{[N_{\geq 14}]_{S_L} + [N_{\geq 14}]_{S_S}} \qquad P_L = \frac{[N_{\geq 14}]_{S_L}}{[N_{\geq 14}]_{S_L} + [N_{<14}]_{S_L}}$$

$$E_S = \frac{[N_{<14} : N_{\geq 14}]_{S_S}}{[N_{<14} : N_{\geq 14}]_{S_I}} \qquad SE_S = \frac{[N_{<14}]_{S_S}}{[N_{<14}]_{S_S} + [N_{<14}]_{S_L}} \qquad P_S = \frac{[N_{<14}]_{S_S}}{[N_{<14}]_{S_S} + [N_{\geq 14}]_{S_S}}$$
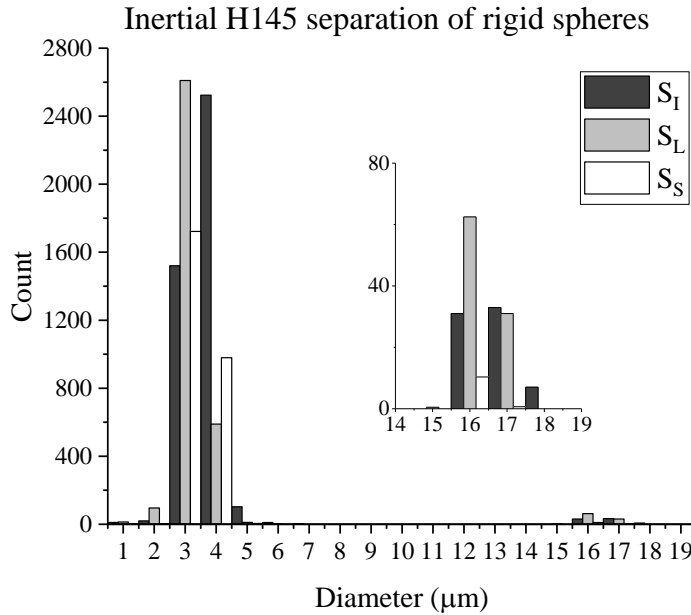
3.3.4 *Rigid sphere separation*

The separation results from the bidisperse suspension of 2 and 15 μm spheres in the 50 μm high filter device Filter1 H50 are shown in Figure 3.5. This and the following histograms compare the distributions of particle sizes in a suspension before and after separation; these histograms are generated by counting the number of differently sized particles in a fixed volume of the initial and separated suspensions (see Appendix I). These experiments were run at Re = 2.6, calculated with the hydraulic diameter D_h of the main channel that bypasses the filter section. Note that although the volume fraction of 15 μm spheres is much higher than that of the 2 μm spheres, the number fraction of the large spheres is much smaller. Thus, the portion of the initial suspension of spheres, S_I, that was included for size analysis has a large number of small spheres and about 60 total larger spheres (see inset). S_L consists of a number of larger spheres, but has lower numbers of both small and large spheres relative to the initial suspension. S_S has even fewer spheres, notably, there are almost no large spheres in this fraction. The overall loss of spheres in this device was expected due to 15 μm spheres being immediately trapped in the filter channels and causing blockage build up over the device run time. Images of the device, captured over the course of the experiment, show first large spheres being trapped in the filter channels; eventually, the small spheres are trapped throughout the device as well. Enrichment (E), separation efficiency (SE), and purity (P) for this device are reported in Table 3.2. There is some enrichment of the large spheres by the device as $E = 1.8$; this indicates that S_L has a number concentration of large spheres that is 1.8 times that of S_I. This device also showed good separation efficiency, as 97% of the total collected large spheres were collected in S_L. However, there was low purity (3%) of large spheres in S_L. This means a large quantity of small spheres remained in the main channel instead of passing through the filter. It is possible the 15 μm spheres blocking the filter channels contributed to the large number of small spheres in the large separated fraction, even though small spheres were still able to bypass these obstructions.
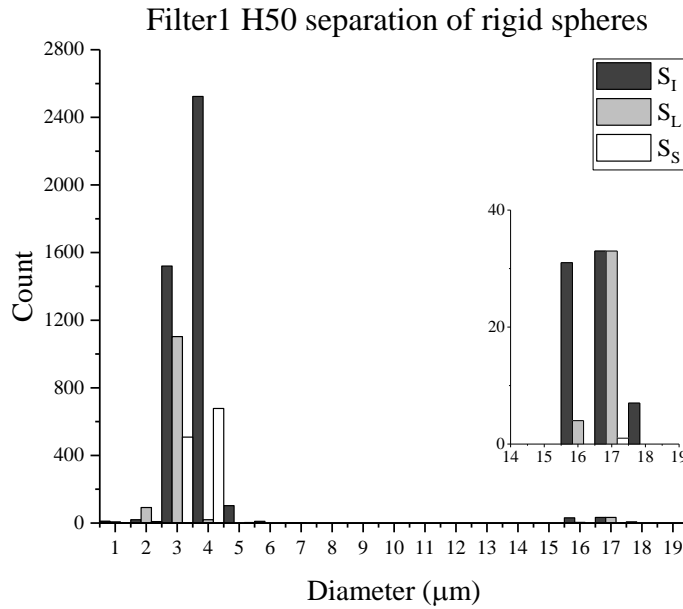
Figure 3.5 Filter1 H50 size distributions of initial and separated suspensions of 15 and 2 μm rigid spheres. (inset) sphere counts of 15 μm spheres.

The bidisperse suspension of spheres was also used with the 145 μm high inertial separation device; these results are shown in Figure 3.6. The inertial device was run at Re = 77, well within the flow regime that is influenced by the inertia of the fluid. (Note that this Re was calculated with the D_h of the repeating serpentine unit.) Again, while the volume fraction of large spheres is higher than that of the small spheres, the number fraction of large spheres is much smaller; changes in the numbers of large spheres are best examined in the inset of the figure. Clearly, the large spheres are more concentrated in S_L relative to S_I; indeed, since we are comparing fixed volumes from the inlets and outlets, the histogram reflects a larger total number of large spheres in S_L than in S_I . Similar to the filter results, S_S captured the lowest number of large spheres. Enrichment, separation efficiency, and purity are reported in Table 3.2. For this device, E is 1.7; this shows that the inertial device is similarly effective at concentrating the large spheres to a particular fraction as the filter device. The separation efficiency (SE) is high at 90%; that is, 90% of the collected large spheres are isolated to S_L. Despite the high separation efficiency, the purity (P) is low at only 3% of the total spheres collected from S_L actually being large spheres. For this device, a low purity is not unexpected. While the large spheres focus to a narrow streamline or band of streamlines, the smaller spheres remain equally distributed throughout the main channel, and thus all of the outlets should have a fairly large number of small spheres, as observed in Figure 3.6.

Figure 3.6 Inertial H145 size distributions of initial and separated suspensions of 15 and 2 μm spheres. (inset) sphere counts of 15 μm spheres.

| Device	E	SE	P	T (μL/min)
Filter1 H50	1.8	97%	3%	~8
Inertial H145	1.7	90%	3%	~550

Table 3.2 Comparison of sphere separation results. Note: Throughput T is calculated for undiluted sphere suspension.

3.3.5 *Vesicle separation*

Several different filter devices were tested with vesicle suspensions. The three bifurcation schemes were tested with the 30 μm high filtration devices at fairly low Reynolds number (Re = 4.3, Q = 667 μL/hr) to minimize vesicle breakup due to high shear in the device. The ability to run the device for long times depended heavily on controlling device clogging and the prevalence of vesicle break up in the filter channels. Several experiments were averaged to obtain the separation results histogram for Filter1 H30 in Figure 3.7. Good separation between the mean diameter of S_L and the mean of S_S was observed, as shown through a large $\Delta\mu$ (14 μm). S_L is clearly differentiated from S_I. At the same time, there is a noticeable decrease in the polydispersity of the separated suspensions, S_L and S_S, relative to S_I. A $\Delta PDI = 0.23$ between S_I and S_L represents a large polydispersity reduction. The separation histograms for Filter2 H30 and Filter3 H30 are shown as well (Figure 3.8 and Figure 3.9); these devices produced reasonable separation, but did not show as high $\Delta\mu$ or ΔPDI (see Table 3.3), which are indicators of separation ability. Interestingly, there was a noticeable difference in the separation results when the only physical difference between the three devices was the bifurcation in the main channel that is placed after the filter section. Possible explanations for this observation are discussed in the following section. The previously defined separation metrics, as calculated with a cutoff size of 14 μm, are reported in Table 3.4 for Filter1 H30. For this device, significant enrichment of the larger vesicles was observed in S_L ($E_L = 4.3$). The purity of the large vesicles was also high at 90%. The separation efficiency of the large vesicles was calculated to be 64%, implying a

32

significant portion of the available large vesicles were not captured in S_L. Still, this device shows promise in its ability to collect a majority of the large vesicles with high purity in S_L.

A filter device with deeper channels (so that the vesicles are less confined) was also tested with vesicles at moderate Re (Re = 43, Q = 6920 µL/hr); the resulting size histogram for Filter1 H60 is shown in Figure 3.10. These results are comparable to those for the Filter1 H30 device when looking at $\Delta\mu$ and ΔPDI, with $\Delta\mu$ = 13.9 µm and ΔPDI = 0.20 (see Table 3.3). These values indicate this device exhibits good separation ability and is able to reduce the polydispersity well. Because the vesicles were less confined, the throughput of the filter device could be increased with less clogging over equivalent run time. Table 3.4 displays the enrichment, separation efficiency, and purity results for this device. This device showed greater enrichment of the small vesicles relative to the 30 µm high filter device (E_S = 6.2 compared to 3.4) and reduced enrichment of the large vesicles (E_L = 2.9 versus 4.3). In separation efficiency and purity, the two filters produced similar results.
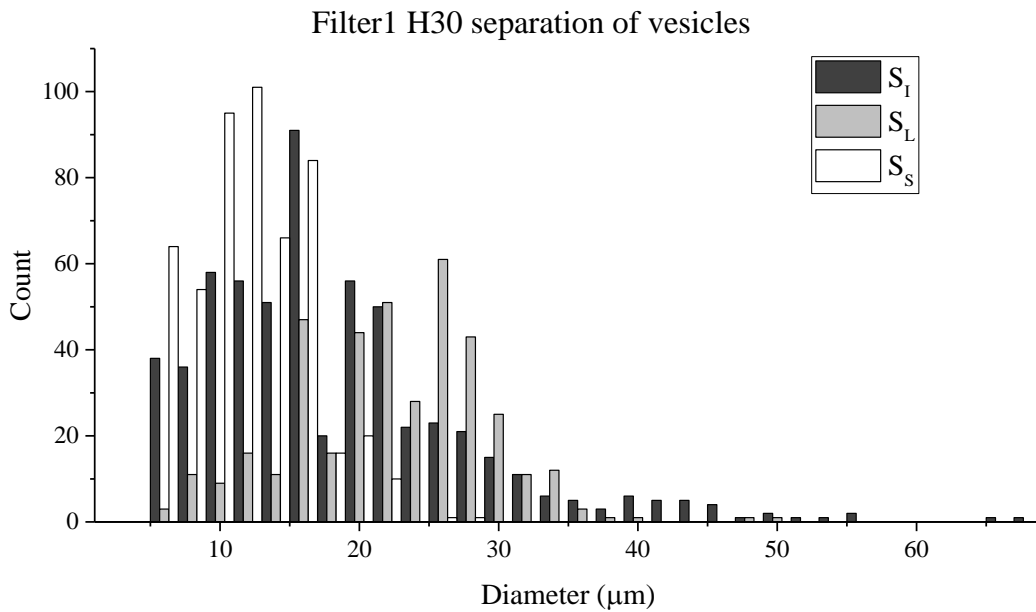
Figure 3.7 Filter1 H30 size distributions of initial and separated suspensions of vesicles.
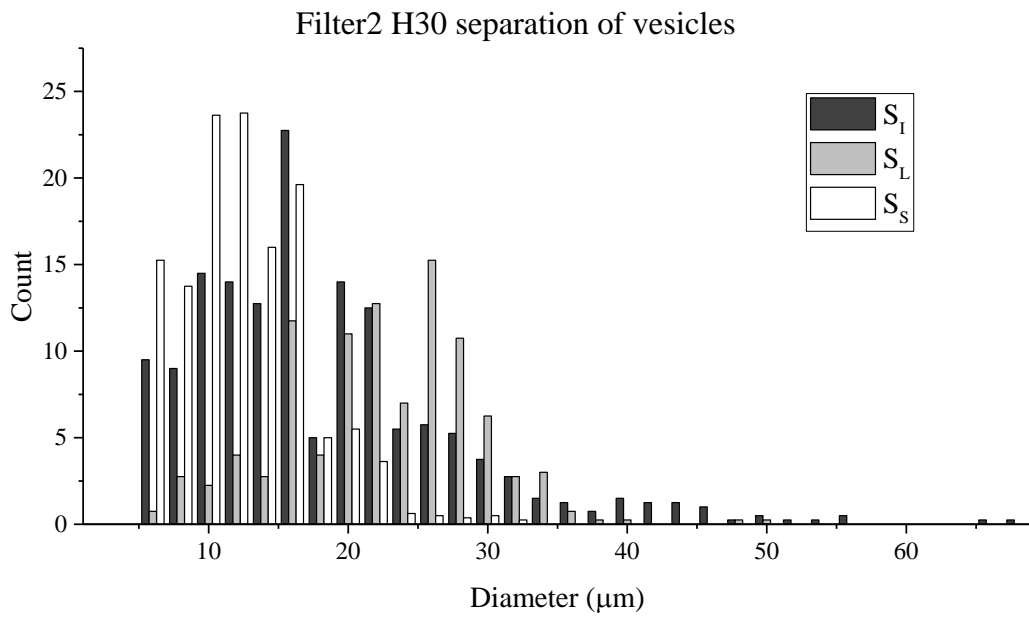
Figure 3.8 Filter2 H30 size distributions of initial and separated vesicle suspensions.
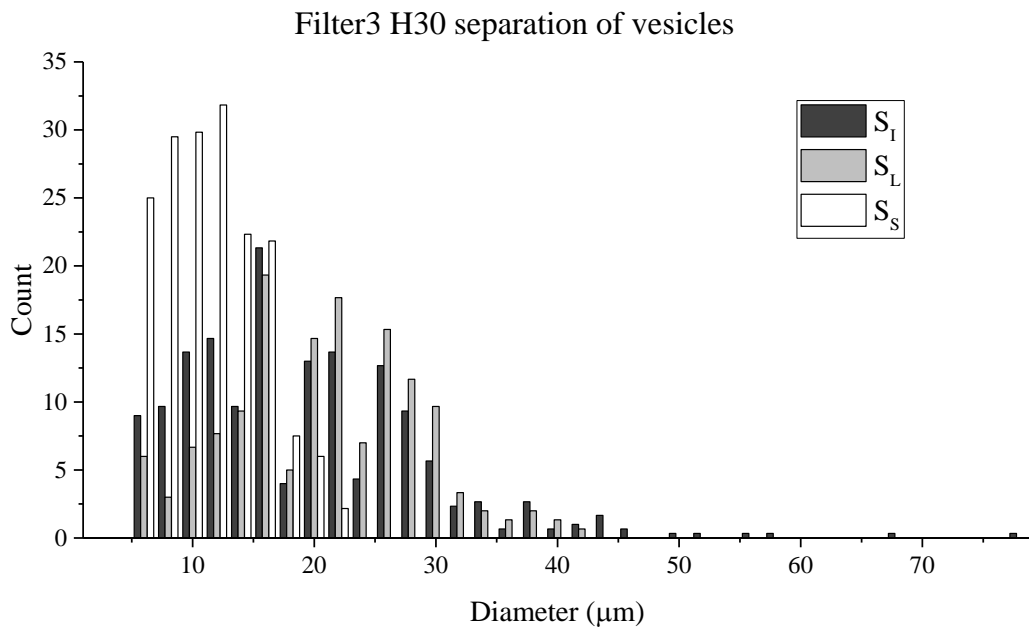
Figure 3.9 Filter3 H30 size distributions of initial and separated vesicle suspensions.

Figure 3.10 Filter1 H60 size distributions of initial and separated suspensions of vesicles.

After showing good separation ability with the suspension of rigid spheres, the inertial separation scheme was tested with vesicles at the same Re as used for the spheres, Re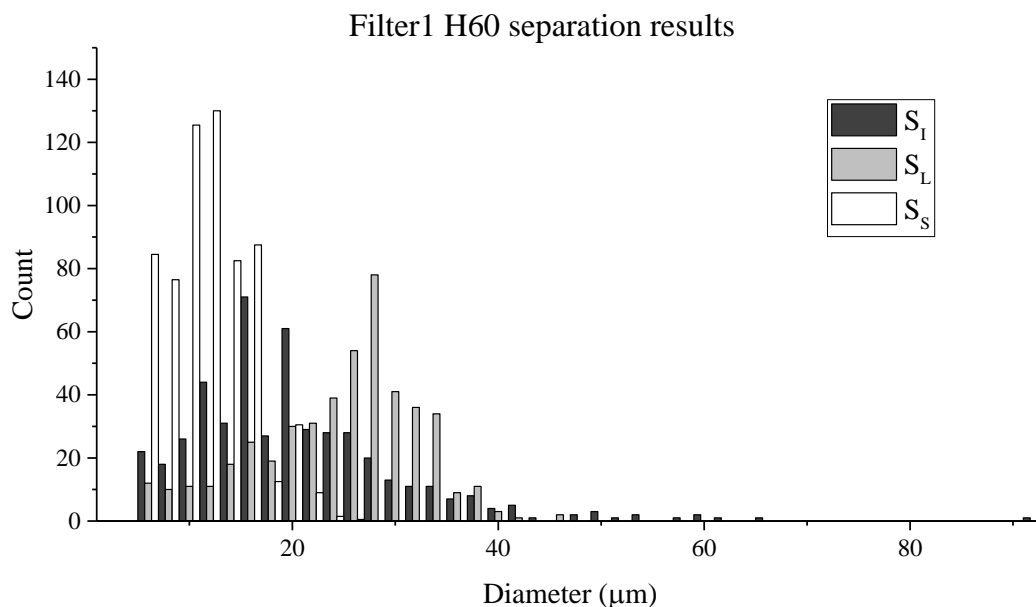 = 77 (Q = 33,000 µL/hr). It was observed that the degree of dilution affected the separation ability of the device, with the more dilute suspensions showing better inertial focusing and separation. Figure 3.11 shows how the vesicles focus to a narrower band of streamlines when the volume fraction (ϕ) is reduced from about 10% to about 2%. Different concentrations of vesicle suspensions were tested and the results for the most dilute suspension (1:15 dilution of the original electroformed suspension, corresponding to $\phi \approx 2\%$) are shown in Figure 3.12. This size distribution histogram shows a smaller separation between S_L and S_S relative to the filter devices, which is reflected in the $\Delta\mu$ of 5.8 µm (Table 3.3). The inertial device also generated a more modest ΔPDI of 0.11 suggesting its ability to reduce the polydispersity is limited relative to the filter device. Table 3.4 contains more separation metrics for the inertial device. The separation results for the more concentrated suspensions ($\phi \approx 6\%$ and $\phi \approx 10\%$), and a preliminary quantification of the dependence of the focusing on volume fraction, are reported in Appendix C. The PDI's of the less dilute separated suspensions were effectively unchanged relative to the initial suspension polydispersity, indicating that this separation device was more effective when the suspension concentration was dilute. Of note is the separation efficiency SE_L, which is reported to be 86%, the highest separation efficiency of the three devices. While this device was adept at collecting a significant majority of the large vesicles, the purity suffered somewhat, as P_L was shown to be 63%. In the case of the purity of the small vesicles (P_S) in the small separated fraction, the inertial device displayed the highest value at 82%.

Separation design	$\Delta\mu$ (µm)	ΔPDI	T (µL/min)
Filter1 H30	14.0	0.23	~10
Filter2 H30	9.7	0.17	~10
Filter3 H30	8.8	0.17	~10
Inertial H145	5.8	0.11	~37
Filter1 H60	13.9	0.20	~115

Table 3.3 Comparison of vesicle separation results with mean size difference ($\Delta\mu$) and polydispersity reduction (ΔPDI). Note: Throughput T is calculated for undiluted suspensions.
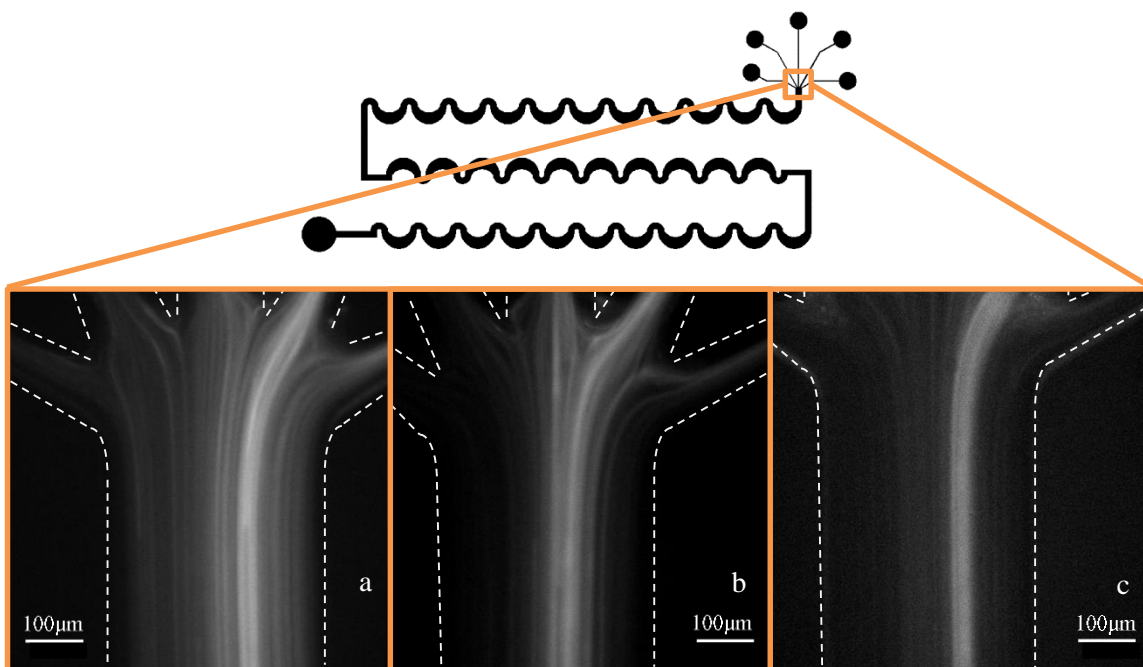
Figure 3.11 Dilution of vesicle suspension changes how well the suspension focuses. (a) Least focused suspension has volume fraction (ϕ) $\approx$ 10%; (b) $\phi \approx$ 6%; (c) best focusing behavior observed with $\phi \approx$ 2%.
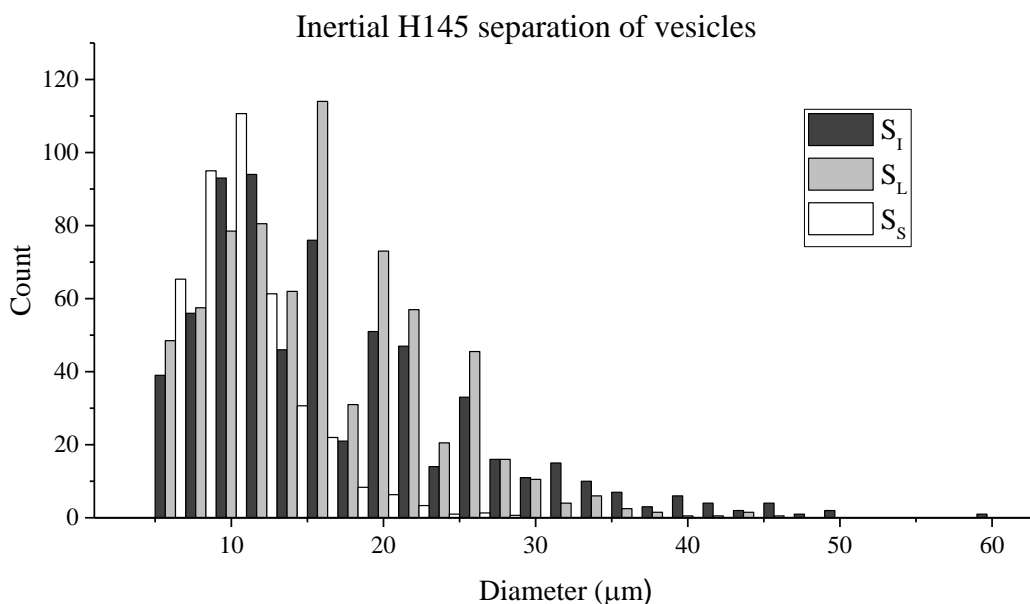
Figure 3.12 Inertial H145 size distributions of initial and separated suspensions of vesicles.

Device	Filter1 H30	Filter1 H60	Inertial
E_L	4.3	2.9	1.3
E_S	3.4	6.2	5.9
SE_L	64%	66%	86%
SE_S	89%	90%	56%
P_L	90%	91%	63%
P_S	61%	65%	82%

Table 3.4 Comparison of vesicle separation results in terms of enrichment, separation efficiency, and purity.

3.4   Discussion

3.4.1   *Rigid sphere suspensions as a first estimation of separation ability*

The inertial separator is an example of how using rigid spheres to optimize a separation device can be very useful. The device needed modifications for higher cutoff sizes, which were predicted through the empirical relationship of Di Carlo[68]. Optimal device height and focusing behavior can be confirmed by using suspensions of rigid particles before testing the device with more valuable suspensions of vesicles or cells. In this device, the clogging issues were nearly non-existent due to the large channel widths and heights.

When the filter devices were being tested with suspensions of rigid spherical particles, however, the filter channels became blocked by the larger spheres almost immediately. Persistent clogging of the device to this extent was not observed with vesicles in so short of a time window. The advantage to using rigid spheres as a first estimation for how a separation device will function is that these suspensions are easy to obtain; however, spheres may not always offer the

best representation of a device's separation ability, especially if the end application involves a suspension of deformable components. The deformability of the suspended particles appears to play a significant role in the filter device operation, and using rigid sphere suspensions does not provide an accurate validation of the separation capabilities of the filter device. This comparison also suggests that fundamentally different designs may be optimal for separating deformable particles and rigid particles, showing the value in testing devices with deformable suspensions.
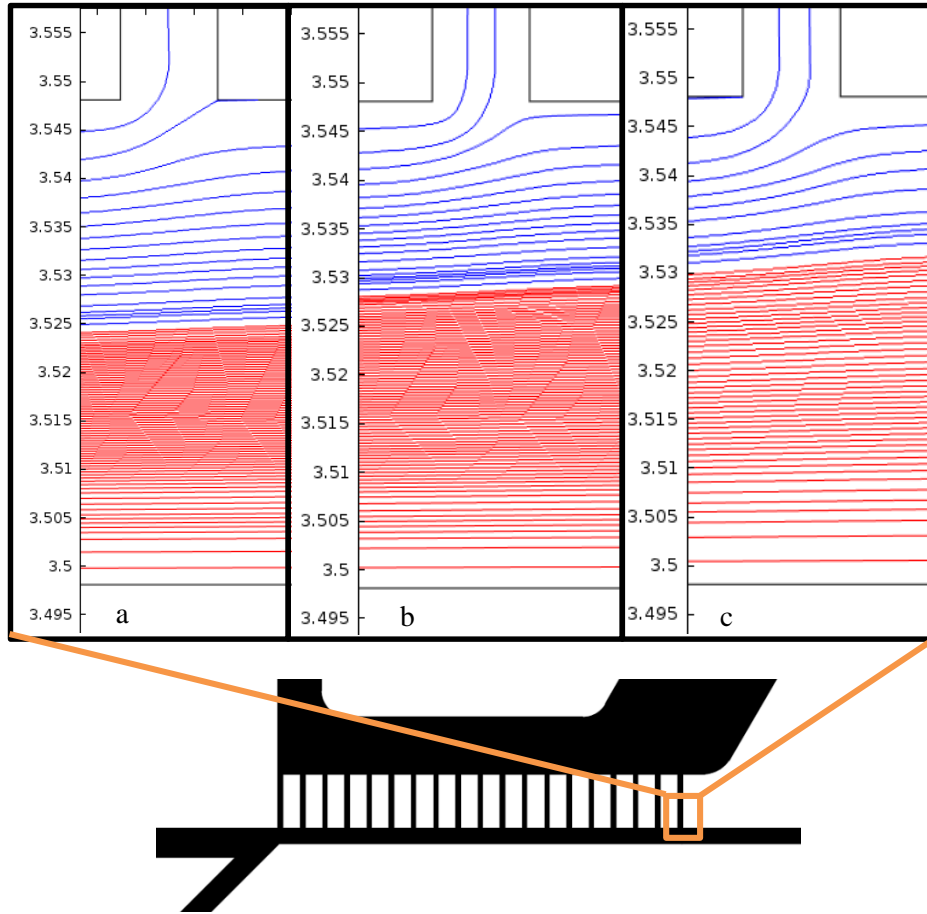
3.4.2 *Evaluation of filtration as a separation strategy for vesicles*

The filtration device showed good separation capability in the high $\Delta\mu$, ΔPDI, and purity values, though these came at the cost of low throughput and severe clogging issues. The 30 μm high devices in particular were especially prone to clogging from debris or lipid residue. While the reduced vesicle confinement of the 60 μm high device helped to mitigate the clogging issues, both the 30 μm and 60 μm high devices could be used only once. An advantage of these devices is that they were able to separate concentrated vesicle suspensions and required no dilution of the initial vesicle suspension. The 60 μm high filter devices allowed for increased throughput, while maintaining the separation and PDI reduction capability. The similar separation results for the two different device heights indicate that – as expected – the smallest dimension (here, the width of the filter channels) is what controls the size cutoff. Separation results for this device design also appear relatively insensitive to Reynolds number, at least over the range probed (4.3 < Re < 43).

The filtration device was adapted from work by Woo et al.[84] who reported a $P_L < 80\%$; the filter devices designed here obtained $P_L = 91\%$. Other separation metrics such as enrichment or separation efficiency were not reported in the earlier study.

3.4.3 *Channel resistance in filter devices affects separation ability*

Three different configurations of the bifurcation after the filter section were tested. There was a noticeable difference in the separation ability of the three designs, as several experimental replicates yielded different $\Delta\mu$ and ΔPDI values. To investigate the effect of bifurcation geometry on the flow, a 2D approximation of the channel flow in the different designs was simulated with COMSOL (see Figure 3.13), where the flow rates of the sample inlet and the pinching flow were constant across the device designs. These streamline plots show the distribution of streamlines in the main channel at the last filtration channel of the filter section. The red streamlines are from the pinching flow inlet introduced before the filter, and the blue streamlines are from the inlet where the vesicles are introduced. It is clear that more blue streamlines from the vesicle inlet remain in the main channel in the Filter1 design relative to the other two, indicating that more large vesicles were able to exit to form S_L in this design. Filter2 and Filter3 had slightly longer outlet channels, and thus, higher channel resistances, than the outlet channels in Filter1. This higher channel resistance was likely pushing a greater quantity of large vesicles through the filter sections of these two devices. Forcing more of the large vesicles through the filter leads to faster filter clogging, and higher numbers of large vesicles in S_S. As the filter clogs, more of the small vesicles will bypass the filter and end up in S_L. In both of these cases, the $\Delta\mu$ and ΔPDI will be reduced. These filter devices appear to be quite sensitive to the outlet channel resistance; optimizing the channel resistance may be one way to tune the separation ability.

Figure 3.13 COMSOL generated streamlines; blue represents vesicle inlet, red represents pinch flow inlet. (a) Filter1; (b) Filter2; (c) Filter3

3.4.4   Evaluation of inertial focusing as a separation strategy for vesicles

The inertial device showed higher SE_L and P_S than the filter devices. Depending on what suspension parameters are valued, this device shows promise. The greatest advantage of the inertial device was the reduced run time. This device also experienced minimal clogging, and when pieces of debris did enter the device, they were easy to remove. This quality allowed the devices to be reusable. While the H60 filter has the highest throughput rate after taking the dilution factor into account, the inertial device is still likely to have a shorter overall run time when including the time required to remove air and debris from the devices before introducing the vesicles. The inertial devices exhibited acceptable separation and modest PDI reduction with diluted vesicle suspensions, but worked best with dilute suspensions of rigid spherical particles. If the target particles are the smaller suspension components, and the larger contaminants are very dilute, this device offers an efficient way to filter out the contaminants from the targets after optimizing the cutoff size. However, the device is not optimal when the smaller component is the contaminant.

This device was modified from work presented by Di Carlo et al. who reported results for a polydisperse suspension of PDMS spheres as $E_L \approx 4$ and $E_S \approx 1$ [68]. The modified device

presented in this work had $E_L = 1.3$ and $E_S = 5.9$ when run with vesicles. Other separation metrics were not reported by the Di Carlo group.

3.4.5 *Inertial separation requires dilute suspensions*

When the suspended particles are being inertially focused to a narrow band of streamlines, if the vesicle suspension is too concentrated, the vesicles will interact and prevent focusing from occurring. To facilitate focusing in the inertial separator, vesicle suspensions were diluted significantly (1/15 of the initial concentration); this makes the throughput of the initial suspension more moderate, at about 40 µL/min. This volumetric flow rate is still higher than that used with the H30 filter devices, and the use of this device may be more appealing when the time required to prepare the inertial devices relative to the filter devices is taken into consideration, or when dilute vesicle suspensions are appropriate for post-separation use.

3.4.6 *Separation dependence on device height*

The separation ability of the filter device appears to depend solely on the width of the filter channels instead of the height. This may be used to greatly increase the throughput while maintaining the same size cutoff capability. This is in contrast to the inertial device, where changing the device height directly affects the size cutoff for particles that will be focused. This feature of the inertial separator allows a single mask design to be used for different separation applications. One mask can be used to fabricate masters with varying channel heights, each tailored to the desired size cutoff.

3.5 Conclusions

As interest in the development of microfluidic diagnostic tools grows, the separation of various components of deformable particle suspensions becomes increasingly important. Using vesicles to test the separation ability of these microfluidic devices provides valuable insight into how deformability affects the suspension behavior and can illuminate separation aspects that are inaccessible if using a suspension of rigid spheres to test the devices' separation abilities. Vesicles also serve as a model suspension for cell populations and offer a first order estimation of cell behavior in these devices.

The size exclusion filter exhibited good size separation, as well as an ability to significantly reduce the suspension polydispersity. These devices can obtain higher throughputs while maintaining similar separation capability by increasing the channel height. They can be used with undiluted initial suspensions, but are subject to device clogging issues which render the devices as single use.

The inertial focusing separator had reasonable size separation and modest polydispersity reduction abilities. It was relatively high throughput, though good separation required dilute suspensions. These devices had few to no clogging issues, allowing them to be reusable.

If the goal is high purity of a large target particle, the H60 Filter1 device appears to be the best device to use. If high separation efficiency of the large target particles is desired, the inertial separation device showed the most promising results. The performance of the filter device is affected by downstream bifurcations in the channel; this should be kept in mind when designing these devices. The inertial device better lends itself to continuous separation since there is a low incidence of clogging with these devices. These separation devices may be cascaded to increase the purity or separation efficiency and reduce polydispersity of the separated fractions. These

separated vesicles can be used in further experiments to better understand the flow behavior of vesicle suspensions and compare with simulations.

Chapter 4. Inertial migration of bidisperse sphere suspensions

4.1   Introduction

Inertial microfluidic devices make use of hydrodynamic forces present in channel flow conditions that cause initially randomly distributed particles in suspensions to migrate to specific equilibrium positions in the channel. Inertial microfluidics has been an integral design component of many lab-on-a-chip (LOC) devices and micro total analysis systems (μTAS), and has the potential to continue to make a large impact on these fields and the area of assay development through lowering material and time requirements, increasing portability and sensitivity, and reducing test costs[28,31,103]. Inertial microfluidics has many applications; it can enable control of single particles, separate leukocytes or circulating tumor cells from blood suspensions[104–106], collect blood plasma[107], enrich cell concentration in dilute suspensions[108], or detect pathogens and diagnose malaria[109]. Several commercial endeavors that utilize inertial microfluidic LOC devices are currently in operation[40,105,106,110].

Inertial migration occurs in the flow regime where inertia is no longer negligible, namely Re ~ 10-100. This phenomenon was first observed experimentally in the early 1960s by Segré and Silberberg[22], setting off a host of both experimental and theoretical investigations into its mechanism[111–117]. There are several forces acting on an individual particle in flow: viscous drag, diffusion, Magnus rotation, Saffman slip-shear, wall-induced lift, and shear gradient-induced lift. The forces that act lateral to the flow direction – and thus, could lead to the inertial migration phenomenon – are determined to be the Magnus force, Saffman force, wall lift force, and shear gradient force. The Magnus lift force occurs when a rigid sphere is rotating in a fluid; a pressure difference around the sphere develops due to the difference in streamline velocity on one side of the sphere in comparison to the velocity on the other side (where the rotation appears to be against the flow direction), and this pressure asymmetry can cause the sphere to migrate[118]. The Saffman lift force is derived from the difference in velocity between the particle and the suspending fluid. If the sphere is lagging behind the fluid, Saffman lift directs particles towards the region where the velocity is higher. If the sphere is actually faster than the flow, the Saffman force moves the particles closer to the walls, where additional drag can act to slow the particle's motion[27]. The wall-induced lift force works to direct particles away from the wall and arises from how the presence of the wall affects the flow around the particle[119]. The shear-induced lift force drives particles towards the channel walls due to pressure asymmetry the develops around the particle. This pressure variation is from the difference in relative velocity streamlines that the particle experiences in Poiseuille flow[28,120]. The current state of theory considers the Magnus and Saffman forces to be comparatively negligible, while the wall-induced lift force and the shear-induced lift force are termed the dominant contributors to the inertial lift that guides suspended particles to the channel equilibrium positions[28,40]. Figure 4.1 illustrates these forces.

Secondary flows or outside forces may also be implemented, offering additional control over the suspended particles. Spiral or serpentining channels introduce Dean flows and an extra force that works to reduce the number of stable equilibrium positions in the channel[41]. Outside applied fields[121,122], such as magnetic[94] or acoustic[123] fields, have been used with some inertial microfluidic systems in a similar capacity. Deformability and particle shape are other properties that may influence how the particles behave or where they migrate in the limit of inertial migration, but these parameters are not the focus of this investigation. The system studied here utilizes simple straight channels of unchanging cross-section and rigid particles, in an attempt to reduce the number of contributing forces that lead to the observed migration behavior.
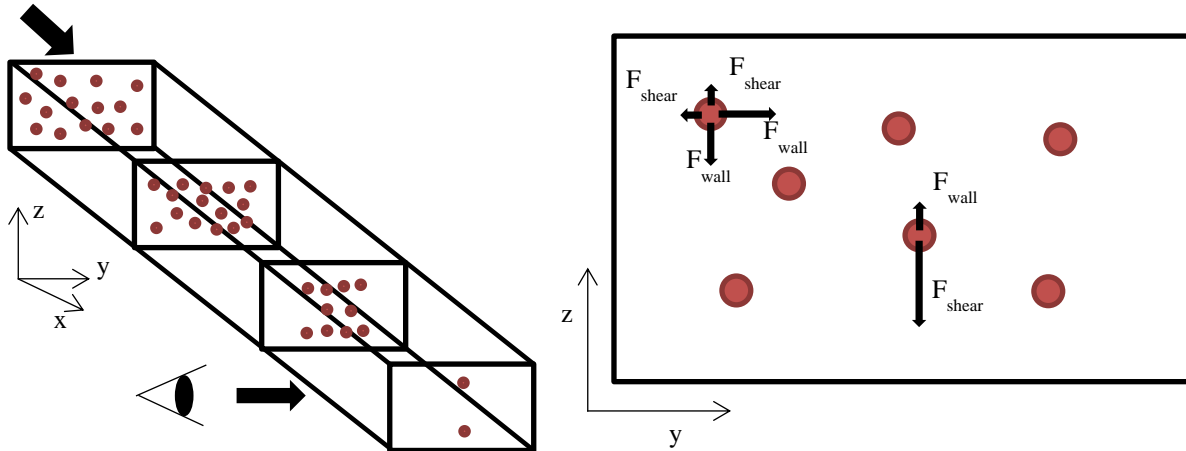
Figure 4.1 Inertial migration of particles to specific equilibrium positions in the channel due to shear-induced lift forces and wall-induced lift forces.

Attempts to predict the migration entry length involve a force balance of inertial lift and Stokes drag; however, small differences in these entry length equations, such as different definitions of the characteristic length or a factor of two, can lead to noticeable differences in the predictions. Table 4.1 presents some estimated entry lengths for our microfluidic system and the spheres used. U is the average velocity in the channel, μ is the suspending fluid viscosity, ρ is the fluid density, and a is the particle diameter.

Equation	Sphere size (μm)	Entry length (mm)	Notes	Reference
$L = \dfrac{3\pi\mu H^3}{\rho U a^3}$	5 10 15	67 8 2	Here, H is the hydraulic diameter: $\dfrac{2hw}{h+w}$, where h is the channel height and w is the channel width	28
$L = \dfrac{\pi\mu H^2}{\rho U_m a^2 f_L}$	5 10 15	14 3 2	Here, H is the smallest channel dimension, $U_m \sim 1.5U$, and $f_L = 0.05$.	31
$L = \dfrac{3\pi\mu}{2\rho U}\left(\dfrac{H}{a}\right)^3$	5 10 15	15 2 1	Here, H is narrowest channel dimension.	124
$L = \dfrac{3\pi\mu D_h^2}{4\rho U a^3}\left(\dfrac{W}{C_L^-}+\dfrac{H}{C_L^+}\right)$	5 10 15	488 26 2	Lift coefficients: $C_{L,5}^-= 1.6$, $C_{L,5}^+= 0.05$; $C_{L,10}^-= 1.2$, $C_{L,10}^+= 0.12$ $C_{L,15}^-= 0.6$, $C_{L,15}^+= 0.7$.	29

Table 4.1 Predicted entry lengths for a system with channel height = 93 μm, channel width = 50 μm, $\mu = 1.12 \times 10^{-3}$ kg s^{-1} m^{-1}, and $\rho = 1048$ kg m^{-3}.

Inertial migration has been studied extensively and put to use in a wide variety of devices and biomedical applications; however, the effect of polydispersity on the migration behavior is still an open question. This chapter attempts to address this question by studying suspensions of

monodisperse and bidisperse rigid spheres as they undergo inertial migration. As these microfluidic channels have a rectangular cross-section, it is expected that the rigid spheres will migrate to two distinct equilibrium positions in the channel. Figure 4.1 shows the direction the migration behavior is being observed from; this vantage point allows for both equilibrium positions to be visible as they develop. The entry lengths over which the particles approach their final equilibrium positions can be measured through these observations. Bidisperse suspensions are composed of spheres with two different diameters. The total volume fraction of the suspension is held constant, but the spheres are mixed in varying proportions of large to small spheres (e.g., if the majority of the volume fraction is composed of small diameter spheres, the large diameter spheres make up the corresponding minority fraction). The measured entry lengths of the spheres in this bidisperse system are compared to both the measured and the predicted entry lengths for a monodisperse suspension in the same microfluidic channel. Two different bidisperse systems are analyzed and discussed. Initially, it is expected that the addition of polydispersity into this system will increase the entry lengths for both sphere sizes as they migrate towards similar focusing positions; however, it is possible that the spheres may display cooperative behavior, or even remain unaffected by the presence of differently sized spheres due to the dilute nature of the suspension.

4.2   Materials and methods
4.2.1   Device fabrication
Microfluidic channels were fabricated with standard soft lithography techniques to be 93 µm high and 50 µm wide. The channel lengths ranged from 75mm to 82mm. The channel masks were designed using AutoCAD (Autodesk) and printed on mylar plastic (Fine Line Imaging, Colorado Springs, CO). Channel masters were fabricated using a dry film photoresist (Riston GoldMaster GM 130 photoresist, DuPont) that was 100 µm thick. This photoresist film was laminated onto 4-inch diameter stainless steel wafers (Stainless Supply). The mask was placed over the photoresist covered wafer and the apparatus was exposed to UV light for about 45 seconds. The unexposed photoresist is developed away with a 1% K_2CO_3 solution. Additional details of the dry film photoresist master protocol can be found in Appendix E.

The developed master is used as a mold for the channel devices. Polydimethylsiloxane (PDMS) devices are fabricated using the Sylgard® 184 Silicon Elastomer Kit (Dow Corning); the base is mixed with the curing agent in a 10:1 ratio and left to degas under vacuum for an hour at room temperature. Once all of the air bubbles are gone, the PDMS is poured over the channel mold and left to degas for another hour. After all of the air is removed, the PDMS is cured for at least 3 hours at 60°C. Typically, the first batch of PDMS does not bond well to the glass slides, so this is discarded and the above process is repeated. With the second, and subsequent, batches, the cured PDMS can be peeled off of the wafer master mold, cut to size, and bonded to glass slides. Because these channels are often longer than standard microscope slides, larger glass slides are cut from glass plates (6" × 4.5", Ted Pella, Inc.). Before bonding, inlet and outlet holes are punched in the PDMS with 16G blunt tipped needles (McMaster-Carr). A handheld laboratory corona treater (BD-20AC, Electro-Technic Products) is used to bond the PDMS channels to the glass slides (see Appendix F).

4.2.2   Sphere suspensions
Rigid sphere suspensions have a total volume fraction of 0.01% v/v and are composed of fluorescent, nearly monodisperse polystyrene spheres of either 5 µm (Fluoro-Max™ green,

ThermoScientific), 10 μm (FluoSpheres® orange ex/em 540/560, Life Technologies), or 15 μm (FluoSpheres® yellow-green ex/em 505/515, Life Technologies) in diameter. So that the suspending fluid is density matched with the sphere density, the suspensions are also 7% by mass NaCl. To prevent sphere aggregation, the mixtures are also 1%v/v Tween-20 (Sigma-Aldrich). Stock suspensions and bidisperse mixtures are sonicated for 10 minutes before use. See Appendix J for detailed sphere recipes.

4.2.3   Migration experiments

Devices are prepared by inserting Tygon® tubing (ID 0.020, Saint-Gobain PPL Corp.) in the outlet hole of the channel. A 3 ml syringe is filled with a 50% isopropyl alcohol (IPA) solution and threaded with a 0.2 μm filter and a 23G blunt tip needle (BRICO Products). The inlet tubing is fitted around the needle and flushed with filtered IPA before inserting into the channel inlet. The device is then flushed with the 50% IPA solution to remove all the air. Once the entire device and outlet tubing are filled with IPA, the sphere solutions (freshly sonicated) are introduced with a syringe pump (Harvard Apparatus PHD 2000). Videos of the spheres in the channel were taken with a 20x magnification objective (Leica) using a Phantom MIRO M310 camera and a Leica DMIRE2 inverted microscope. Spheres were fluorescently illuminated with an external light source (Leica EL6000).

When running spheres through the channels, it is important to maximize the contrast between the spheres and the background, especially because some of the spheres of interest can be quite dim (e.g. when the 15 μm spheres make up 25% of the suspension that is only 0.01%v/v spheres in the first place). Besides turning off the overhead lights in the room and opening up the lightsource shutter in full, it is important to hit the "Current Session Reference" (CSR) button on the camera software interface for every new experiment. Videos of at least 1200 frames at 24 frames per second are captured at different positions down the channel. Appendix K has more details of the microscopy process.

4.2.4   Image Analysis

Each video is initially analyzed using ImageJ (NIH). The average of the image stack (that comprises the video) is taken, then the intensity profile of that average image is measured (see Figure 4.2). In Excel (Microsoft), the intensity profile is graphed and a Gaussian curve is fitted to each main peak in the profile (with this particular channel geometry, there are two peaks that develop). The full width at half maximum (FWHM) of each Gaussian is calculated (see Figure 4.3 for a visual representation). This analysis is repeated for each video that was captured at different positions down the channel. Once all of the videos for a particular experiment are analyzed, the FWHMs are plotted against the distance down the channel at which the video was recorded (Figure 4.4). This information can be fitted with a decaying exponential function. The focusing length is determined as the length (in mm) at which the exponential fit falls within 5% of its asymptotic value. See Appendix L for an in-depth description of this process.
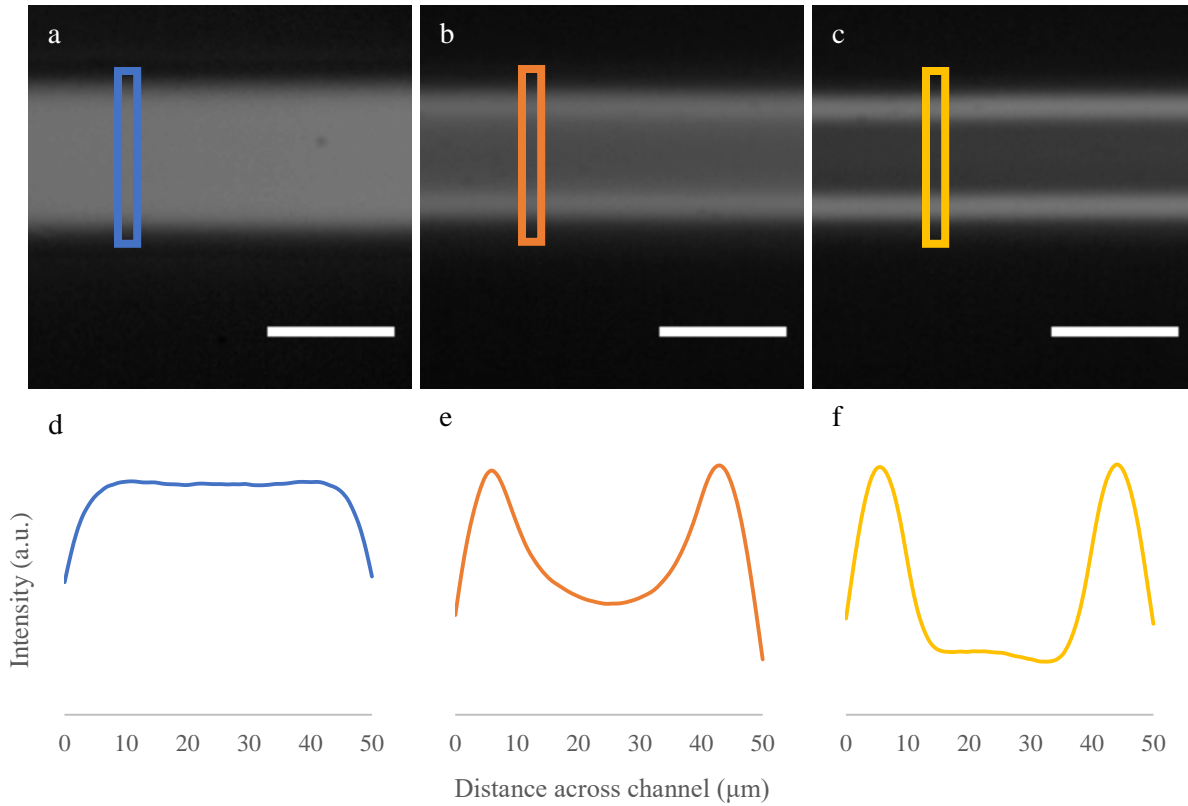
Figure 4.2 Top row: average composite of videos taken of a suspension of 10 μm spheres at (a) 1 mm, (b) 5 mm, and (c) 60 mm down a microfluidic channel showing the development of two equilibrium positions. Scale bars are 50 μm. Bottom row: intensity profiles plotted against the channel position (normal to the direction of flow). These are measured across the channel from the above average images at (d) 1 mm down channel, (e) 5 mm from entrance, and (f) 60 mm down the channel.
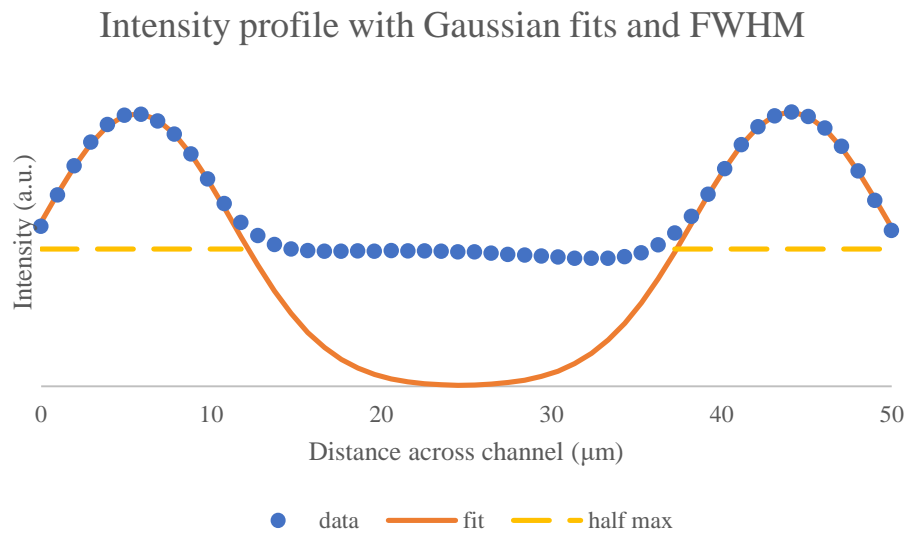
Figure 4.3 Example of measuring full width at half maximum (FWHM) of Gaussian fit for each peak in the intensity profile. This experiment was for a suspension of 10 μm spheres at 60 mm from the channel entrance.

46

FWHM measurements at different positions down the channel
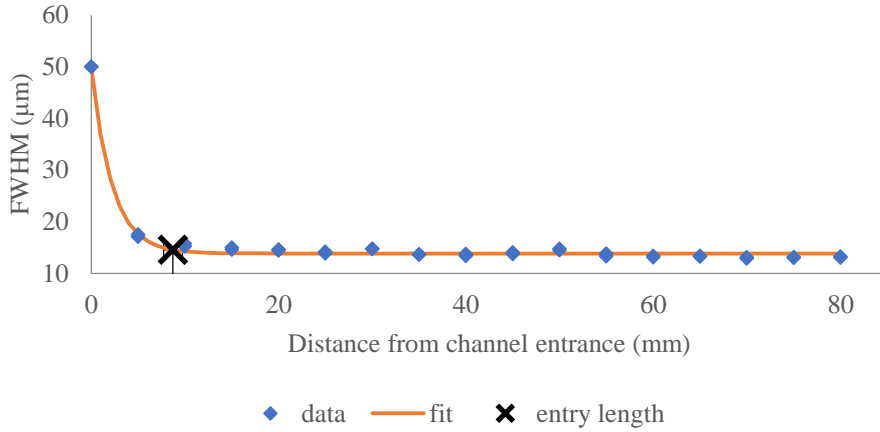
Figure 4.4 Plot of FWHMs measured from intensity profiles of videos taken at different positions down the channel. Entry length is marked to denote where fit falls within 5% of horizontal asymptote. This data is for an experiment run with 10 μm spheres.

4.3   Results

All sphere experiments used suspensions with a total volume fraction of 0.01% to ensure that the suspension was dilute enough to prevent sphere interactions and to enable inertial focusing. The devices used for these experiments were all 93 μm high and about 50 μm wide. The consistency of the measurement method described in the previous section was validated by looking at the results from a monodisperse suspension of 10 μm spheres. This experiment was repeated three times (see Figure 4.5), and the mean resulting entry length was measured to be 9.1 mm with a standard deviation of 1.2 mm.

Entry length of 10 μm spheres
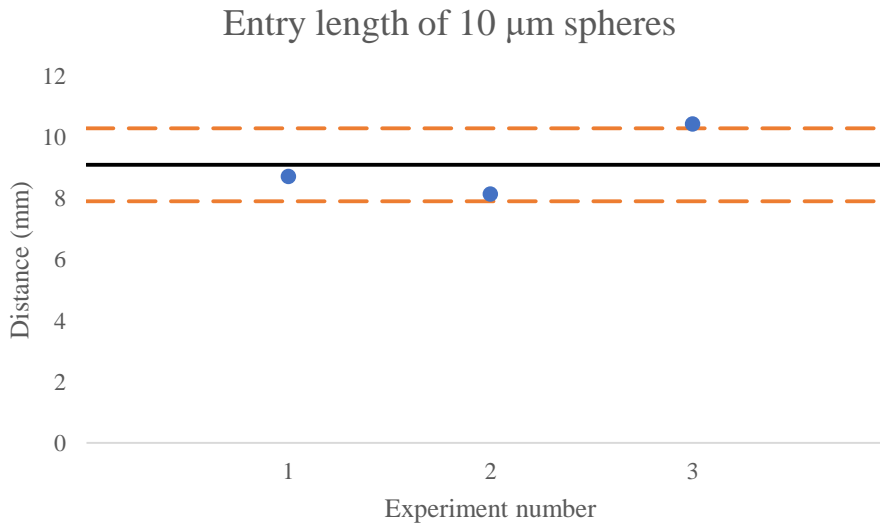
Figure 4.5 Consistency of experimental measurements. Mean and standard deviation: 9.1 ± 1.2 mm. The solid black line represents the average value of the three measured entry lengths. The dashed orange lines represent the standard deviation.

47

A bidisperse suspension of 10 μm and 5 μm spheres was investigated next (see Figure 4.6). Different volume fraction ratios were used to investigate the effect the 5 μm spheres might have on the migration entry length of the 10 μm spheres. Preliminary results for a second bidisperse mixture of spheres is also tested for comparison to the 5 μm and 10 μm results. This mixture uses 10 μm and 15 μm spheres in similar volume fraction ratios (Figure 4.7).
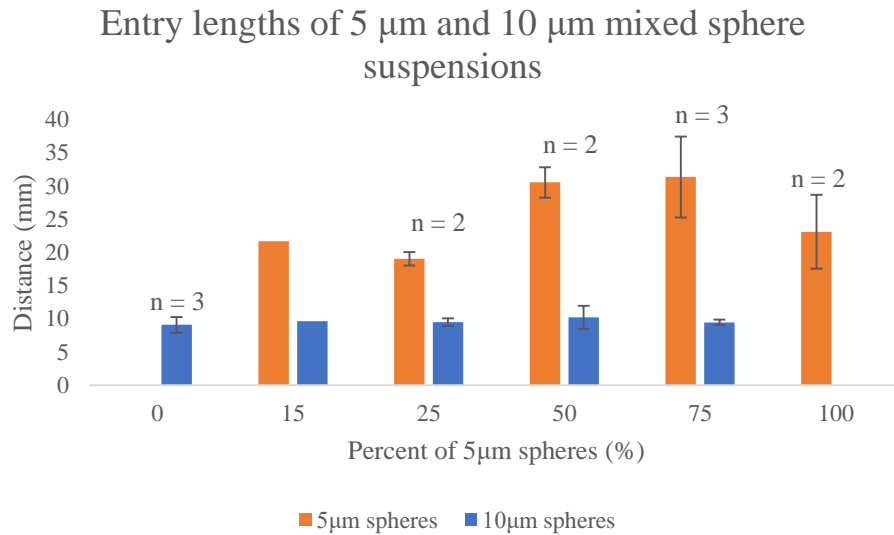
Figure 4.6 Entry length measurements for suspensions of 5 μm and 10 μm spheres mixed in different volume percentages. Total volume fraction of spheres is 0.01%. Error bars represent the standard deviation in measured entry lengths if multiple experiments were conducted.
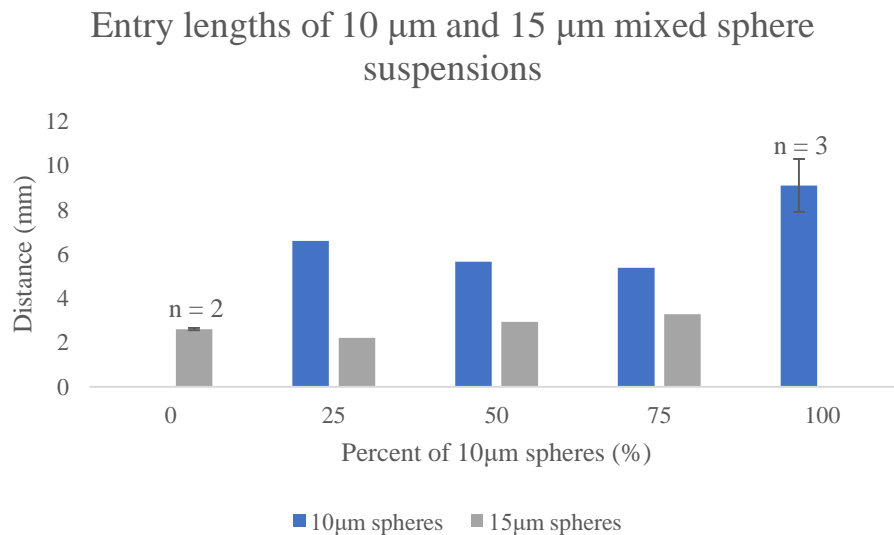
Figure 4.7 Entry length measurements for suspensions of 10 μm and 15 μm spheres at different volume percentages. Total volume fraction of each suspension is 0.01%.

The entry lengths of the 50/50 bidisperse mixtures (both 5 μm and 10 μm, and 15 μm and 10 μm) are plotted with the monodisperse results to compare how spheres that are 50% smaller and spheres that are 50% larger may affect the resulting entry length.
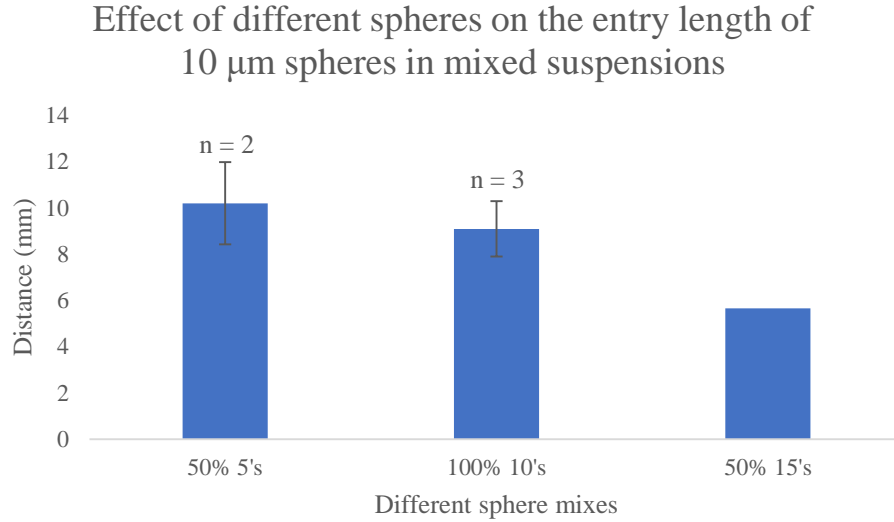
Figure 4.8 Comparison of entry lengths of monodisperse and bidisperse suspensions. Preliminary data shows the 50/50 mixture of 10 μm spheres and 15 μm spheres has a shorter entry length than the monodisperse results.

Values for the entry lengths reported in the above figures can be found in Table 4.2. Here, μ_S is the size of the smaller spheres, and μ_L is the size of the larger spheres for bidisperse suspensions. ϕ_S is the volume percent of small spheres and ϕ_L is the volume percentage of large spheres. The *"Focus"* column indicates the sphere size that corresponds to the reported entry length. When multiple measurements are conducted, the average entry length and standard deviation of those measurements are reported.

μ_S/μ_L	ϕ_S/ϕ_L	Focus	Entry length (mm)	Standard deviation (mm)	No. of replicates, n	Predicted entry length[28] (mm)
5/-	100/-	5	23.1	5.6	2	67
5/10	15/85	5	21.7	N/A	1	
5/10	15/85	10	9.6	N/A	1	
5/10	25/75	5	19.0	1.0	2	
5/10	25/75	10	9.5	0.6	2	
5/10	50/50	5	30.5	2.3	2	
5/10	50/50	10	10.2	1.8	2	
5/10	75/25	5	31.4	6.1	3	
5/10	75/25	10	9.5	0.4	3	
10/-	100/-	10	9.1	1.2	3	8
10/15	25/75	10	6.6	N/A	1	
10/15	25/75	15	2.2	N/A	1	
10/15	50/50	10	5.7	N/A	1	
10/15	50/50	15	2.9	N/A	1	
10/15	75/25	10	5.4	N/A	1	
10/15	75/25	15	3.3	N/A	1	
-/15	-/100	15	2.6	0.05	2	2

Table 4.2 Entry length values for sphere migration experiments.

4.4   Discussion and conclusions

From Figure 4.8, the presence of the larger spheres (15 µm) appears to reduce the entry length of the smaller 10 µm spheres, even though the overall suspension is extremely dilute. Figure 4.6 indicates that the presence of the 5 µm spheres has little to no effect on the migration entry length of the 10 µm spheres; although, in contrast to Figure 4.7, it suggests that the addition of small amounts of 10 µm spheres increases the entry length of the 5 µm. Figure 4.7 contains preliminary data, but appears to reinforce the trend of the larger spheres remaining relatively unaffected by the presence of the smaller spheres, while indicating that the presence of the larger spheres can reduce the entry length of the smaller spheres under some conditions.

It may be possible that the channel confinement of the 5 µm spheres (characterized by Re_p) contributes to the observed increase in entry length as 10 µm spheres are first introduced. The 10 and 15 µm spheres migrate much faster than the 5 µm spheres due to increased contribution of wall effects (the wall confinement is greater with higher Re_p – see Table 4.3). As the 10 µm spheres outcompete the 5 µm spheres for the same focusing position, when small numbers of the 10 µm spheres are first introduced, they may be dispersing the 5 µm spheres and lead to the observed longer entry lengths for the small spheres. Once the volume fraction of 10 µm spheres has surpassed some critical value, they may now work cooperatively with the smaller spheres and reduce the entry length, similar to what is observed with the experiments that used a mixed suspension of 10 µm and 15 µm spheres.

Sphere diameter (µm)	$Re_p = Re\left(\dfrac{a^2}{D_h^2}\right)$
5	0.12
10	0.47
15	1.06

Table 4.3 Particle Reynolds number values for spheres.

The entry length equation postulated by Zhang et al.[28] provided the closest entry length predictions for monodisperse suspensions to the entry lengths observed here for both monodisperse and bidisperse suspensions (see Table 4.2); however, all of the estimates were off for the 5 µm spheres. The variation in entry length may be due to the heavy weighting the effects of particle diameter or characteristic channel length are given. While these equations may not have the answer to inertial migration behavior over a wide range of particle sizes or channel geometries, they remain a good starting point for designing microfluidic channels.

The implication of these results is that even in very dilute conditions, where the particles are not expected to interact with each other, it is possible that particle-particle interactions are still taking place. These initial results indicate that the question of how polydispersity affects the migration behavior and entry length merits more study. A larger study of different mixtures of sphere sizes and channel geometries and total volume fractions could provide some interesting insight into this phenomenon. Additionally, it would be of interest to study the migration of polydisperse suspensions of deformable particles or vesicles, to see how deformability influences the migration question.

Chapter 5. Conclusions

The objective of this dissertation was to gain insight into the driving forces behind the collective migration behavior of vesicle suspensions. In order to meet this goal, a protocol for the generation of well-controlled, monodisperse vesicle suspensions was required. After conducting the parametric study of the electroformation process, it was clear that *that* particular route of investigation would not lead to significant reductions in the polydispersity of the electroformed vesicle suspensions. In an effort to find another way to reduce the polydispersity, several microfluidic separation devices were investigated. Designing and developing the methods to fabricate and operate these devices proved more challenging than initially considered. Some designs were unable to be successfully fabricated, others failed to separate the vesicles at all. In the designs that proved successful, issues stemming from devices clogging with lipids or other debris had to be addressed. Differences in device performance were observed when testing the separation devices with a model rigid particle suspension compared to the model deformable particle suspension. While rigid spherical particles are generally a good first estimation for how a microfluidic device will work with the end suspension of interest, these resulting differences show that there is a definite need for model deformable particle suspensions with which to test new microfluidic designs – especially if the end application involves suspensions of deformable particles or cells. This work showed that different separation mechanisms have different strengths pertaining to how a polydisperse vesicle suspension is separated. A particular separation mechanism and microfluidic design should be chosen depending on the target particles and how the resulting suspension purity or separation efficiency of the device are valued (the filtration device yields relatively high purity; the inertial device has higher separation efficiency). For testing migration behavior of vesicle suspensions, the filtration device was the most promising, as it showed the greatest ability to reduce the suspension polydispersity at the highest throughputs. The separated vesicle suspensions retained a degree of polydispersity, the effect of which should be determined before comparing the migration results of deformable vesicle suspensions to the results obtained for monodisperse rigid spheres.

With the purpose of gaining insight into how polydispersity would affect suspension migration, the well-studied inertial migration regime and an idealized suspension of rigid spheres was chosen as the next area to investigate. Polydispersity was introduced by combining monodisperse spheres of different sizes in a single suspension. The results presented in Chapter 4 indicate that the larger spheres may exert some influence over how the smaller spheres focus. Even though the suspensions were designed to be extremely dilute to minimize the chance of particle interactions, differences in migration length for spheres of a specific size are observed in bidisperse suspensions relative to the entry lengths measured in monodisperse suspensions. It should be noted that the story presented here is not complete, but is a step towards gaining a better understanding of how exactly polydispersity may affect the migration behavior of suspensions in channel flows.

At this moment, there are still no experiments published that investigate the collective migration behavior of vesicle suspensions. The work presented in this dissertation lays the groundwork for conducting this study, but the experiments required are certainly not trivial. First, it is important that a robust and accurate method for characterizing the suspension volume fraction is required. A significant amount of time was spent attempting different characterization methods, but vesicles pose an interesting set of challenges. The thin walls of the membrane mean that the vesicle is nearly invisible under standard brightfield contrast; it is possible to get slightly

improved contrast by diluting some of the suspending fluid with an equi-osmolar solution that has a different index of refraction, however, this usually isn't enough to make a significant difference in visibility and thus, adds to the challenge of characterizing the suspension. The vesicles generated in this work utilized a fluorescent lipid, so they were visible under fluorescent contrast methods. Flow cytometry is a high throughput characterization method that utilizes fluorescence to track and sort particles and cells, and several attempts were made to apply this method to vesicle suspensions. Again, this effort proved futile, possibly due to the sheathing flows containing chemicals that led to vesicle breakup or possibly being strong enough to shear the vesicles apart by themselves. The hemocytometer method that was eventually settled on might be able to be improved if access to stronger magnification phase objectives or perhaps a thinner hemocytometer slide is possible. The current method makes visualization of the vesicles fairly difficult.

Vesicle visualization must be addressed again when it comes to the suspension migration experiments. Preliminary inertial migration experiments with vesicles show that fluorescent vesicles are quite a bit dimmer than the fluorescent rigid spheres. If a higher magnification objective is desired than 20x (63x is available), the shorter working distance means that thinner glass slides must be used. The current slides used for fabricating the long microfluidic channels for these migration experiments are too thick for the higher magnification objectives to focus inside the channel. Thin glass coverslips can be used; however, these are generally not made to be very long – around half of the channel length currently utilized for the rigid sphere experiments. Glass capillaries (VitroCom) are available commercially (in limited channel geometries) and may prove to be a useful resource in conducting future migration experiments. While there are several challenges to conducting these migration experiments with vesicles, the information they could provide make them worthy of consideration.

To move forward in the study of deformable particle suspension migration behavior, the inertial migration regime is a good place to start because of how much previous work has been invested in studying ideal suspensions of rigid spheres. The electroformed and separated (to reduce polydispersity) vesicle suspension would be flowed through microfluidic channels of differing geometries (varying heights and widths) and the migration behavior would be measured in a similar way as that described in Chapter 4 with the suspension of rigid spheres. Conducting these experiments with differing concentrations of vesicles, from dilute (little to no particle interactions) to concentrated, would cover a wide parameter space and provide insight into the effects of deformability and concentration on the migration behavior. Again, this requires a reliable method of quantifying vesicle volume fraction – which may prove to be more challenging than expected. Comparing the separated vesicle suspension results to the results from experiments run with suspensions that have not been separated (extremely polydisperse suspensions) may provide answers as to how polydispersity interacts with deformability to influence the migration of these suspensions. Finally, studying these suspensions in the Stokes regime, where inertia of the fluid is not expected to play a role in the migration behavior, would provide data to compare to simulations of deformable particle suspensions that have been conducted.

The underlying physics of suspension flow behavior is an area of active research. This dissertation has made steps towards investigating the effects of polydispersity and deformability on collective suspension migration behavior through an effort to develop a protocol for well-controlled vesicle suspensions that have the potential to access a wider range of suspension parameters than those available through conventional cell studies, as well as initial migration

experiments with polydisperse sphere suspensions. This work has laid a foundation for future vesicle migration experiments that can provide insight into the driving forces behind the margination phenomena observed in suspensions of blood.

References

1. Mach, A. J. & Di Carlo, D. Continuous scalable blood filtration device using inertial microfluidics. *Biotechnol. Bioeng.* **107,** 302–311 (2010).
2. Zhao, H., Shaqfeh, E. S. G. & Narsimhan, V. Shear-induced particle migration and margination in a cellular suspension. *Phys. Fluids* **24,** 011902 (2012).
3. Kumar, A. & Graham, M. D. Margination and segregation in confined flows of blood and other multicomponent suspensions. *Soft Matter* **8,** 10536–10548 (2012).
4. Vlahovska, P. M., Podgorski, T. & Misbah, C. Vesicles and red blood cells in flow: From individual dynamics to rheology. *Comptes Rendus Phys.* **10,** 775–789 (2009).
5. Abreu, D., Levant, M., Steinberg, V. & Seifert, U. Fluid vesicles in flow. *Adv. Colloid Interface Sci.* **208,** 129–141 (2014).
6. Bacia, K. & Schweizer, J. Practical Course: Giant Unilamellar Vesicles. (2005).
7. Dahl, J. B. *et al.* Experimental observation of the asymmetric instability of intermediate-reduced-volume vesicles in extensional flow. *Soft Matter* **12,** 3787–3796 (2016).
8. Leal, L. G. Particle Motions in a Viscous Fluid. *Annu. Rev. Fluid Mech.* **12,** 435–476 (1980).
9. Smart, J. R. & Leighton, D. T. Measurement of the drift of a droplet due to the presence of a plane. *Phys. Fluids Fluid Dyn.* **3,** 21–28 (1991).
10. Coupier, G., Kaoui, B., Podgorski, T. & Misbah, C. Noninertial lateral migration of vesicles in bounded Poiseuille flow. *Phys. Fluids* **20,** 111702 (2008).
11. Farutin, A. & Misbah, C. Symmetry breaking and cross-streamline migration of three-dimensional vesicles in an axial Poiseuille flow. *Phys. Rev. E* **89,** 042709 (2014).
12. Abkarian, M. & Viallat, A. Dynamics of Vesicles in a Wall-Bounded Shear Flow. *Biophys. J.* **89,** 1055–1066 (2005).
13. Lyon, M. K. & Leal, L. G. An experimental study of the motion of concentrated suspensions in two-dimensional channel flow. Part 1. Monodisperse systems. *J. Fluid Mech.* **363,** 25–56 (1998).
14. Koh, C. J., Hookham, P. & Leal, L. G. An experimental investigation of concentrated suspension flows in a rectangular channel. *J. Fluid Mech.* **266,** 1–32 (1994).
15. Eckstein, E. C., Bailey, D. G. & Shapiro, A. H. Self-diffusion of particles in shear flow of a suspension. *J. Fluid Mech.* **79,** 191–208 (1977).
16. Leighton, D. & Acrivos, A. The shear-induced migration of particles in concentrated suspensions. *J. Fluid Mech.* **181,** 415–439 (1987).
17. Nott, P. R. & Brady, J. F. Pressure-driven flow of suspensions: simulation and theory. *J. Fluid Mech.* **275,** 157–199 (1994).
18. Lyon, M. K. & Leal, L. G. An experimental study of the motion of concentrated suspensions in two-dimensional channel flow. Part 2. Bidisperse systems. *J. Fluid Mech.* **363,** 57–77 (1998).
19. Clausen, J. R., Reasor, D. A. & Aidun, C. K. The rheology and microstructure of concentrated non-colloidal suspensions of deformable capsules. *J. Fluid Mech.* **685,** 202–234 (2011).

20. Kumar, A. & Graham, M. D. Mechanism of Margination in Confined Flows of Blood and Other Multicomponent Suspensions. *Phys. Rev. Lett.* **109,** 108102 (2012).

21. Kumar, A., Rivera, R. G. H. & Graham, M. D. Flow-induced segregation in confined multicomponent suspensions: effects of particle size and rigidity. *J. Fluid Mech.* **738,** 423–462 (2014).

22. Segré, G. & Silberberg, A. Behaviour of macroscopic rigid spheres in Poiseuille flow Part 2. Experimental results and interpretation. *J. Fluid Mech.* **14,** 136–157 (1962).

23. Matas, J.-P., Morris, J. F. & Guazzelli, É. Inertial migration of rigid spherical particles in Poiseuille flow. *J. Fluid Mech.* **515,** 171–195 (2004).

24. Liu, C., Hu, G., Jiang, X. & Sun, J. Inertial focusing of spherical particles in rectangular microchannels over a wide range of Reynolds numbers. *Lab. Chip* **15,** 1168–1177 (2015).

25. Cox, R. G. & Brenner, H. The lateral migration of solid particles in Poiseuille flow — I theory. *Chem. Eng. Sci.* **23,** 147–173 (1968).

26. Ho, B. P. & Leal, L. G. Inertial migration of rigid spheres in two-dimensional unidirectional flows. *J. Fluid Mech.* **65,** 365–400 (1974).

27. Saffman, P. G. The lift on a small sphere in a slow shear flow. *J. Fluid Mech.* **22,** 385–400 (1965).

28. Zhang, J. *et al.* Fundamentals and applications of inertial microfluidics: a review. *Lab. Chip* **16,** 10–34 (2015).

29. Zhou, J. & Papautsky, I. Fundamentals of inertial focusing in microchannels. *Lab. Chip* **13,** 1121–1132 (2013).

30. Choi, Y.-S., Seo, K.-W. & Lee, S.-J. Lateral and cross-lateral focusing of spherical particles in a square microchannel. *Lab. Chip* **11,** 460–465 (2011).

31. Di Carlo, D. Inertial microfluidics. *Lab. Chip* **9,** 3038–3046 (2009).

32. Misbah, C. Soft suspensions: inertia cooperates with flexibility. *J. Fluid Mech.* **760,** 1–4 (2014).

33. Shin, S. J. & Sung, H. J. Dynamics of an elastic capsule in moderate Reynolds number Poiseuille flow. *Int. J. Heat Fluid Flow* **36,** 167–177 (2012).

34. Kilimnik, A., Mao, W. & Alexeev, A. Inertial migration of deformable capsules in channel flow. *Phys. Fluids* **23,** 123302 (2011).

35. Tanaka, T. *et al.* Separation of cancer cells from a red blood cell suspension using inertial force. *Lab. Chip* **12,** 4336–4343 (2012).

36. Zhou, J., Giridhar, P. V., Kasper, S. & Papautsky, I. Modulation of rotation-induced lift force for cell filtration in a low aspect ratio microchannel. *Biomicrofluidics* **8,** 044112 (2014).

37. Wu, Z., Willing, B., Bjerketorp, J., Jansson, J. K. & Hjort, K. Soft inertial microfluidics for high throughput separation of bacteria from human blood cells. *Lab. Chip* **9,** 1193–1199 (2009).

38. Faivre, M., Abkarian, M., Bickraj, K. & Stone, H. A. Geometrical focusing of cells in a microfluidic device: An approach to separate blood plasma. *Biorheology* **43,** 147–159 (2006).

39. Hur, S. C., Henderson-MacLennan, N. K., McCabe, E. R. B. & Carlo, D. D. Deformability-based cell classification and enrichment using inertial microfluidics. *Lab. Chip* **11,** 912–920 (2011).

40. Amini, H., Lee, W. & Carlo, D. D. Inertial microfluidic physics. *Lab. Chip* **14,** 2739–2761 (2014).

41. Gossett, D. R. & Di Carlo, D. Particle Focusing Mechanisms in Curving Confined Flows. *Anal. Chem.* **81,** 8459–8465 (2009).

42. Salac, D. & Miksis, M. J. Reynolds number effects on lipid vesicles. *J. Fluid Mech.* **711,** 122–146 (2012).

43. Lim, E. J., Ober, T. J., Edd, J. F., McKinley, G. H. & Toner, M. Visualization of microscale particle focusing in diluted and whole blood using particle trajectory analysis. *Lab. Chip* **12,** 2199–2210 (2012).

44. Han, M., Kim, C., Kim, M. & Lee, S. Particle migration in tube flow of suspensions. *J. Rheol.* **43,** 1157–1174 (1999).

45. Kazerooni, H. T., Fornari, W., Hussong, J. & Brandt, L. Inertial migration in dilute and semi-dilute suspensions of rigid particles in laminar square duct flow. *ArXiv170508734 Phys.* (2017).

46. Krüger, T., Kaoui, B. & Harting, J. Interplay of inertia and deformability on rheological properties of a suspension of capsules. *J. Fluid Mech.* **751,** 725–745 (2014).

47. van Dinther, A. M. C., Schroën, C. G. P. H., Vergeldt, F. J., van der Sman, R. G. M. & Boom, R. M. Suspension flow in microfluidic devices — A review of experimental techniques focussing on concentration and velocity gradients. *Adv. Colloid Interface Sci.* **173,** 23–34 (2012).

48. Tanaka, T. *et al.* Inertial migration of cancer cells in blood flow in microchannels. *Biomed. Microdevices* **14,** 25–33 (2012).

49. Walde, P., Cosentino, K., Engel, H. & Stano, P. Giant Vesicles: Preparations and Applications. *ChemBioChem* **11,** 848–865 (2010).

50. Reeves, J. P. & Dowben, R. M. Formation and properties of thin-walled phospholipid vesicles. *J. Cell. Physiol.* **73,** 49–60 (1969).

51. Teh, S.-Y., Khnouf, R., Fan, H. & Lee, A. P. Stable, biocompatible lipid vesicle generation by solvent extraction-based droplet microfluidics. *Biomicrofluidics* **5,** 044113 (2011).

52. Nishimura, K., Suzuki, H., Toyota, T. & Yomo, T. Size control of giant unilamellar vesicles prepared from inverted emulsion droplets. *J. Colloid Interface Sci.* **376,** 119–125 (2012).

53. Shum, H. C., Lee, D., Yoon, I., Kodger, T. & Weitz, D. A. Double Emulsion Templated Monodisperse Phospholipid Vesicles. *Langmuir* **24,** 7651–7653 (2008).

54. Massenburg, D. & Lentz, B. R. Poly (ethylene glycol)-induced fusion and rupture of dipalmitoylphosphatidylcholine large, unilamellar extruded vesicles. *Biochemistry (Mosc.)* **32,** 9172–9180 (1993).

55. Stachowiak, J. C., Richmond, D. L., Li, T. H., Brochard-Wyart, F. & Fletcher, D. A. Inkjet formation of unilamellar lipid vesicles for cell-like encapsulation. *Lab. Chip* **9,** 2003–2009 (2009).

56. Dimitrov, D. S. & Angelova, M. I. Lipid swelling and liposome formation on solid surfaces in external electric fields. in *New Trends in Colloid Science* 48–56 (Steinkopff, 1987). doi:10.1007/3-798-50724-4_62

57. Angelova, M. I. & Dimitrov, D. S. Liposome electroformation. *Faraday Discuss. Chem. Soc.* **81,** 303–311 (1986).

58. Angelova, M. & Dimitrov, D. S. A mechanism of liposome electroformation. in *Trends in Colloid and Interface Science II* 59–67 (Steinkopff, 1988). doi:10.1007/BFb0114171

59. Okumura, Y. & Iwata, Y. Electroformation of Giant Vesicles and Electrode Polarity. *Bull. Chem. Soc. Jpn.* **84,** 1147–1149 (2011).

60. Politano, T. J., Froude, V. E., Jing, B. & Zhu, Y. AC-electric field dependent electroformation of giant lipid vesicles. *Colloids Surf. B Biointerfaces* **79,** 75–82 (2010).

61. Dimitrov, D. S. & Angelova, M. I. Lipid swelling and liposome formation mediated by electric fields. *J. Electroanal. Chem. Interfacial Electrochem.* **253,** 323–336 (1988).

62. Estes, D. J. & Mayer, M. Electroformation of giant liposomes from spin-coated films of lipids. *Colloids Surf. B Biointerfaces* **42,** 115–123 (2005).

63. Spjut, J. E. Trapping, deformation, and dynamics of phospholipid vesicles. (University of California, Berkeley, 2010).

64. Storslett, K. J. & Muller, S. J. Evaluation and comparison of two microfluidic size separation strategies for vesicle suspensions. *Biomicrofluidics* **11,** 034112 (2017).

65. Shields IV, C. W., Ohiri, K. A., Szott, L. M. & López, G. P. Translating microfluidics: Cell separation technologies and their barriers to commercialization. *Cytometry B Clin. Cytom.* **92,** 115–125 (2017).

66. Bhagat, A. A. S. *et al.* Microfluidics for cell separation. *Med. Biol. Eng. Comput.* **48,** 999–1014 (2010).

67. Gossett, D. R. *et al.* Label-free cell separation and sorting in microfluidic systems. *Anal. Bioanal. Chem.* **397,** 3249–3267 (2010).

68. Di Carlo, D., Edd, J. F., Irimia, D., Tompkins, R. G. & Toner, M. Equilibrium Separation and Filtration of Particles Using Differential Inertial Focusing. *Anal. Chem.* **80,** 2204–2211 (2008).

69. Kuntaegowdanahalli, S. S., Bhagat, A. A. S., Kumar, G. & Papautsky, I. Inertial microfluidics for continuous particle separation in spiral microchannels. *Lab. Chip* **9,** 2973–2980 (2009).

70. Geislinger, T. M. & Franke, T. Hydrodynamic lift of vesicles and red blood cells in flow — from Fåhræus & Lindqvist to microfluidic cell sorting. *Adv. Colloid Interface Sci.* **208,** 161–176 (2014).

71. Uchegbu, I. F. & Vyas, S. P. Non-ionic surfactant based vesicles (niosomes) in drug delivery. *Int. J. Pharm.* **172,** 33–70 (1998).

72. Danker, G., Vlahovska, P. M. & Misbah, C. Vesicles in Poiseuille Flow. *Phys. Rev. Lett.* **102,** 148102 (2009).

73. Farutin, A. *et al.* Dynamics of flexible fibers and vesicles in Poiseuille flow at low Reynolds number. *Soft Matter* **12,** 7307–7323 (2016).

74. Gires, P.-Y., Srivastav, A., Misbah, C., Podgorski, T. & Coupier, G. Pairwise hydrodynamic interactions and diffusion in a vesicle suspension. *Phys. Fluids* **26,** 013304 (2014).

75. Farutin, A. & Misbah, C. Analytical and Numerical Study of Three Main Migration Laws for Vesicles Under Flow. *Phys. Rev. Lett.* **110,** 108104 (2013).

76. Misbah, C. Vesicles, capsules and red blood cells under flow. *J. Phys. Conf. Ser.* **392,** 012005 (2012).

77. Lamura, A. & Gompper, G. Dynamics and rheology of vesicle suspensions in wall-bounded shear flow. *EPL Europhys. Lett.* **102,** 28004 (2013).

78. Noguchi, H., Gompper, G., Schmid, L., Wixforth, A. & Franke, T. Dynamics of fluid vesicles in flow through structured microchannels. *EPL Europhys. Lett.* **89,** 28002 (2010).

79. Noguchi, H. & Gompper, G. Vesicle dynamics in shear and capillary flows. *J. Phys. Condens. Matter* **17,** S3439 (2005).

80. van Swaay, D. & deMello, A. Microfluidic methods for forming liposomes. *Lab. Chip* **13,** 752–767 (2013).

81. Arriaga, L. R. *et al.* Ultrathin Shell Double Emulsion Templated Giant Unilamellar Lipid Vesicles with Controlled Microdomain Formation. *Small* **10,** 950–956 (2014).

82. Angelova, M. I., Soléau, S., Méléard, P., Faucon, F. & Bothorel, P. Preparation of giant vesicles by external AC electric fields. Kinetics and applications. in *Trends in Colloid and Interface Science VI* 127–131 (Steinkopff, 1992). doi:10.1007/BFb0116295

83. Hope, M. J., Bally, M. B., Mayer, L. D., Janoff, A. S. & Cullis, P. R. Generation of multilamellar and unilamellar phospholipid vesicles. *Chem. Phys. Lipids* **40,** 89–107 (1986).

84. Woo, Y., Heo, Y., Shin, K. & Yi, G.-R. Hydrodynamic Filtration in Microfluidic Channels as Size-Selection Process for Giant Unilamellar Vesicles. *J. Biomed. Nanotechnol.* **9,** 610–614 (2013).

85. Choi, S. & Park, J.-K. Continuous hydrophoretic separation and sizing of microparticles using slanted obstacles in a microchannel. *Lab. Chip* **7,** 890–897 (2007).

86. Takagi, J., Yamada, M., Yasuda, M. & Seki, M. Continuous particle separation in a microchannel having asymmetrically arranged multiple branches. *Lab. Chip* **5,** 778–784 (2005).

87. Yamada, M., Nakashima, M. & Seki, M. Pinched Flow Fractionation: Continuous Size Separation of Particles Utilizing a Laminar Flow Profile in a Pinched Microchannel. *Anal. Chem.* **76,** 5465–5471 (2004).

88. Yang, S., Ündar, A. & Zahn, J. D. A microfluidic device for continuous, real time blood plasma separation. *Lab. Chip* **6,** 871–880 (2006).

89. Yamada, M. & Seki, M. Hydrodynamic filtration for on-chip particle concentration and classification utilizing microfluidics. *Lab. Chip* **5,** 1233–1239 (2005).

90. Choi, S., Song, S., Choi, C. & Park, J.-K. Continuous blood cell separation by hydrophoretic filtration. *Lab. Chip* **7,** 1532–1538 (2007).

91. Shevkoplyas, S. S., Yoshida, T., Munn, L. L. & Bitensky, M. W. Biomimetic Autoseparation of Leukocytes from Whole Blood in a Microfluidic Device. *Anal. Chem.* **77,** 933–937 (2005).

92. Geislinger, T. M. & Franke, T. Sorting of circulating tumor cells (MV3-melanoma) and red blood cells using non-inertial lift. *Biomicrofluidics* **7,** 044120 (2013).

93. Zheng, S. *et al.* Membrane microfilter device for selective capture, electrolysis and genomic analysis of human circulating tumor cells. *J. Chromatogr. A* **1162,** 154–161 (2007).

94. Huang, R. *et al.* A microfluidics approach for the isolation of nucleated red blood cells (NRBCs) from the peripheral blood of pregnant women. *Prenat. Diagn.* **28,** 892–899 (2008).

95. Huh, D. *et al.* Gravity-Driven Microfluidic Particle Sorting Device with Hydrodynamic Separation Amplification. *Anal. Chem.* **79,** 1369–1376 (2007).

96. Hiemenz, P. C. *Polymer chemistry: The basic concepts.* (Taylor & Francis, 1984).

97. Rodriguez, F. *Principles of polymer systems.* (Hemispher Pub. Corp., 1989).

98. Tam, C. K. W. & Hyman, W. A. Transverse motion of an elastic sphere in a shear field. *J. Fluid Mech.* **59,** 177–185 (1973).

99. Di Carlo, D., Irimia, D., Tompkins, R. G. & Toner, M. Continuous inertial focusing, ordering, and separation of particles in microchannels. *Proc. Natl. Acad. Sci.* **104,** 18892–18897 (2007).

100. Jimenez, M., Miller, B. & Bridle, H. L. Efficient separation of small microparticles at high flowrates using spiral channels: Application to waterborne pathogens. *Chem. Eng. Sci.* **157,** 247–254 (2017).

101. Khalkhal, F., Chaney, K. H. & Muller, S. J. Optimization and application of dry film photoresist for rapid fabrication of high-aspect-ratio microfluidic devices. *Microfluid. Nanofluidics* **20,** 153 (2016).

102. Kaoui, B., Farutin, A. & Misbah, C. Vesicles under simple shear flow: Elucidating the role of relevant control parameters. *Phys. Rev. E* **80,** 061905 (2009).

103. Sackmann, E. K., Fulton, A. L. & Beebe, D. J. The present and future role of microfluidics in biomedical research. *Nat. Lond.* **507,** 181–9 (2014).

104. Wu, L., Guan, G., Hou, H. W., Bhagat, A. A. S. & Han, J. Separation of Leukocytes from Blood Using Spiral Channel with Trapezoid Cross-Section. *Anal. Chem.* **84,** 9324–9331 (2012).

105. Ozkumur, E. *et al.* Inertial Focusing for Tumor Antigen–Dependent and –Independent Sorting of Rare Circulating Tumor Cells. *Sci. Transl. Med.* **5,** 179ra47-179ra47 (2013).

106. Hou, H. W. *et al.* Isolation and retrieval of circulating tumor cells using centrifugal forces. *Sci. Rep.* **3,** (2013).

107. Lee, M. G. *et al.* Inertial blood plasma separation in a contraction–expansion array microchannel. *Appl. Phys. Lett.* **98,** 253702 (2011).

108.	Martel, J. M. *et al.* Continuous Flow Microfluidic Bioparticle Concentrator. *Sci. Rep.* **5,** (2015).

109.	Birch, C. M., Hou, H. W., Han, J. & Niles, J. C. Identification of malaria parasite-infected red blood cell surface aptamers by inertial microfluidic SELEX (I-SELEX). *Sci. Rep.* **5,** srep11347 (2015).

110.	Tse, H. T. K. *et al.* Quantitative Diagnosis of Malignant Pleural Effusions by Single-Cell Mechanophenotyping. *Sci. Transl. Med.* **5,** 212ra163-212ra163 (2013).

111.	McLaughlin, J. B. The lift on a small sphere in wall-bounded linear shear flows. *J. Fluid Mech.* **246,** 249–265 (1993).

112.	Cherukat, P. & Mclaughlin, J. B. The inertial lift on a rigid sphere in a linear shear flow field near a flat wall. *J. Fluid Mech.* **263,** 1–18 (1994).

113.	Joseph, D. D. & Ocando, D. Slip velocity and lift. *J. Fluid Mech.* **454,** 263–286 (2002).

114.	Asmolov, E. S. The inertial lift on a spherical particle in a plane Poiseuille flow at large channel Reynolds number. *J. Fluid Mech.* **381,** 63–87 (1999).

115.	Chun, B. & Ladd, A. J. C. Inertial migration of neutrally buoyant particles in a square duct: An investigation of multiple equilibrium positions. *Phys. Fluids* **18,** 031704 (2006).

116.	Yang, B. H. *et al.* Migration of a sphere in tube flow. *J. Fluid Mech.* **540,** 109–131 (2005).

117.	Hood, K., Lee, S. & Roper, M. Inertial migration of a rigid sphere in three-dimensional Poiseuille flow. *J. Fluid Mech.* **765,** 452–479 (2015).

118.	Rubinow, S. I. & Keller, J. B. The transverse force on a spinning sphere moving in a viscous fluid. *J. Fluid Mech.* **11,** 447–459 (1961).

119.	Cox, R. G. & Hsu, S. K. The lateral migration of solid particles in a laminar flow near a plane. *Int. J. Multiph. Flow* **3,** 201–222 (1977).

120.	Feng, J., Hu, H. H. & Joseph, D. D. Direct simulation of initial value problems for the motion of solid bodies in a Newtonian fluid. Part 2. Couette and Poiseuille flows. *J. Fluid Mech.* **277,** 271–301 (1994).

121.	Cheng, I.-F., Froude, V. E., Zhu, Y., Chang, H.-C. & Chang, H.-C. A continuous high-throughput bioparticle sorter based on 3D traveling-wave dielectrophoresis. *Lab. Chip* **9,** 3193–3201 (2009).

122.	MacDonald, M. P., Spalding, G. C. & Dholakia, K. Microfluidic sorting in an optical lattice. *Nat. Lond.* **426,** 421–4 (2003).

123.	Petersson, F., Åberg, L., Swärd-Nilsson, A.-M. & Laurell, T. Free Flow Acoustophoresis: Microfluidic-Based Mode of Particle and Cell Separation. *Anal. Chem.* **79,** 5117–5123 (2007).

124.	Bhagat, A. A. S., Kuntaegowdanahalli, S. S. & Papautsky, I. Inertial microfluidics for continuous particle filtration and extraction. *Microfluid. Nanofluidics* **7,** 217–226 (2009).

Appendix A. Electroformation protocol

1. Hold indium tin oxide (ITO) slides (25 x 25 x 1.1 mm; Delta Technologies, Limited) with tweezers and rinse slides with methanol, acetone, and chloroform in a fume hood. Rinse rubber gasket with acetone. Avoid rinsing debris from tweezers onto slides; do not rub slides with kimwipes after rinsing. Air dry.
2. Measure resistance of each side of the ITO slides. The side that has a measurable resistance or the lower resistance (5-30Ω) is coated with ITO. This is the side that you want to put the lipid mixture on. Mark the uncoated side with a piece of lab tape.
3. Mix the lipids and solvent together in a small glass vial.
    a. Rinse a 100 µl glass gas-tight syringe (Hamilton) with chloroform three times (fill and discard) to clean.
    b. Then mix together lipids such that the total lipid concentration is 2 mg/ml and is composed of 80% 1,2-dioleoyl-*sn*-glycero-3-phosphocholine (DOPC) and 20% 1-oleoyl-2-{6-[(7-nitro-2-1,3-benzoxadiazol-4-yl)amino]hexanoyl}-*sn*-glycero-3-phosphocholine (NBD-PC) and the solvent composition is 95% chloroform and 5% acetonitrile.
    c. Note: typical experiments use about 1.5 ml of vesicles; this amount can be reached by setting up and running three electroformation cells. If each cell uses 30 µL of lipid mixture (15 µL per ITO slide), a mixture volume of 100 µL is useful to prepare.
    d. Store excess stock lipids under argon at -20°F and clean gas-tight syringes by rinsing with chloroform.
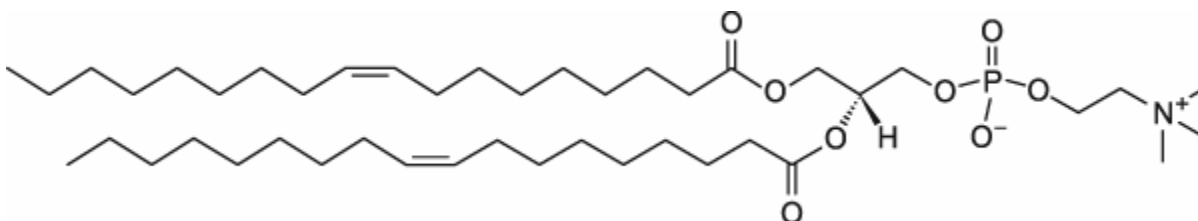

Figure A1 DOPC structure (Avanti Lipids 850375C).

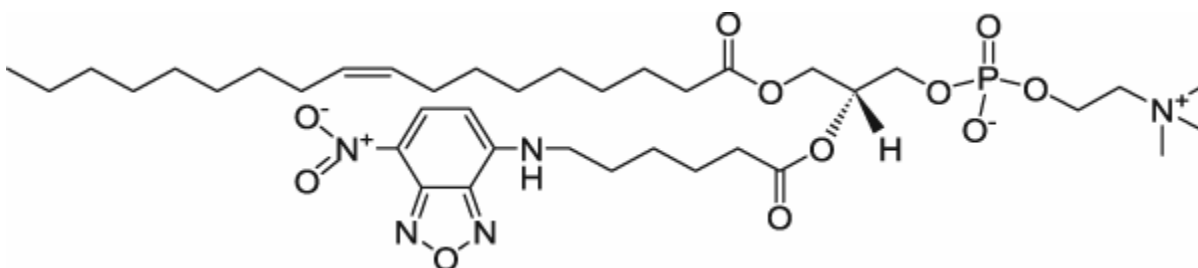**Figure A2** NBD-PC structure (Avanti Lipids 810132C).

4. Deposit and spread 15 µL of the lipid mixture onto each ITO slide with the syringe tip. Cover with foil and place under vacuum for half an hour to evaporate off the excess solvents.
5. Place copper tape on both sides of a 1.6mm rubber gasket, cut to fit the ITO slide dimensions.

6. Ensure that the function generator is on and recognized by the computer using Agilent Connection Expert.
7. Open the Electroformation_3r executable and click the Set I/O button. This interface should appear:
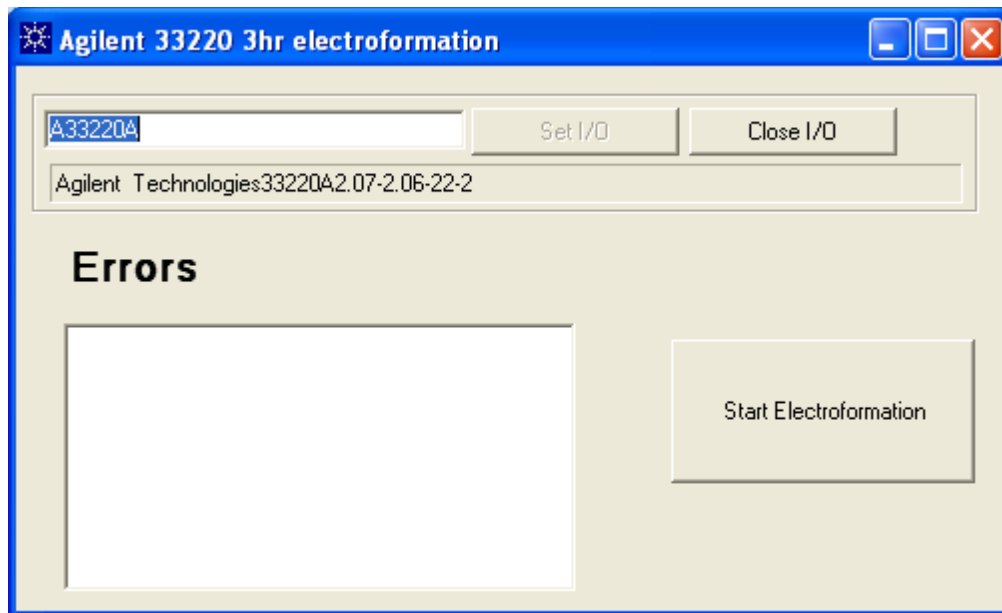
Figure A3 Electroformation interface.

8. Prepare 100 mM sucrose solution. Fill a 3 ml syringe with the aqueous solution and cap with 0.2 μm filter and 18G needle.
9. Remove the lipid coated ITO slides from the vacuum oven and quickly assemble the electroformation cell.
   a. Sandwich the copper tape-rubber spacer with two lipid covered ITO slides. The copper tape should be in contact with the ITO coating. Hold the cell together with small binder clips (Figure A4.a-b).
   b. Fill the cell with a 100mM sucrose solution using a syringe and needle through a small gap in the rubber spacer (Figure A4.c).
   c. Seal the gap with a small bit of Sculpey polymer clay (Figure A4.d). Water on the exterior of the cell can prevent proper sealing, so ensure the exterior is dry.
   d. Attach copper tape to function generator (Agilent 33220A) alligator clamps (Figure A4.e).


(a)　　　　　　(b)　　　　　　(c)　　　　　　(d)　　　　　　(e)
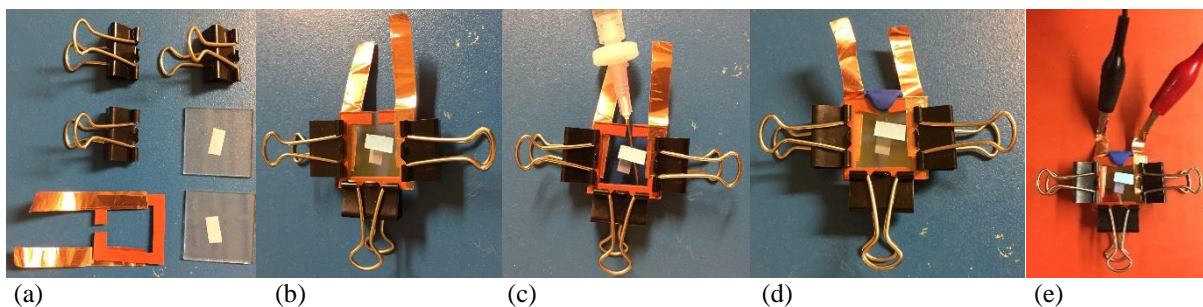
Figure A4 Compilation of electroformation cell.

10. Apply electric field by clicking the [Start Electroformation] button on the executable interface. First, a 10 Hz sine wave is linearly ramped from 0.05 V to 1.41 V over half an hour. A sine wave at 10 Hz and 1.41 V is then applied for the next two hours. To detach the vesicles from the electrode, a 2.12 V, 4.5 Hz square wave is applied for 30 minutes. The "output" light on the function generator will turn off at the end of the 3 hour cycle. See Jakob Spjut's Master's Thesis[63] for programming details.
11. Withdraw vesicles carefully and slowly with an 18G needle and deposit in 1.5 mL centrifuge tube. Vesicles can be stored, covered in foil, at room temperature or in 4°F fridge, but it is recommended to use the vesicles within a week.
12. Used ITO slides and rubber gaskets can be cleaned by sonicating in a 2% v/v micro-90 (International Products Corporation) cleaning solution for half an hour, then sonicating for another half hour in water. Let air dry.

Appendix B. Vesicle size analysis protocol

1. Assemble CoverWell apparatus by cutting out one well (Invitrogen C18139) per sample. Peel off adhesive protection layer and place adhesive side down onto a #1 coverslip (Fisher Scientific).
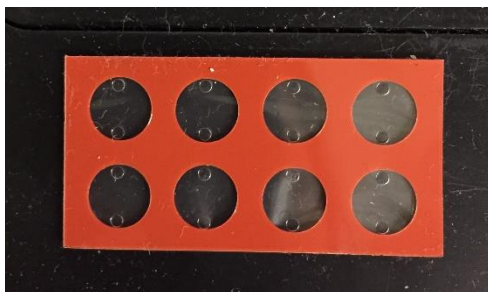
Figure B1 CoverWell example.

2. Mix 25 µl of vesicle sample with 25 µl 100 mM glucose solution in a 1.5 ml microcentrifuge tube. Gently stir with pipette tip – do not mix by pipetting up and down. This will break the vesicles up.
3. Slowly pipette up 40 µl of mixture and gently pipette into coverwell. Cover the inlet holes with clear scotch tape. Let settle for a few minutes, but not longer than 10-15 minutes as the vesicles may start breaking up after coming into extended contact with the glass coverslip.
4. Using the 63x magnification (Leica) objective and the Photometrics Cascade 512b CCD camera, take about 20 images throughout the coverwell, capturing vesicles. Make sure to close the fluorescent shutter while saving images to avoid photobleaching the vesicles.
5. Run MATLAB code (see below) to fit circles to visible vesicles; select good fits and reject poor fits.
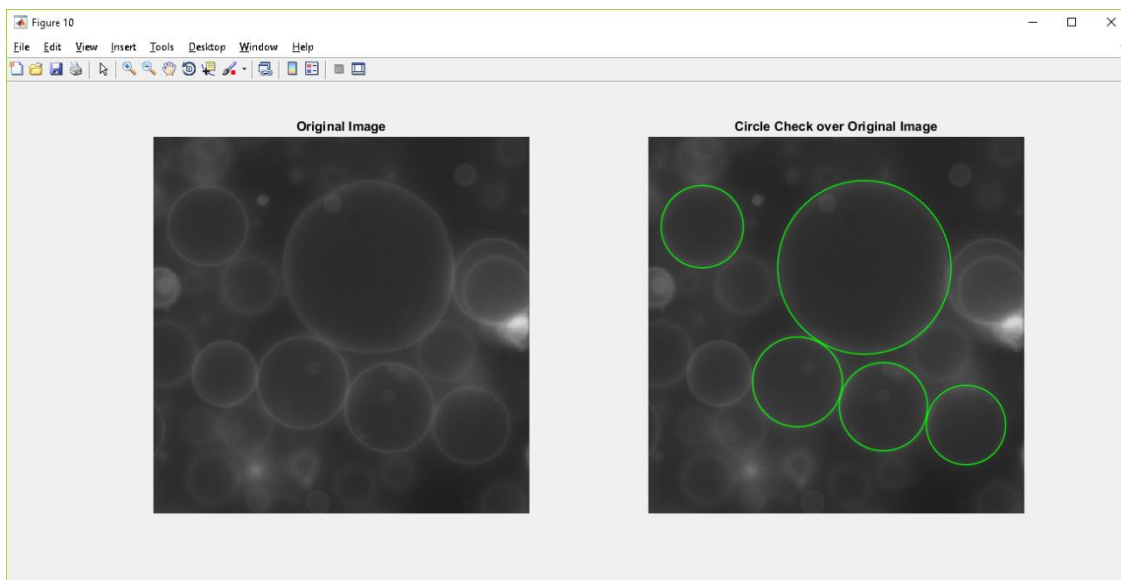
Figure B2 Vesicle image with MATLAB circle fitting.

6. Run code to export diameters to an Excel spreadsheet. May need to run a separate Matlab code with adjusted sensitivity parameters to capture larger vesicles (also listed below). Convert these measurements to Excel as well.
7. In Excel spreadsheet, convert radius measurements from pixels to microns. At 63x, with the Photometrics camera, 100 μm = 392 pixels. Put measurements in terms of diameter.
8. Calculate average, standard deviation, and polydispersity index (PDI). Graph histogram. Make sure you have at least 100 vesicles counted.

$$PDI = 1 + \left(\frac{\sigma}{\mu}\right)^2$$

Matlab code to determine vesicle size (adapted from Margaret Y. Hwang and Joanna B. Dahl)

```matlab
% Find circular vesicles in single image

close all % close all open figures

% circle finding options
sens = 0.70;
%method = 'twostage';
method = 'phasecode';

%% Load image (PNG)
% PNG image seems to give better contrast when MATLAB plotting
% This will be easier for the user when accepting/rejecting circles
file_start = 0;
totalf = 20;
for filen = file_start:totalf
    foldername = sprintf('test');
    fileName = sprintf('size %d.tif',filen);
    % fileName = '14.png';

    pathName = pwd;

    bw = imread(fileName);
    % figure; imshow(bw)

    outname=sprintf('%d.txt', filen);
    outpath = fullfile('F:', foldername, outname);
    fileOut = fopen(outpath, 'w');

    fprintf(fileOut,'Circlular Vesicle Finding in %12s',fileName);
    fprintf(fileOut,'\n');
    fprintf(fileOut,'Location : %100s',pathName);
    fprintf(fileOut,'\n\n');

    %% Find circles
    % Call |imfindcircles| on this image with the search radius of [20 25]
    % pixels.
```

```matlab
    % "A good rule of thumb is to choose radiusRange such that rmax < 3*rmin
    % and (rmax-rmin) < 100. The accuracy of imfindcircles is limited when
the
    % value of radius (or rmin) is less than 10." -- imfindcircles help

    % Assume using 63x objective: 393 px = 100 um
    % Break up radius range into 10 px segmemts
    nRange = 5;
    % Range 0:  5 - 10 px =  < 2.54 um
    % Range 1: 10 - 20 px =  2.54 -  5.09 um @ 63x
    % Range 2: 20 - 30 px =  5.09 -  7.63 um @ 63x
    % Range 3: 30 - 40 px =  7.63 -  10.18 um @ 63x
    % Range 4: 40 - 50 px = 10.18 - 12.72 um @ 63x
    % Range 5: 50 - 60 px = 12.72 - 15.27 um @ 63x
    % Range 6: 60 - 70 px = 15.27 - 17.81 um @ 63x

    figure('Position',[0   100   652*2   582]) % one screen
    % figure('Position',[-1437 391 1304   582]); % two screen
    subplot(1,2,1); hOrig = imshow(bw);
    title('Original Image')
    subplot(1,2,2); hCirc = imshow(bw); axCirc = gca;
    title('Circle Check over Original Image')

    % preallocate
    centers = cell(nRange); radii = cell(nRange);
    centersConf = cell(nRange); radiiConf = cell(nRange);
    nDiscard = zeros(nRange,1);
    centersKeep = [];  radiiKeep = []; hKeep = []; hRmv = [];
    discard = 0;

    for i = 2:nRange
        if i == 1
            range = [5 10];
        else
            range = [10*(i-1)-2 10*(i)+2];
        end

        [centers{i}, radii{i}] = imfindcircles(bw,range,...
            'ObjectPolarity','bright',...
            'Sensitivity',sens,'Method',method, 'EdgeThreshold', 0.03);

        currCtr = centers{i};
        currRad = radii{i};

        % output to file and screen
        fprintf('Found  %i  circles  in  the  range  %i  -  %i  px
\n',length(currRad),...
            10*i,10*(i+1))

        for j = 1:length(currRad)
            axes(axCirc)
            h                                                        =
viscircles(currCtr(j,:),currRad(j),'EdgeColor','y','LineWidth',1);
            home % return cursor to command window
            iKeep = input('Keep this vesicle? y/n    ','s');
```

66

```matlab
            if iKeep == 'y'
                centersKeep(end+1,1:2) = currCtr(j,:);
                radiiKeep(end+1,1) = currRad(j);
                delete(h)
                % green means go
                hKeep(end+1) = viscircles(currCtr(j,:),currRad(j),...
'EdgeColor','g','LineWidth',1,'DrawBackgroundCircle',false);
            elseif iKeep == 'n'
                disp('Circle discarded')
                nDiscard(i) = nDiscard(i) + 1;
                delete(h)
                % red means bad
        %          hRmv(end+1) = viscircles(currCtr(j,:),currRad(j),...
            %
'EdgeColor','r','LineWidth',1,'DrawBackgroundCircle',false);
            discard=discard+1;
            end
        end

        % save confirmed circle info
        centersConf{i} = centersKeep;
        radiiConf{i}  = radiiKeep;

        if ge(length(currRad),1)
            % write to output file
            fprintf(fileOut,'Kept %3i of %3i circles found in the radius
range %i - %i px \n',length(radiiKeep),...
                length(currRad),range(1),range(2));
            fprintf(fileOut,'%13s %13s %13s \n','CenterX [px]',...
                'CenterY [px]','Radius [px]');
            fprintf(fileOut,'%13.3f       %13.3f       %13.3f\n',[centersKeep
radiiKeep]');
        else
            fprintf(fileOut,'No circles found in the radius range %i - %i px
\n',...
                range(1),range(2));
        end
        fprintf(fileOut,'\n\n');
        % reset
        centersKeep = [];   radiiKeep = [];

    end

    % Save final image of selected particles
    figname = sprintf('%d', filen);
    figout = fullfile('F:', foldername, figname);
    savefig(gcf,figout);

    %% Option to add circles that were missed

    %% OUTPUT SUMMARY OF PARAMETERS

    fprintf(fileOut,'999');
    fprintf(fileOut,'\n');
```

67

```matlab
    fprintf(fileOut,'\n');
    fprintf(fileOut,'Total vesicles found = %6i;',length(hKeep));
    fprintf(fileOut,'\n');
    fprintf(fileOut,'Number discarded     = %6i;',discard);
    fprintf(fileOut,'\n');
    fprintf(fileOut,'\n');
    fprintf(fileOut,'Circle Finding options [imfindcircles] \n');
    fprintf(fileOut,'Sensitivity   = %4.2f;',sens);
    fprintf(fileOut,'\n');
    fprintf(fileOut,'Method        = %10s;',method);

    fclose(fileOut);

    % Close figure for new figure
    %close(gcf)

end
```

Matlab code for vesicles with diameter out of range (adapted from Margaret Y. Hwang)

```matlab
% Find circular vesicles in single image

close all % close all open figures

% circle finding options
sens = 0.8;
method = 'twostage';
% method = 'phasecode';

%% Load image (PNG)
% PNG image seems to give better contrast when MATLAB plotting
% This will be easier for the user when accepting/rejecting circles
file_start = 0;
totalf = 20;
for filen = file_start:totalf
    foldername = sprintf('testlarge');
    fileName = sprintf('size %d.tif',filen);
    % fileName = '14.png';

    pathName = pwd;

    bw = imread(fileName);
    % figure; imshow(bw)

    outname=sprintf('%d.txt', filen);
    outpath = [fullfile('F:', foldername, outname)];
    fileOut = fopen(outpath, 'w');

    fprintf(fileOut,'Circlular Vesicle Finding in %12s',fileName);
    fprintf(fileOut,'\n');
    fprintf(fileOut,'Location : %100s',pathName);
    fprintf(fileOut,'\n\n');
```

```matlab
    %% Find circles
    % Call |imfindcircles| on this image with the search radius of [20 25]
    % pixels.

    % "A good rule of thumb is to choose radiusRange such that rmax < 3*rmin
    % and (rmax-rmin) < 100. The accuracy of imfindcircles is limited when
the
    % value of radius (or rmin) is less than 10." -- imfindcircles help

    % Assume using 63x objective: 393 px = 100 um
    % Break up radius range into 10 px segmemts
    nRange = 25;
    % Range 0:  5 - 10 px =  < 2.54 um
    % Range 1: 10 - 20 px =  2.54 -  5.09 um @ 63x
    % Range 2: 20 - 30 px =  5.09 -  7.63 um @ 63x
    % Range 3: 30 - 40 px =  7.63 -  10.18 um @ 63x
    % Range 4: 40 - 50 px = 10.18 - 12.72 um @ 63x
    % Range 5: 50 - 60 px = 12.72 - 15.27 um @ 63x
    % Range 6: 60 - 70 px = 15.27 - 17.81 um @ 63x

    figure('Position',[0   50   652*2   582]) % one screen
    % figure('Position',[-1437 391 1304  582]); % two screen
    subplot(1,2,1); hOrig = imshow(bw);
    title('Original Image')
    subplot(1,2,2); hCirc = imshow(bw); axCirc = gca;
    title('Circle Check over Original Image')

    % preallocate
    centers = cell(nRange); radii = cell(nRange);
    centersConf = cell(nRange); radiiConf = cell(nRange);
    nDiscard = zeros(nRange,1);
    centersKeep = [];  radiiKeep = []; hKeep = []; hRmv = [];
    discard = 0;

    for i = 6:15
        if i == 1
            range = [7 10];
        else
            range = [10*(i-1)+1 10*(i)];
        end

        [centers{i}, radii{i}] = imfindcircles(bw,range,...
            'ObjectPolarity','bright',...
            'Sensitivity',sens,'Method',method, 'EdgeThreshold', 0.03);

        currCtr = centers{i};
        currRad = radii{i};

        % output to file and screen
        fprintf('Found  %i   circles   in   the   range   %i   -   %i   px
\n',length(currRad),...
            10*i,10*(i+1))

        for j = 1:length(currRad)
```

```matlab
            axes(axCirc)
            h                                                   =
viscircles(currCtr(j,:),currRad(j),'EdgeColor','y','LineWidth',1);
            home % return cursor to command window
            iKeep = input('Keep this vesicle? y/n   ','s');
            if iKeep == 'y'
                centersKeep(end+1,1:2) = currCtr(j,:);
                radiiKeep(end+1,1) = currRad(j);
                delete(h)
                % green means go
                hKeep(end+1) = viscircles(currCtr(j,:),currRad(j),...

'EdgeColor','g','LineWidth',1,'DrawBackgroundCircle',false);
            elseif iKeep == 'n'
                disp('Circle discarded')
                nDiscard(i) = nDiscard(i) + 1;
                delete(h)
                % red means bad
        %         hRmv(end+1) = viscircles(currCtr(j,:),currRad(j),...
            %
'EdgeColor','r','LineWidth',1,'DrawBackgroundCircle',false);
            discard=discard+1;
            end
        end

        % save confirmed circle info
        centersConf{i} = centersKeep;
        radiiConf{i}  = radiiKeep;

        if ge(length(currRad),1)
            % write to output file
            fprintf(fileOut,'Kept %3i of %3i circles found in the radius
range %i - %i px \n',length(radiiKeep),...
                length(currRad),range(1),range(2));
            fprintf(fileOut,'%13s %13s %13s \n','CenterX [px]',...
                'CenterY [px]','Radius [px]');
            fprintf(fileOut,'%13.3f      %13.3f       %13.3f\n',[centersKeep
radiiKeep]');
        else
            fprintf(fileOut,'No circles found in the radius range %i - %i px
\n',...
                range(1),range(2));
        end
        fprintf(fileOut,'\n\n');
        % reset
        centersKeep = [];  radiiKeep = [];

    end

    % Save final image of selected particles
    figname = sprintf('%d', filen);
    figout = [fullfile('F:', foldername, figname)];
    savefig(gcf,figout);

    %% Option to add circles that were missed
```

```matlab
    %% OUTPUT SUMMARY OF PARAMETERS

    fprintf(fileOut,'999');
    fprintf(fileOut,'\n');
    fprintf(fileOut,'\n');
    fprintf(fileOut,'Total vesicles found = %6i;',length(hKeep));
    fprintf(fileOut,'\n');
    fprintf(fileOut,'Number discarded     = %6i;',discard);
    fprintf(fileOut,'\n');
    fprintf(fileOut,'\n');
    fprintf(fileOut,'Circle Finding options [imfindcircles] \n');
    fprintf(fileOut,'Sensitivity   = %4.2f;',sens);
    fprintf(fileOut,'\n');
    fprintf(fileOut,'Method        = %10s;',method);

    fclose(fileOut);

    % Close figure for new figure
    %close(gcf)

end
```

Matlab code to export sizes to Excel (adapted from Margaret Y. Hwang)

```matlab
% Read txt files sequentially from another folder.
clear all
clc

% Preallocate array for total particles

Total = zeros(1000, 4);
Npart = 1;
for k = 29:39

    % Create a text file name, and read the file.
    filename = sprintf('%d.txt', k);
    foldername = 'test';
    textFileName = fullfile('F:', foldername, filename);
    %if exist(textFileName, 'file')
        fid = fopen(textFileName, 'rb');
        % Advance five lines:
        linesToSkip = 4;
        for ii = 1:linesToSkip-1
            fgetl(fid);
        end


        % Placeholder variable to keep loop going until end of file is
        % reached

        open = 1;
```

71

```matlab
while open==1

    % Check to see if vesicles were found in the first batch
    firstline = fgetl(fid);
    check = strsplit(firstline);

    if strcmp(check{1},'Kept') == 1

        % check to see number of particles kept
        particles = str2num(check{2});
        fprintf('%d\n', particles)
        if particles ~= 0;
            % Skip the header line
            fgetl(fid);
            for n = 1:particles
                Psizetemp = fgetl(fid);
                split = regexp(Psizetemp,'        ','split');

                if length(split) > 3
                    Psizetemp2 = split(2:end);
                else
                    Psizetemp2 = split;
                end

                Psizef = str2double(Psizetemp2);

                % Store the particle sizes
                Total(Npart,1)= Psizef(1);
                Total(Npart,2)= Psizef(2);
                Total(Npart,3)= Psizef(3);
                Total(Npart,4) = k;
                Npart = Npart + 1;

            end
        end

        % Advance to next line
        fgetl(fid);

    elseif strcmp(check{1}, 'Total') == 1
        fprintf('End\n')
        [a b] = size(check);
        split = check{b};
        npart = str2num(split);
        fprintf('Total number of particles = %d\n', npart)
        open = 0;

    else
        fprintf('No\n')
    end
end

textData = textscan(fid, '%s');
```

```matlab
        fclose(fid);
fprintf('File is %d\n', k)
end

headers = {'CenterX [px]', 'CenterY [px]', 'Radius [px]', 'Image'};
filename = 'ParticleSizes.xlsx';
xlswrite(filename, headers, 'Sheet1') % by defualt starts from A1
xlswrite(filename,  Total(1:Npart-1,:),  'Sheet1','A2')  % array  under  the
header.
```

Appendix C. Supplementary data for Chapter 3

Mean vesicle size for S_I, S_L, and S_S for different separation devices:

Suspension	Filter1 H30	Filter2 H30	Filter3 H30	Filter1 H60	Inertial H145
S_I (µm)	17.2	17.5	18.8	19.4	15.9
S_L (µm)	25.6	21.1	20.1	24.6	15.0
S_S (µm)	11.6	11.4	11.3	10.7	9.2

Table C1 Mean vesicle size of initial and separated suspensions from different separation devices.

Mean PDI values for different separation devices:

Device	Filter1 H30	Filter2 H30	Filter3 H30	Filter1 H60	Inertial H145
S_I	1.31	1.30	1.28	1.28	1.30
S_L	1.08	1.13	1.11	1.08	1.19
S_S	1.12	1.14	1.12	1.11	1.13

Table C2 Average PDI reported for initial and separated suspensions using different separation devices.

The separation metrics for more concentrated vesicle suspensions in Inertial H145 are reported in the following table.

Suspension volume fraction (ϕ)	$\approx 6\%$	$\approx 10\%$
E_L	4.3	2.9
E_S	3.4	6.2
SE_L	64%	66%
SE_S	89%	90%
P_L	90%	91%
P_S	61%	65%
$\Delta\mu$ (µm)	8.9	7.2
ΔPDI	0.02	0.05
T (µL/min)	~110	~183

Table C3 Separation metrics for more concentrated vesicle suspension in Inertial H145.

To quantify the degree of focusing in the Inertial H145 device, the fluorescence intensity profile across the channel near the device outlet was measured. The full width at half maximum (FWHM) of the intensity profile for each suspension dilution was calculated and is reported in Figure C1. Higher FWHM values of the more concentrated suspensions indicate less focusing behavior.
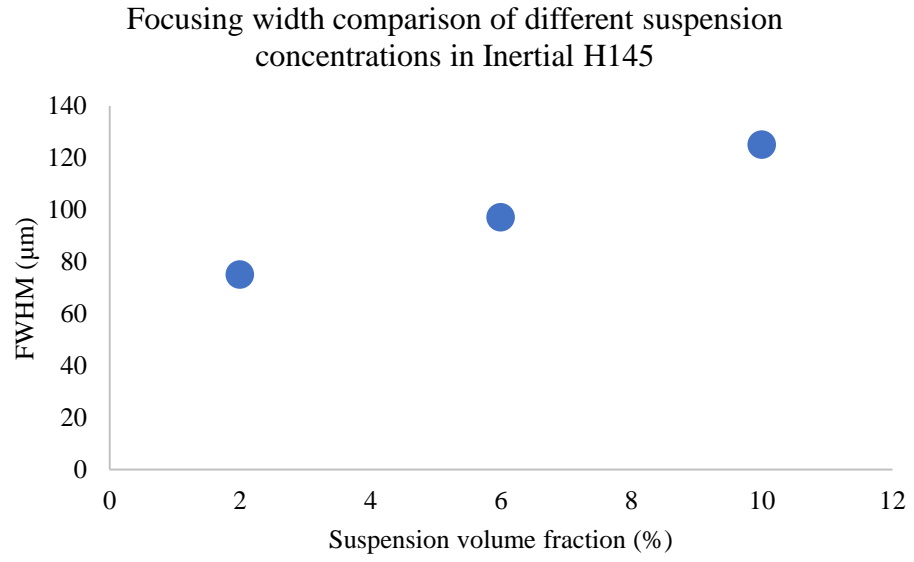
Figure C1 Comparison of FWHM for different suspension dilutions in Inertial H145.

Appendix D. SU-8 master fabrication protocol

This is done at the BNC. Contact Paul Lum (p_lum@berkeley.edu) or Naima Azgui (azgui@berkeley.edu) for training.

Protocol for making SU-8 master wafer at 60 μm high.

1. Turn on UV aligner. Wait 10 minutes before turning on UV light power switch. Measure UV power.
2. Set one hot plate to 65°C, one to 95°C, and one to 150°C.
3. Rinse silicon wafer with acetone, isopropyl alcohol (IPA), and de-ionized water. Dry with nitrogen stream, then place on 150°C hot plate for 15-30 minutes.
4. Program spincoater:
   a. 300rpm for 20s with ramping of 100rpm/s
   b. 500rpm for 20s with ramping of 100rpm/s
   c. 1300rpm for 30s with ramping of 300rpm/s
5. After the wafer dehydration bake (helps SU-8 adhere to the wafer surface), quickly move wafer to spincoater chuck, pour SU-8 2050 photoresist (MicroChem) in the center of the wafer, slowly – to avoid bubbles – until it covers about 1/3 of the wafer surface. Close lid and run spincoater program.
6. Remove SU-8 edge bead with TexWipe soaked in acetone.
7. Initiate soft bake step:
   a. Place wafer on 65°C hot plate for 3 minutes.
   b. Place wafer on 95°C hot plate for 9 minutes.
8. Calculate exposure time:

$$\frac{200\,\frac{mJ}{cm^2}}{\text{measured power}\left(\frac{mW}{cm^2}\right)} \times 1.5^2 = \text{exposure time (s)}$$

9. Load wafer on aligner stage. Place mylar mask with channel designs in the designated mask holder. Slowly raise wafer stage until mask is in contact with wafer (you will see the diffraction pattern in sections where contact is made). Set aligner timer and expose wafer to UV light.
10. Initial post-exposure bake step:
    a. Place wafer on 65°C hot plate for 2 minutes.
    b. Place wafer on 95°C hot plate for 7 minutes.
11. Remove mask from aligner. Let wafer cool briefly before developing away the unexposed SU-8. Turn off 65°C and 95°C hot plates.
12. Develop wafer by filling a Teflon dish with some SU-8 developer and shaking wafer around for a few minutes. Watch wafer to determine when it has finished developing. Rinse briefly with extra developer in a spray bottle, then rinse with IPA in a spray bottle. If the wafer is not fully developed, SU-8 will precipitate out in the IPA and you will see white streaks running down the wafer. Return the wafer to the dish with SU-8 developer and repeat until the wafer runs clean during the IPA rinse.
13. Dry wafer with filtered air or N_2 stream.

14. Hard bake for 5-10 minutes by placing wafer on 150°C hot plate. Turn off hot plate and let wafer cool on the hot plate for half an hour (this is to avoid large temperature gradients that can cause SU-8 to detach from the wafer).
15. Silanize master wafer by spincoating 0.5 mL hexamethyldisilazane (HMDS, Sigma-Aldrich) at 1000 rpm for 30s.
16. Wafer is now ready to serve as a master for PDMS devices.

Protocol for making SU-8 master wafer at 50 μm high

1. Turn on UV aligner. Wait 10 minutes before turning on UV light power switch. Measure UV power.
2. Set one hot plate to 65°C, one to 95°C, and one to 150°C.
3. Rinse silicon wafer with acetone, isopropyl alcohol (IPA), and de-ionized water. Dry with nitrogen stream, then place on 150°C hot plate for 15-30 minutes.
4. Program spincoater:
    a. 300rpm for 20s with ramping of 100rpm/s
    b. 500rpm for 20s with ramping of 100rpm/s
    c. 1600rpm for 30s with ramping of 300rpm/s
5. After the wafer dehydration bake (helps SU-8 adhere to the wafer surface), quickly move wafer to spincoater chuck, pour SU-8 2050 photoresist (MicroChem) in the center of the wafer, slowly – to avoid bubbles – until it covers about 1/3 of the wafer surface. Close lid and run spincoater program.
6. Remove SU-8 edge bead with TexWipe soaked in acetone.
7. Initiate soft bake step:
    a. Place wafer on 65°C hot plate for 1.5 minutes.
    b. Place wafer on 95°C hot plate for 7.5 minutes.
8. Calculate exposure time:

$$\frac{160\,\frac{\text{mJ}}{\text{cm}^2}}{\text{measured power}\left(\frac{\text{mW}}{\text{cm}^2}\right)} \times 1.5^2 = \text{exposure time (s)}$$

9. Load wafer on aligner stage. Place mylar mask with channel designs in the designated mask holder. Slowly raise wafer stage until mask is in contact with wafer (you will see the diffraction pattern in sections where contact is made). Set aligner timer and expose wafer to UV light.
10. Initial post-exposure bake step:
    a. Place wafer on 65°C hot plate for 1.5 minutes.
    b. Place wafer on 95°C hot plate for 6.5 minutes.
11. Remove mask from aligner. Let wafer cool briefly before developing away the unexposed SU-8. Turn off 65°C and 95°C hot plates.
12. Develop wafer by filling a Teflon dish with some SU-8 developer and shaking wafer around for a few minutes. Watch wafer to determine when it has finished developing. Rinse briefly with extra developer in a spray bottle, then rinse with IPA in a spray bottle. If the wafer is not fully developed, SU-8 will precipitate out in the IPA and you will see white streaks running down the wafer. Return the wafer to the dish with SU-8 developer and repeat until the wafer runs clean during the IPA rinse.
13. Dry wafer with filtered air or N_2 stream.
14. Hard bake for 5-10 minutes by placing wafer on 150°C hot plate. Turn off hot plate and let wafer cool on the hot plate for half an hour (this is to avoid large temperature gradients that can cause SU-8 to detach from the wafer).
15. Silanize master wafer by spincoating 0.5 mL HMDS at 1000 rpm for 30s.
16. Wafer is now ready to serve as a master for PDMS devices.

Protocol for making SU-8 master wafer at 30 μm high

1. Turn on UV aligner. Wait 10 minutes before turning on UV light power switch. Measure UV power.
2. Set one hot plate to 65°C, one to 95°C, and one to 150°C.
3. Rinse silicon wafer with acetone, isopropyl alcohol (IPA), and de-ionized water. Dry with nitrogen stream, then place on 150°C hot plate for 15-30 minutes.
4. Program spincoater:
   a. 500rpm for 10s with ramping of 100rpm/s
   b. 1000rpm for 30s with ramping of 300rpm/s
   c. 3500rpm for 30s with ramping of 300rpm/s
5. After the wafer dehydration bake (helps SU-8 adhere to the wafer surface), quickly move wafer to spincoater chuck, pour SU-8 2050 photoresist (MicroChem) in the center of the wafer, slowly – to avoid bubbles – until it covers about 1/3 of the wafer surface. Close lid and run spincoater program.
6. Remove SU-8 edge bead with TexWipe soaked in acetone.
7. Initiate soft bake step:
   a. Place wafer on 65°C hot plate for 3 minutes.
   b. Place wafer on 95°C hot plate for 6 minutes.
8. Calculate exposure time:

$$\frac{153.33\,\frac{mJ}{cm^2}}{measured\ power\left(\frac{mW}{cm^2}\right)}\times1.5^2=exposure\ time\ (s)$$

9. Load wafer on aligner stage. Place mylar mask with channel designs in the designated mask holder. Slowly raise wafer stage until mask is in contact with wafer (you will see the diffraction pattern in sections where contact is made). Set aligner timer and expose wafer to UV light.
10. Initial post-exposure bake step:
    a. Place wafer on 65°C hot plate for 1 minutes.
    b. Place wafer on 95°C hot plate for 6 minutes.
11. Remove mask from aligner. Let wafer cool briefly before developing away the unexposed SU-8. Turn off 65°C and 95°C hot plates.
12. Develop wafer by filling a Teflon dish with some SU-8 developer and shaking wafer around for a few minutes. Watch wafer to determine when it has finished developing. Rinse briefly with extra developer in a spray bottle, then rinse with IPA in a spray bottle. If the wafer is not fully developed, SU-8 will precipitate out in the IPA and you will see white streaks running down the wafer. Return the wafer to the dish with SU-8 developer and repeat until the wafer runs clean during the IPA rinse.
13. Dry wafer with filtered air or N_2 stream.
14. Hard bake for 5-10 minutes by placing wafer on 150°C hot plate. Turn off hot plate and let wafer cool on the hot plate for half an hour (this is to avoid large temperature gradients that can cause SU-8 to detach from the wafer).
15. Silanize master wafer by spincoating 0.5 mL HMDS at 1000 rpm for 30s.
16. Wafer is now ready to serve as a master for PDMS devices.

Appendix E. Dry film photoresist protocol

This is done in the BNC clean room – you need safety training from Paul Lum to work here. Talk to graduate students in the Liepmann lab for training with laminator.

1. Turn on laminator machine (Akiles ProLam Ultra Laminator).
2. Set temp to 115°C.
3. Set motor speed on high setting (speed 6).
4. Clean steel wafers:
   a. Score plastic coating with razor and peel off to reveal mirror surface
   b. Remove residual coating with acetone and Texwipe
   c. Rinse with acetone, rinse with IPA, air dry with filtered air or N_2 stream
5. Cut dry film resin to fit wafer; note that there is a dull plastic coating and a shiny plastic coating on the sides of the resin (to protect the photoresist).
6. Peel dull coating off of resin, place edge of resin (resin side down) onto clean wafer top (that will be going through rollers), so shiny coating is facing up. Put on a Texwipe (low lint) then place between sheets of Kapton plastic (minimize resin getting on laminator rollers).
7. Send wafer through laminator so resin, wafer, and Kapton sheets are sandwiched through rollers.
8. Cut extra laminate around edges and back side with a razor or scissors.
9. Add extra layers if required (repeat steps 5-8) BUT you must remove shiny plastic coating before adding a second layer.
10. Turn off laminator.
11. Load mask into UV aligner, measure UV power.
12. Use about 45 seconds (arbitrary time – will depend on development of channels) of exposure.
13. Peel off shiny coat to expose resin, load wafer and raise stage so resin contacts mask.
14. Expose wafer.
15. Develop by placing wafer in a dish with with 1% K_2CO_3 (keep an eye on it).
    a. Development may involve shaking the dish, directed washing with a spray bottle of developer, or using a Q-tip soaked in developer to rub away the unexposed photoresist depending on channel designs.
16. Rinse with DI H_2O (put in dish with water).
17. Air dry with filtered air stream.
18. Wafer is ready for PDMS and bonding. Note: Resin might leave residue on PDMS after first round that makes bonding of PDMS to glass difficult. It is recommended to sacrifice a round of PDMS curing to remove this residue.

Appendix F. Fabrication of microfluidic devices from master wafer

These amounts are for one 4" master wafer.

1. Place a clean 150 ml disposable plastic beaker (Fisher Scientific) on analytical balance and zero/tare the balance.
2. Pour 2.9 g PDMS (Sylgard® 184 kit, Dow Corning) curing agent into beaker.
3. Tare balance. Pour 29 g PDMS base into beaker.
4. Stir PDMS base and curing agent vigorously with glass stir rod for a few minutes. The PDMS should be full of small bubbles such that is appears opaque. Clean stir rod with kimwipe.
5. Place beaker in *room temperature* vacuum oven and set under vacuum for 30 minutes to one hour. (Make sure that the purge valve is closed and the vacuum valve is open, then turn on the vacuum pump. Run until pressure reads around -50 kPa – the actual value is not important but will affect how long the PDMS needs to sit to degas. Turn off pump and close vacuum valve). Open purge valve to release vacuum and open vacuum oven door.
6. Take wafer and place in the center of a piece of aluminum foil, folded into a square ~6" per side. Fold up the foil around the wafer to form vertical "walls" around the edge of the master wafer.
7. Slowly pour degassed PDMS onto the foil-wrapped wafer and place under vacuum (see Step 5) to degas until all bubbles are removed.
8. Set oven to 60°C and let PDMS cure for at least 3 hours. They can be left to cure overnight as well.
9. Remove cured PDMS and wafers from the oven. Remove foil and carefully peel PDMS off of master wafer. Removing the PDMS too fast may lead to tears in the PDMS or detachment of the channel designs from the wafer.
10. Trim individual devices from the PDMS slab with an X-ACTO knife. Ensure that no raised PDMS edges are left around the channels as this will keep the device from bonding to the glass slides.
11. With the channel side facing out, place the PDMS device on a cutting surface and punch out holes for inlets and outlets using a blunt-tip 16-G needle (McMaster Carr). Make sure that the PDMS core is removed from the punched holes.
12. Clean the PDMS device of large debris and dust with a new piece of scotch tape. Rinse PDMS device with IPA, then DI H_2O. Dry with a filtered stream of cold air. Place with the channels facing up near the handheld corona discharger (Electro-Technic Products) and cover with petri dish lid to prevent accumulation of dust.
13. Clean a glass slide by rinsing with acetone, IPA, and DI H_2O. Dry thoroughly with filtered cold air. Set next two the cleaned PDMS device.
14. Turn on handheld corona discharger and hold the apparatus about 1 cm above the PDMS and glass slide (you should see the faint purple plasma). Evenly move the plasma over both surfaces for 10-20 seconds total, then turn the discharger off.
15. Pick up PDMS device and carefully place on glass slide. If necessary, you may need to press certain parts of the PDMS to the glass to remove air bubbles. Visually inspect the device to make sure the PDMS is in contact with the glass.
16. Place the device into a 60°C oven for at least 20 minutes.

# Appendix G. Measuring volume fraction protocol

This was done at the Biological Imaging Facility (BIF) using the M1 Axioimager upright microscope and 40x phase contrast objective. Dr. Denise Schichnes (schichne@berkeley.edu) is a very helpful contact and will train you on setting up Köhler illumination for the best contrast. Muller lab account password: Flu1d1c

1. Pipette 40 µl 100 mM glucose into a 1.5 ml microcentrifuge tube. Gently pipette in 40 µl of the vesicle sample in the tube and stir slowly with the pipette tip.
2. Withdraw 10 µl from the mixture and pipette under the hemocytometer (Hausser Scientific Co.) coverslip to fill the counting chamber. Let vesicles settle for a few minutes, but do not wait longer than 2-3 minutes because your solution will start to evaporate out of the hemocytometer.
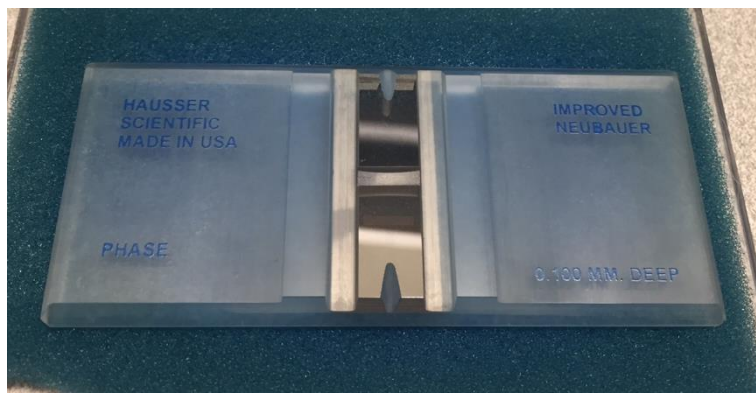
Figure F1 Hemocytometer slide without coverslip.

3. Focus on the plane where the vesicles are settling. The large vesicles will look in focus at a different plane than the small vesicles, but there should be a middle ground where you can capture most of them. Take several snapshots around the slide to capture the full counting grid. Note: this slide is too thick and has beveled edges that make it unable to fit into the stage arms – it is a bit inconvenient to move around.
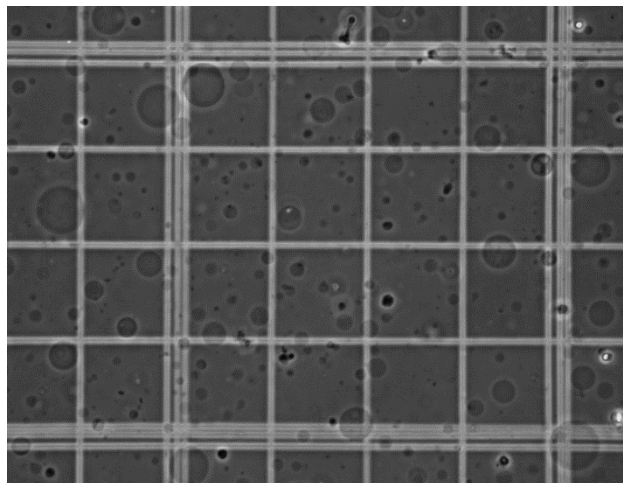
Figure F2 Example snapshot of counting grid with vesicles in focus.

4. Use the ImageJ [Multi-point] tool to count the vesicles in each snapshot.
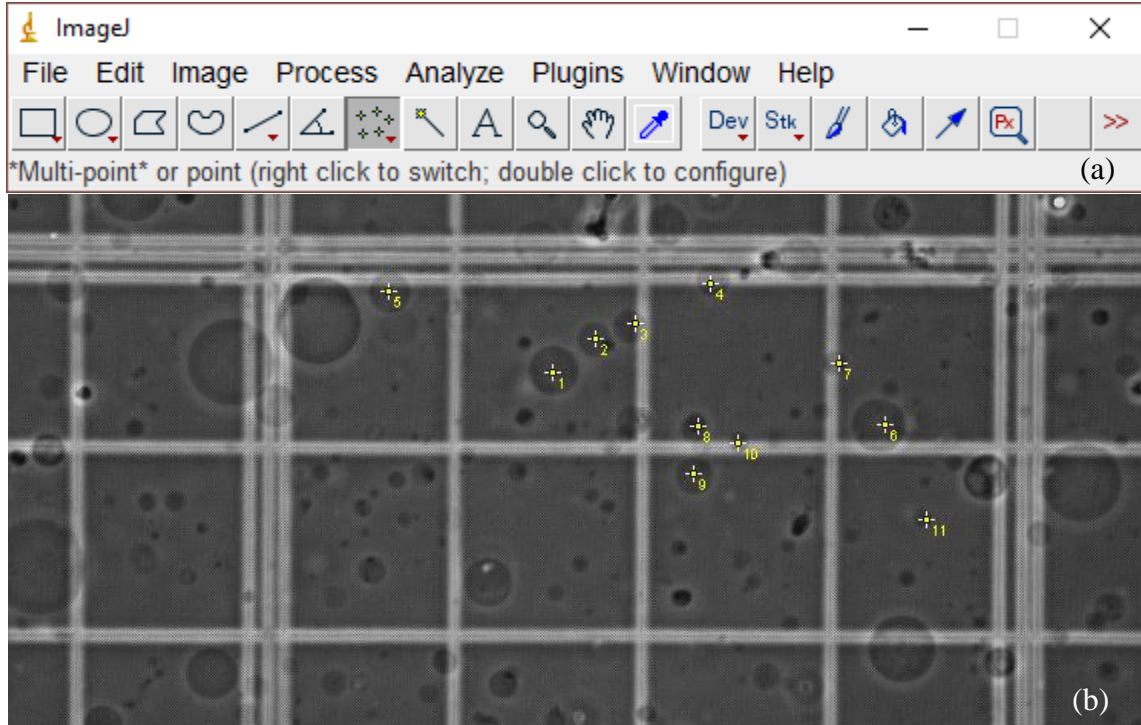
Figure F3 (a) Location in toolbar of [Multi-point] function. (b) Appearance of counted vesicles.

5. One square (surrounded by 3 lines on each side) is equivalent to 4nl. There are 25 total squares that make up the full grid (total volume = 100nl). Sum up the total vesicle count, take the dilution factor into account (multiply by 2 if you diluted the sample with an equal part of sucrose as described in Step 1) and divide by the volume to get the number of vesicles per ml of suspension.

6. To get an estimate of the volume of vesicles per ml of suspension, multiply the count/ml by the average vesicle volume per one vesicle (from the size analysis performed earlier). Another way of estimating the volume fraction is to apply the count/ml to the full size histogram (each histogram bin represents how much that diameter contributed to the size distribution). For example, use the percentage of 5 μm diameter vesicles from the histogram and the count/ml to calculate the volume fraction of 5 μm vesicles. Repeat for each diameter bin and sum to get the total volume fraction.

Appendix H. Preparing separation devices

1. Put in outlet tubing first. Place ends of outlet tubing into a receptacle (like a 1.5 ml centrifuge tube – the tubing can be held in place with tape).
2. Fill a 3 ml syringe with 50% isopropyl alcohol (IPA). Place 0.2 μm filter on end of syringe. Place a 23G blunt tip needle on after the filter. Put inlet tubing on the end of the 23G needle and flush tubing with filtered IPA before placing in PDMS device. Use tweezers and try to quickly insert tubing to avoid pushing debris or dust into the inlet.
3. Fill device with IPA solution by depressing the syringe plunger but do not use too much pressure as this can cause the filter to not work and allow debris into the device. When you see that the outlet containers are being filled with IPA, you can now switch to another solution.
4. If you see debris introduced at this point, you can try to back-flush it out by removing the needle/filter/syringe from the inlet tubing and placing the open end of the tubing in a separate 1.5 ml receptacle. Using one or several outlets, flush the 50% IPA solution through the device; your goal is to have the debris exit through the inlet channel. Pulsing the different IPA syringes can sometimes dislodge the debris. This is more relevant for the filter devices; the inertial device is large enough that most debris can just be flushed through the outlets (no need to back-flush).
5. If you are using spheres, at this point you would start flowing the spheres through, but if you are using vesicles, you must flush the device with different solutions so as to not damage the suspension. If clogging with sphere suspensions are occurring, they may be briefly dislodged by tapping the outlet receptacles or gently lifting them up and dropping them.
6. Remove the 50% IPA from the device by sending filtered DI H_2O through. You can leave the 23G needle in place, just replace the syringes and filters. Make sure that when you are switching syringes, you are not introducing air into the device. The syringe with filter should be initially flushed so that a drop of liquid is visible at the connection point. The needle should be filled so that a convex meniscus is visible. Connect the two droplets so no air is between the filter tip and needle before tightly closing the connection.
7. After the device is flushed with water and no debris is visible (if debris is introduced at or after this point, you will most likely need to start over with 50% IPA as back-flushing with water will introduce air bubbles which are difficult to remove without the IPA solution), you can flush the device with filtered 2 mg/ml bovine serum albumin (BSA). Fill the device and let sit for 5-15 minutes. This step is to prevent lipids from aggregating on the channel walls immediately. Sidenote: Dr. Markita Landry suggested using PEG to prevent lipid aggregation which could be promising, but I have not tried this.
8. Flush the BSA from the device with a 0.2 μm filtered sucrose solution (use what the vesicles were formed in to maintain osmolarity balance across the membrane). In these experiments, this was 100 mM sucrose.
9. Slowly withdraw the vesicles with an 18G needle into a 3 ml syringe. Introduce the vesicles into the device at the desired flow rate. Make sure to switch out the outlet receptacles to collect only vesicles (if residual IPA or BSA solution is left in the outlet collectors, the vesicle suspension will degrade).

Appendix I. Size analysis of rigid sphere suspensions protocol

1. Cut out a CoverWell for each sample. Remove protective backing and place adhesive side down on a #1 glass coverslip.
2. Mix together 40 µl DI H_2O and 20 µl sphere sample. Pipette 40 µl of this mixture into the assembled coverwell and cover openings with clear scotch tape. Let spheres settle for at least 15 minutes so all of the spheres are sitting on the bottom of the well.
3. Using the 20x magnification objective, pick seven locations to image spheres. At each location take two images: one with the filter to pick up the small spheres, one with the filter to pick up the large spheres.

(a)   (b)
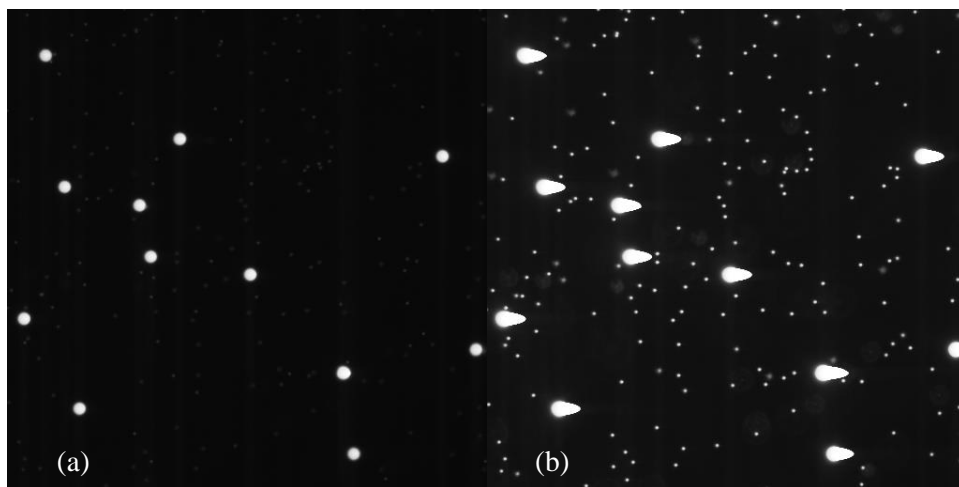
Figure G1 (a) Filter that focuses on large spheres. (b) Filter that captures small spheres as well.

4. In ImageJ, compile the 14 images into a stack: [Image] [Stacks] [Images to Stack]
5. Make the stack into binary images: [Process] [Binary] [Make Binary]
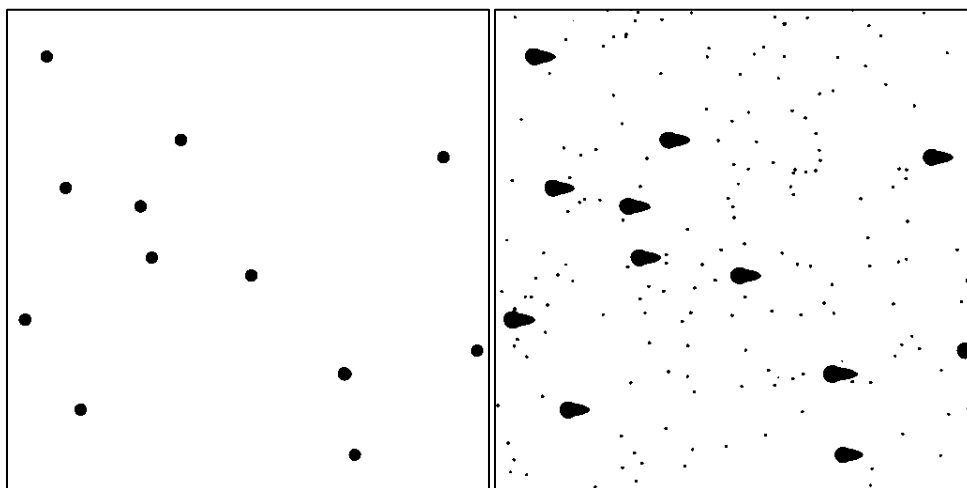
Figure G2 Binary sphere images.

6. Get major and minor ellipse measurements. [Analyze] [Analyze Particles…]
   a. Make sure [Display results] is checked off.
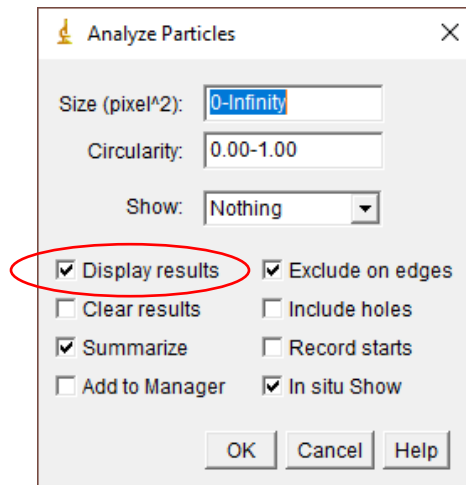
Figure G3 Check [Display results].

b. If you do not see Major/Minor columns in Results table, go to [Analyze] [Set Measurements] and check [Fit ellipse] before repeating step 6.

Figure G4 Check [Fit ellipse] to report Major and Minor lengths for particles.

7. Copy Results (see Figure G5) into an Excel file. Calculate the difference between the Major and Minor columns in a separate column. Highlight the difference column and rank by value: [Home] [Sort & Filter] [Sort Smallest to Largest]
    a. Check [Expand the selection] if the warning pops up about moving the rest of the data.
8. Calculate the average of the Major and Minor lengths for particles that have differences less than 2.3. Convert the measurements from pixels to microns. 100 μm = 126 pixels at 20x with the Photometrics camera.
9. Calculate the histogram with the Data Analysis add-on (see Options). Graph the histogram.

	Area	Major	Minor	Angle	Slice	
1	137	13.423	12.995	150.915	1	
2	142	13.544	13.349	26.379	1	
3	141	13.404	13.394	0.000	1	
4	139	13.457	13.152	45.000	1	
5	141	13.516	13.282	117.268	1	
6	139	13.457	13.152	45.000	1	
7	142	13.544	13.349	26.379	1	
8	144	13.763	13.322	15.642	1	
9	139	13.457	13.152	45.000	1	
10	170	15.004	14.427	152.819	1	

Figure G5 Results table with Major and Minor ellipse axes reported.

Appendix J. Sphere suspension recipes for Chapter 4

For all recipes:
Total sphere volume fraction: 0.01%v/v
7m% NaCl
1%v/v Tween-20
6 ml total volume
Sonicate 10 minutes before using in devices

100% 5 μm spheres
0.4404 g NaCl
4.737 ml DI H$_2$O
1.2 ml 5%v/v Tween-20 solution
63 μl 5 μm stock solution (0.01 g spheres/ml stock) – sonicated 10 minutes

100% 10 μm spheres
0.4404 g NaCl
4.482 ml DI H$_2$O
1.2 ml 5%v/v Tween-20 solution
318 μl 10 μm stock solution (3.6×10^6 beads/ml stock) – sonicated 10 minutes

100% 15 μm spheres
0.4404 g NaCl
4.460 ml DI H$_2$O
1.2 ml 5%v/v Tween-20 solution
340 μl 15 μm stock solution (1×10^6 beads/ml stock) – sonicated 10 minutes

15% 5 μm spheres, 85% 10 μm spheres
0.4404 g NaCl
4.520 ml DI H$_2$O
1.2 ml 5%v/v Tween-20 solution
271 μl 10 μm stock solution (3.6×10^6 beads/ml stock) – sonicated 10 minutes
9 μl 5 μm stock solution (0.01 g spheres/ml stock) – sonicated 10 minutes

25% 5 μm spheres, 75% 10 μm spheres
0.4404 g NaCl
4.546 ml DI H$_2$O
1.2 ml 5%v/v Tween-20 solution
239 μl 10 μm stock solution (3.6×10^6 beads/ml stock) – sonicated 10 minutes
16 μl 5 μm stock solution (0.01 g spheres/ml stock) – sonicated 10 minutes

50% 5 μm spheres, 50% 10 μm spheres
0.4404 g NaCl
4.609 ml DI H$_2$O
1.2 ml 5%v/v Tween-20 solution
159 μl 10 μm stock solution (3.6×10^6 beads/ml stock) – sonicated 10 minutes
32 μl 5 μm stock solution (0.01 g spheres/ml stock) – sonicated 10 minutes

75% 5 µm spheres, 25% 10 µm spheres
0.4404 g NaCl
4.673 ml DI H_2O
1.2 ml 5%v/v Tween-20 solution
80 µl 10 µm stock solution (3.6×10^6 beads/ml stock) – sonicated 10 minutes
47 µl 5 µm stock solution (0.01 g spheres/ml stock) – sonicated 10 minutes

25% 10 µm spheres, 75% 15 µm spheres
0.4404 g NaCl
4.466 ml DI H_2O
1.2 ml 5%v/v Tween-20 solution
80 µl 10 µm stock solution (3.6×10^6 beads/ml stock) – sonicated 10 minutes
255 µl 15 µm stock solution (1×10^6 beads/ml stock) – sonicated 10 minutes

50% 10 µm spheres, 50% 15 µm spheres
0.4404 g NaCl
4.471 ml DI H_2O
1.2 ml 5%v/v Tween-20 solution
159 µl 10 µm stock solution (3.6×10^6 beads/ml stock) – sonicated 10 minutes
170 µl 15 µm stock solution (1×10^6 beads/ml stock) – sonicated 10 minutes

75% 10 µm spheres, 25% 15 µm spheres
0.4404 g NaCl
4.476 ml DI H_2O
1.2 ml 5%v/v Tween-20 solution
239 µl 10 µm stock solution (3.6×10^6 beads/ml stock) – sonicated 10 minutes
85 µl 15 µm stock solution (1×10^6 beads/ml stock) – sonicated 10 minutes

# Appendix K. Microscopy for inertial migration videos

Using the Phantom MIRO M310 camera.

1. Turn on the microscope. Have device prepped and flushed with 50% isopropyl alcohol (IPA) solution. Check the device for debris.
2. Turn on camera. You will hear the fan start up. When the fan sound dies down, open the [PCC 2.6] software icon from desktop.
3. Ensure that the camera is recognized (Figure J1) by the software in the [Manager] tab.
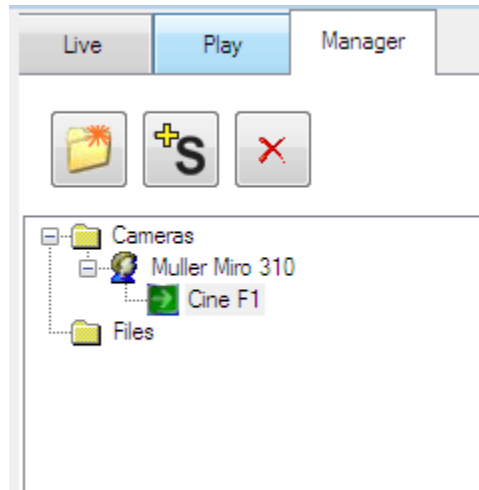
Figure J1 Camera recognition by PCC software

4. Go to [Live] tab and select [Muller Miro 310] from the Camera drop down menu. For inertial migration streak images, you want to choose the Cine Settings so that the [Sample Rate] is set to 24pps, the [Exposure Time] is set to 41000μs.
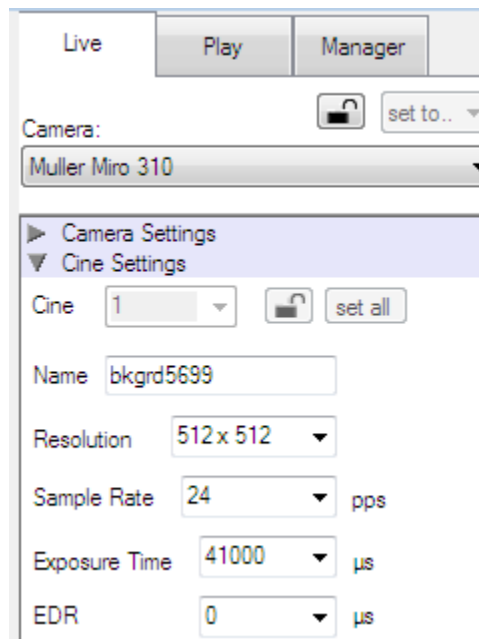
Figure J2 Cine Settings for inertial migration vides

5. Under [Image Range and Trigger Position], set the Last number of frames to be captured to 1200 (Figure J3).
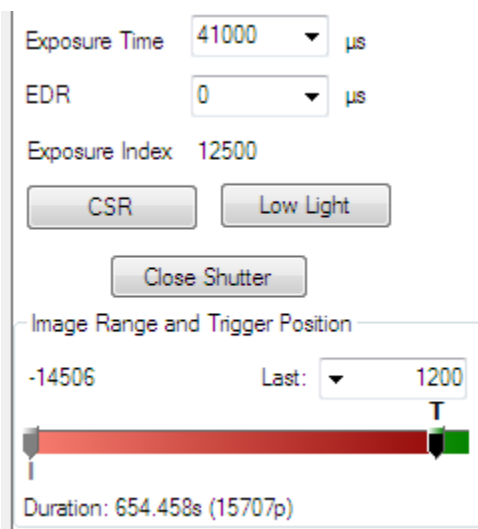
Figure J3 Set last number of frames. Videos recorded will be just under a minute long.

6. Now switch out the IPA syringe for sphere suspension of interest and start up syringe pump to run spheres through device. For a device with channels that are 93 μm high and 50 μm wide, set Q = 5518 μl/hr for Re = 20. Turn on the fluorescent light source and open the shutter on the microscope. Look for spheres to flow through the device. Choose the proper filter for the sphere you are trying to visualize.

| Filter cube	Excitation wavelengths (nm)	Emission wavelengths (nm)
Leica I3	450-490	Long Pass 515
Leica N2.1	515-560	Long Pass 590
Chroma 41001	460-500	510-560
Chroma 51004v2	475-495 and 540-570	500-535 and 580-630

Table J1 Filter cubes available with Leica microscope. Information from Hagar Zohar's notes.

7. Once spheres are visible on camera and through the eyepiece, click the [CSR] button to "Current Session Reference" the camera (see Figure J3). This is important for maximizing contrast in the videos.

8. To record a video, hit [Capture]. You may need to delete previous video that was recorded. Quickly hit [Trigger] to start the actual recording (the time between hitting [Capture] and hitting [Trigger] is recorded as well – since we are interested in only 1200 frames, we want to minimize the extra recording time). Once recording is finished, maneuver to the [Play] tab and select [Save Cine…]. Save file as a Multipage TIF, but be sure to add the ".tif" at the end of the file name so that it is saved properly.

Appendix L. Inertial migration analysis protocol

1. Open video in ImageJ. Run macro (see below for text). The macro first gets an average image from the stack of video frames; it then allows you to rotate the video (you have about five attempts) so streaks are parallel to edges (Figure K1). Brightness and contrast is adjusted, and the user can move the drawn rectangle with arrow keys and take the intensity profile ([Alt] [Ctrl] [K]).
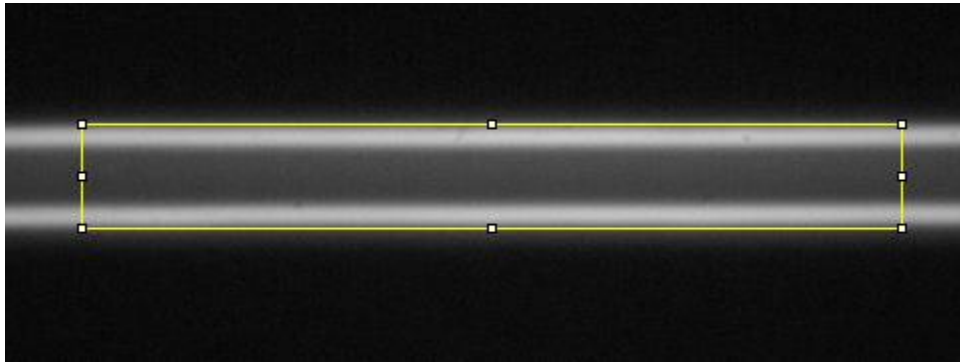
Figure K1 Rotated average image with rectangle in place to measure profile.

2. Select [List] in the profile window and get the (x,y) values for the intensity profile (Figure K2).
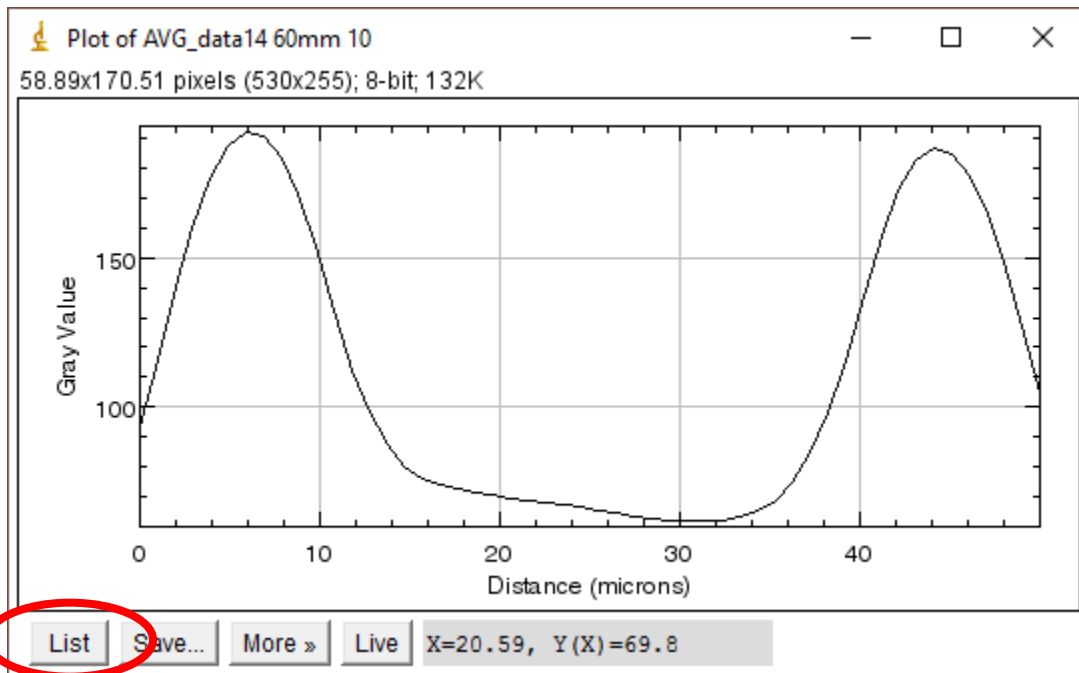
Figure K2 Profile plot. Select [List] to get (x,y) values.

3. Copy the list of plot values to an Excel file. Use the next column to calculate a Gaussian fit to each peak (see example in Table K1). The fit equation is calculated with the three variables a, b, and c and is listed below:

$$\text{Fit} = a \left[e^{-\left(\frac{(x-b)^2}{2c^2} \right)} \right]$$

x	Data	Fit	a	b	c	RSS
0	142.254	147.7702	255.8227	5.841186	5.575305	6.471681
0.9804	172.412	174.9377				
1.9608	201.254	200.794				
2.9412	225.354	223.4544				
3.9216	243.741	241.1002				
4.9019	252.18	252.2178				
…	…	…				

Table K1 Example of plotted data and fit calculations.

4. The quality of the fit is determined by calculating the "root sum square" (RSS); this looks at the difference between the data and the fit values. Careful selection of the range of Data and Fit values is necessary to ensure a good fit. To improve the fit, you can minimize the RSS using built-in Excel functions.

$$\text{RSS} = \sqrt{\sum_i (\text{Data} - \text{Fit})^2}$$

5. To get the [Solver] function, go to [File] [Options] [Add-Ins]. Under the [Manage] menu, select [Excel Add-ins] and hit [Go…]. Select [Solver Add-in] and hit [OK].
6. Now minimize the RSS error (which will optimize the Gaussian fit). Under the [Data] tab, go to the [Analysis] section and select [Solver]. Under [Set Objective:] choose the cell with the RSS equation. Make sure that [Min] is selected. under the [By Changing Variable Cells:] choose the cells that contain the variables a, b, and c. Then select [Solve].
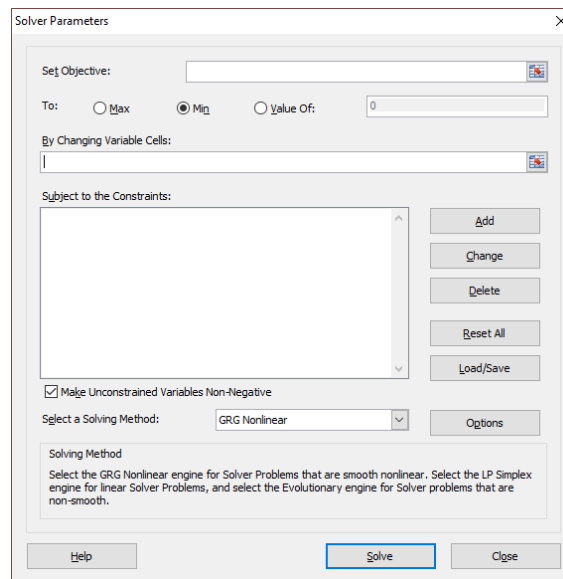
Figure K3 Solver window to minimize the error between the Data and Fit columns in Excel.

7. Repeat this error minimization between Data and Fit with the second peak in the intensity profile (two separate Gaussians are being calculated here).
8. Calculate the full width at half maximum (FWHM) for each fitted Gaussian curve (Figure K4) using the variable c used to calculate the Fit column:

$$\text{FWHM} = 2c\sqrt{2\ln(2)}$$

Example profile with Gaussian fits
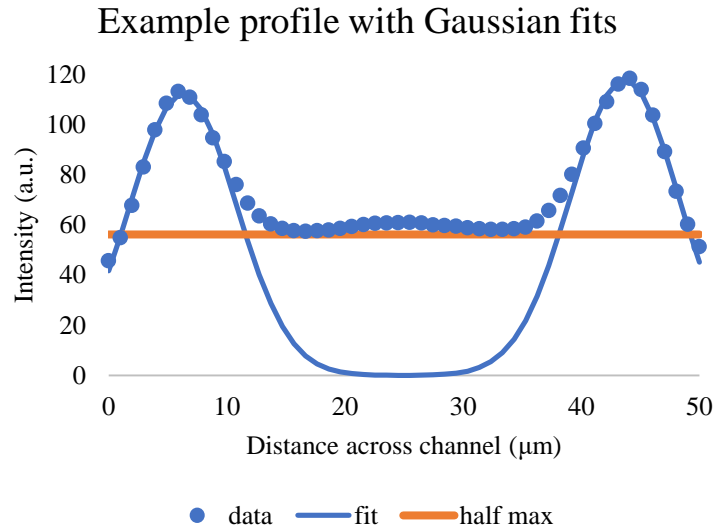
Figure K4 Example of what fitted data look like with a visualization of where the FWHM is measured.

9. After each video is analyzed and a FWHM is calculated for both profile peaks, plot the FWHM values against the length at which each FWHM was measured. Fit a three parameter exponential function to the FWHM values using the RSS, similar to the process above (see Figure K5). Here, K is a scaling factor, x is the length in mm down the channel, L is the decay parameter, and A is the horizontal asymptote.

$$\text{Fit} = Ke^{-\left(\frac{x}{L}\right)} + A$$

10. When the RSS calculated between the data and the fit is minimized, the entry length can be determined by solving for the length (x') at which the Fit function falls within 5% of the horizontal asymptote:

$$1.05A = Ke^{-\left(\frac{x'}{L}\right)} + A, \text{ solve for } x'$$

$$x' = -L \times \ln\left(\frac{0.05A}{K}\right)$$
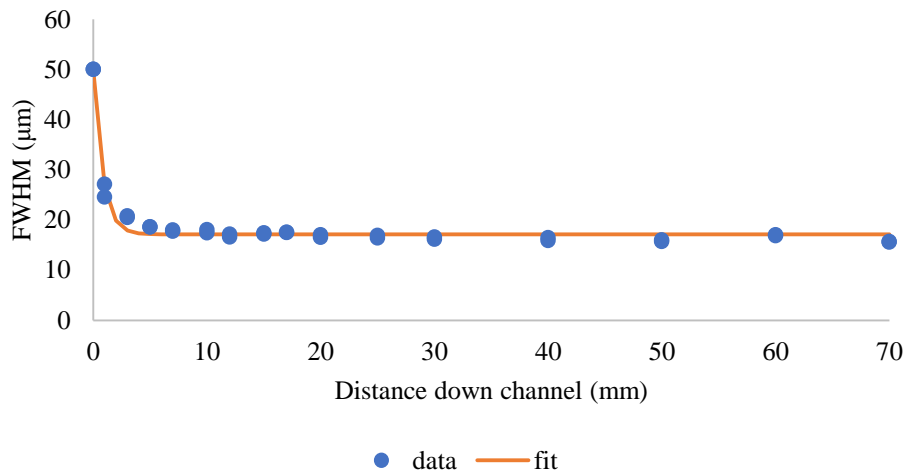
94

Example plot of FWHM vs. L

Figure K5 Plot of FWHM vs. L with fitted exponential.

ImageJ macro for getting intensity profile from inertial migration videos taken at 20x magnification with channels that are 50 μm wide. Save text as a .txt file and install in ImageJ: [Plugins] [Macros] [Install…]. After this, it should show up in the [Macros] menu. Open a video and click the macro to run.

```
// For analysis of sphere migration videos

// Get average of pixels in video
run("Z Project...", "projection=[Average Intensity]");

// Set distance units to microns from pixels
run("Properties...", "channels=1 slices=1 frames=1 unit=microns pixel_width=0.98039
pixel_height=0.98039 voxel_depth=0.98039");

// Find best rotation angle through iteration
for (i = 0; i < 5; i++) {

        // Set rotation angle
        Angle = getNumber("Enter rotation angle",0);
        print( "Angle = " +Angle);

        // Rotate image
        run("Rotate...", "angle="+Angle+" grid=1 interpolation=Bilinear");

        // Check rotation
        rotationOK = getBoolean("Is the rotation okay?");
        if(rotationOK == false) {
```

```
                run("Undo");
        }
        else {
                i = 4;
        }
}

// Brighten image for easier visual gaussian fitting
run("Brightness/Contrast...");
setMinAndMax(0, 65);
run("Apply LUT");

// Set rectangle for profile measurement
run("Specify...", "width=400.98 height=50.00 x=42.49 y=220.49 scaled");
```

Appendix M. Pixel to micron conversions for image analysis

Using the Leica DMIRE2 inverted microscope.

Photometrics Cascade 512b CCD camera:

Magnification	Pixel count	Microns
10x	75	100
20x	126	100
63x	392	100
100x	381	60

Table L1 Pixel to micron relationship for Photometrics camera.

Phantom MIRO M310 camera:

| Magnification	Pixel count	Microns
10x	60	100
20x	102	100

Table L2 Pixel to micron relationships for Miro camera.

It is recommended to check these values with the calibration slide as there are different light column tube connectors for the camera with different magnifications.

Appendix N. Profilometer to measure channel height protocol

The profilometer (LaserScan, Solarius™ Development) is located in 340 Hearst Memorial Mining Building (Liepmann Lab) – speak to graduate students in Liepmann lab for training.

1. Turn on three power buttons in cabinet underneath profilometer
   a. Stage motor
   b. Laser profilometer
   c. Computer
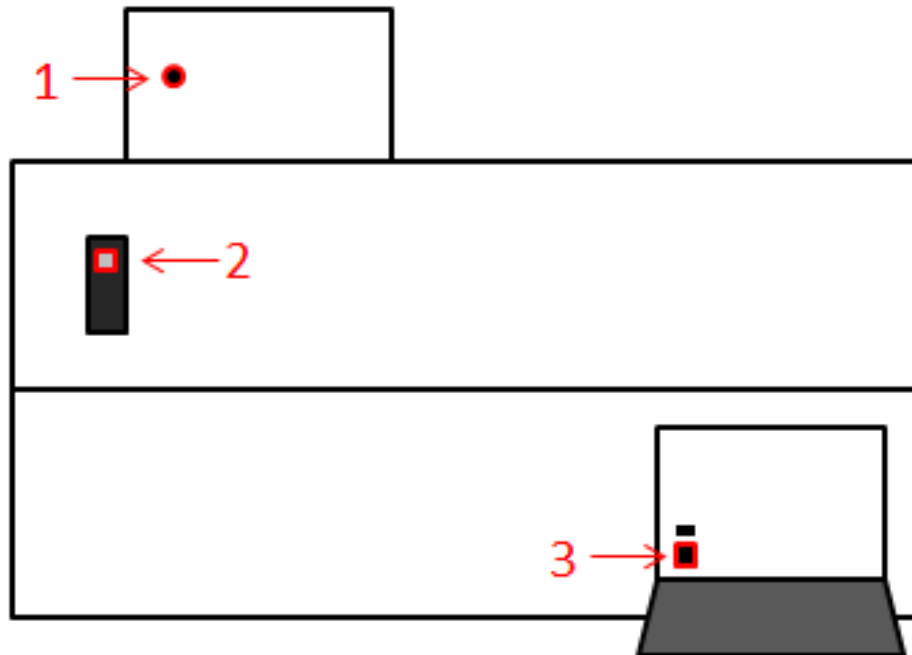
Figure H1 Three power buttons that need to be turned on for profilometer to work.

2. Computer log in:
   a. Username: lab2
   b. PW: arkal123
   c. Domain: ARKALMED
3. Open LaserScan program and log in:
   a. Username: Engineer
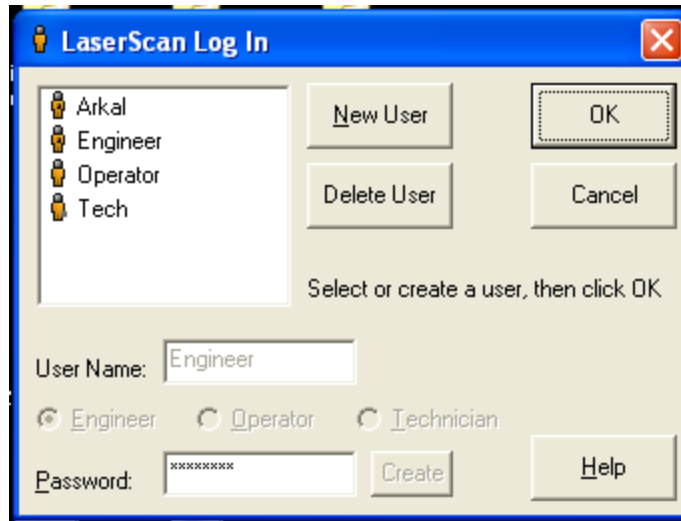   b. PW: Engineer

Figure H2 Login page.

4. Focus laser on either SU-8 wafer or PDMS (from dry film wafer – the resin is difficult for the laser to accurately measure)
   a. You are looking for a very small bright dot reflected off the surface to indicate the laser is focusing on the surface. This is difficult to see (especially with the PDMS) and may take a couple of tries. Often it helps to focus on the edges of the channel, because they reflect more light towards you or even to focus on dust sitting on the surface.
5. Set up an area scan or line scan. Area scans will give you more information to average over, but line scans are much faster.
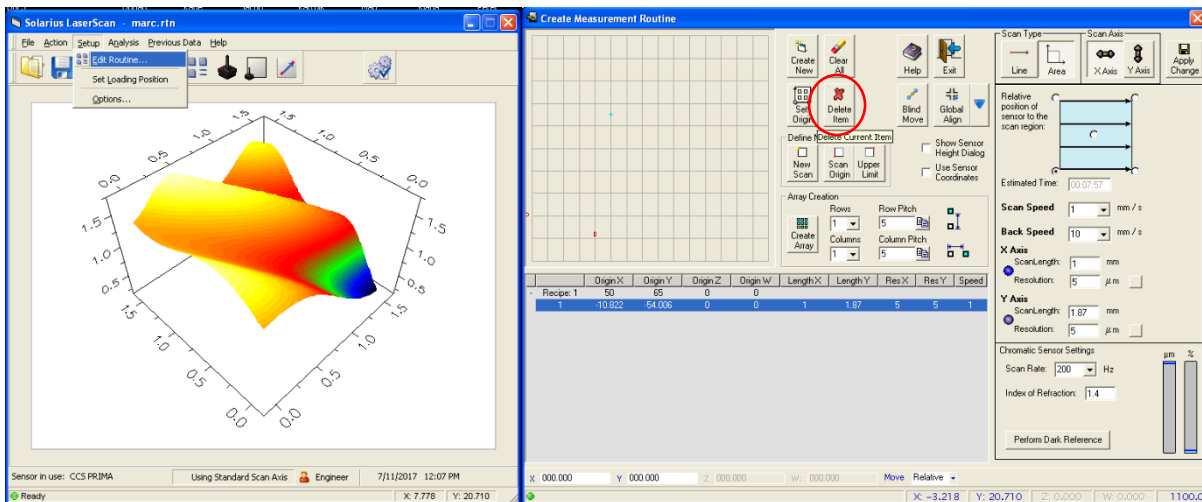   a. [Set up] [Edit Routine] [Delete Item] Select Area or Line Scan

Figure H3 LaserScan interface and [Edit Routine…] interface. Delete the previous scan item.

   b. Move laser in the X-Y direction by clicking [Toggle Joystick ON/OFF] and using the joystick to the side of the profilometer. Make sure the laser is focused on the device surface by moving the laser head up and down with the knob attached to

99

the laser head. Good focusing is achieved when the [Chromatic Sensor Settings] bars are in the center of the range (see Figure H4).
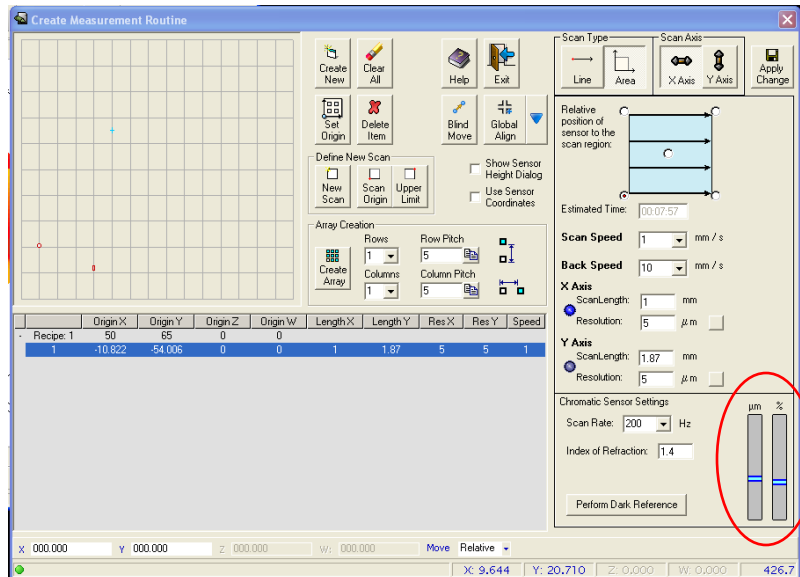
Figure H4 Where the sensor settings should lie for profilometer to be in focus.

    c. [New Scan] [Set Origin] This is where the scan will start. Denote where the scan will end with [Upper Limit].

    d. Check index of refraction (PDMS is 1.4). Adjust resolution or scan direction if needed.

    e. Hit [Apply Change] and [Exit].

6. Hit [Play] to run the scan.

7. To analyze data, open SolarMap Universal 5.0 Program

    a. [Operators] [Leveling…]

    b. [Operators] [Profile Extraction…]

    c. [Studies] [Step Height Measurement]

8. Repeat measurements in other locations across the wafer.

9. Shut down the computer and turn off the stage and laser profilometer motors.